SNAKE INSTABILITY, VORTEX LATTICES AND FRACTIONAL QUANTUM HALL STATES IN TWO-DIMENSIONAL ANISOTROPIC BOSONIC QUANTUM GASES

A THESIS SUBMITTED TO
THE GRADUATE SCHOOL OF NATURAL AND APPLIED SCIENCES
OF
MIDDLE EAST TECHNICAL UNIVERSITY

BY

UMUT TANYERİ

IN PARTIAL FULFILLMENT OF THE REQUIREMENTS
FOR
THE DEGREE OF MASTER OF SCIENCE
IN
PHYSICS

JULY 2025

Approval of the thesis:

SNAKE INSTABILITY, VORTEX LATTICES AND FRACTIONAL QUANTUM HALL STATES IN TWO-DIMENSIONAL ANISOTROPIC BOSONIC QUANTUM GASES

submitted by **UMUT TANYERİ** in partial fulfillment of the requirements for the degree of **Master of Science in Physics Department, Middle East Technical University** by,

Prof. Dr. Naci Emre ALTUN
Dean, Graduate School of **Natural and Applied Sciences** _____

Prof. Dr. Seçkin Kürkçüoğlu
Head of Department, **Physics** _____

Assist. Prof. Dr. Ahmet Keleş
Supervisor, **Physics, METU** _____

Assoc. Prof. Dr. Mehmet Atakan Gürkan
Co-supervisor, **Physics, METU** _____

Examining Committee Members:

Prof. Dr. Mehmet Özgür Oktel
Physics, Bilkent University _____

Assist. Prof. Dr. Ahmet Keleş
Physics, METU _____

Prof. Dr. Bilal Tanatar
Physics, Bilkent University _____

Prof. Dr. Rıfat Onur Umucalılar
Physics, Mimar Sinan Fine Arts University _____

Assoc. Prof. Dr. Mehmet Atakan Gürkan
Physics, METU _____

Date:24.07.2025

I hereby declare that all information in this document has been obtained and presented in accordance with academic rules and ethical conduct. I also declare that, as required by these rules and conduct, I have fully cited and referenced all material and results that are not original to this work.

Name, Surname: Umut Tanyeri

Signature :

ABSTRACT

SNAKE INSTABILITY, VORTEX LATTICES AND FRACTIONAL QUANTUM HALL STATES IN TWO-DIMENSIONAL ANISOTROPIC BOSONIC QUANTUM GASES

Tanyeri, Umut
M.S., Department of Physics
Supervisor: Assist. Prof. Dr. Ahmet Keleş
Co-Supervisor: Assoc. Prof. Dr. Mehmet Atakan Gürkan

July 2025, 89 pages

This thesis consists of two main works. First, we investigate the snake instability of solitons in 2D Bose-Einstein condensates. By proposing a variational wavefunction and using the Gross–Pitaevskii equation, we analytically and numerically explore stability criteria for dark solitons, which depend on the system's physical constants. In the second part, we consider a rapidly rotating anisotropic Bose gas. Projecting the full Hamiltonian onto the lowest Landau level, we derive a two-parameter model to study the effects of interaction strength, rotation, and anisotropy on the ground state of the system. Through exact diagonalization and density matrix renormalization group techniques, we obtain a phase diagram featuring broken-symmetry phases and topologically ordered quantum Hall states, paving the way for future exploration of anisotropic quantum fluids.

Keywords: Ultracold Atomic Gases, Gross-Pitaevskii Theory, Snake Instability, Density Matrix Renormalization Group, Fractional Quantum Hall Effect

ÖZ

İKİ BOYUTLU YÖNBAĞIMLI BOSE KUANTUM GAZLARDA YILAN KARARSIZLIĞI, VORTEX ÖRGÜLERİ VE KESİRLİ KUANTUM HALL DURUMLARI

Tanyeri, Umut
Yüksek Lisans, Fizik Bölümü
Tez Yöneticisi: Dr. Öğr. Üyesi. Ahmet Keleş
Ortak Tez Yöneticisi: Doç. Dr. Mehmet Atakan Gürkan

Temmuz 2025 , 89 sayfa

Bu tez iki ana çalışmadan oluşmaktadır. İlk olarak, 2 boyutlu Bose-Einstein yoğunlaşmalarındaki solitonların yılan kararsızlığını araştırdık. Varyasyonel bir dalga fonksiyonu önererek ve Gross-Pitaevskii denklemini kullanarak, sistemin fiziksel sabitlerine bağlı olan karanlık solitonlar için kararlılık kriterlerini analitik ve sayısal olarak araştırdık. İkinci bölümde, hızla dönen yönbağımlı bir Bose gazı inceledik. Hamiltonyen'in tamamını en alt Landau seviyesine yansıtarak, etkileşim kuvveti, dönme ve yönbağımlılığı incelemek için iki parametreli bir model türettik. Kesin diyagonalizasyon ve yoğunluk matrisi renormalizasyon grubu teknikleri aracılığıyla, kırık simetri fazları ve topolojik kuantum Hall durumlarını içeren bir faz diyagramı elde ettik ve bu da anizotropik kuantum akışkanlarının gelecekteki araştırmalarının önünü açtı.

Anahtar Kelimeler: Aşırı Soğuk Atom Gazları, Gross-Pitaevskii Kuramı, Yılan Kararsızlığı, Yoğunluk Matrisi Renormalizasyon Grubu, Kesirli Kuantum Hall Etkisi

To my family...

ACKNOWLEDGMENTS

I would like to express my sincere appreciation to my supervisors, Prof. Mehmet Özgür Oktel, Assist. Prof. Ahmet Keleş, and Assoc. Prof. Mehmet Atakan Gürkan, for their endless support throughout my postgraduate education. They taught me that there is always something new to learn and played a significant role in my development as a researcher. I cannot emphasize enough their contribution to the writing of the articles associated with this thesis. I am also grateful to Prof. Onur Umucalılar, who shared his wisdom and provided invaluable support to this work.

I want to thank my collaborators and colleagues, Taha Alper Yoğurt and Ahmed Kallushi, for their essential contributions to this work and for their friendship. Additionally, I want to thank my friends, Özgür Nazlı, Gün Günal, and Umut Can Turhan, for being by my side during some of the most stressful and challenging moments, and for helping to make those days as cheerful as possible.

I acknowledge the financial support provided by the 2210-E National M.Sc. Scholarship Program for Former Undergraduates run by TÜBİTAK Science Fellowships and Grant Programmes Directorate (BİDEB) for this thesis.

I want to thank my beloved family, who have always believed in me from the very beginning. I have always felt their love and faith in me, even when we were not in the same place. Finally, I thank my dear companion Ahsen. Since my undergraduate years, she has always been by my side and has never withheld her support. She has consistently helped me overcome my shortcomings—of which there have been many. To me, she has been more than a spouse; she has been my best friend. I am grateful for all the support she has given me so far and the joyful moments she has brought into my life.

TABLE OF CONTENTS

ABSTRACT v

ÖZ vi

ACKNOWLEDGMENTS viii

TABLE OF CONTENTS ix

LIST OF FIGURES xii

LIST OF ABBREVIATIONS xvi

CHAPTERS

1 INTRODUCTION 1

2 THEORETICAL BACKGROUND 3

2.1 Weakly Interacting Bosonic Quantum Gases 3

2.1.1 The Gross-Pitaevskii Theory 4

2.1.2 BEC in Traps and Dimensional Reduction 5

2.1.3 Dimensionless Form of the GP Equations 7

2.1.4 Thomas-Fermi approximation 8

2.1.5 Solitons 11

2.1.6 Bose Gas in Rotating Traps 13

2.2 Quantum Hall States 15

2.2.1 Integer Quantum Hall Effect and Landau Levels 15

2.2.1.1 Landau Gauge 16

2.2.2 Fractional Quantum Hall Effect and Laughlin State 18

3 NUMERICAL METHODS 19

3.1 Numerical Methods for Partial Differential Equations 19

3.1.1 Discretization of 2D wavefunction 19

3.1.2 Central Finite Difference Method and Discretization of the 2D GPE 20

3.1.3 Forward Euler Method 21

3.1.4 Crank-Nicolson Method 22

3.1.5 Split-Step Fourier Method 23

3.2 Exact Diagonalization 25

3.3 Density Matrix Renormalization Group 26

3.3.1 Reduced Density Matrix and Truncation in DMRG Algorithms 27

3.3.2 DMRG with Matrix Product States 29

4 SNAKE INSTABILITY IN BOSE-EINSTEIN CONDENSATE IN ANISOTROPIC TRAPS 31

4.1 Excitation Energies of Solitons and Vortices in Anisotropic Trap . . 32

4.2 Numerical Observation of Snake Instability 35

4.3 Variational Wavefunction 37

4.4 Stability Analysis of Dark Soliton 38

4.4.1 Condensate with Constant Density 39

4.4.2 Condensate with Thomas-Fermi Density 45

4.4.3 Condensate with Gaussian Density Profile 51

4.5 Comparison with Numerical Simulations 56

4.6 Conclusion 57

5 VORTICES AND FRACTIONAL QUANTUM HALL STATES IN A RAPIDLY ROTATING ANISOTROPIC BOSE GAS 61

5.1 Model 62

5.2 Phase Space of the System 66

5.2.1 Fractional Quantum Hall Phase 69

5.2.2 Vortex Lattice and Meissner Phases 71

5.2.3 Crossover at Quasi-1D Regime 72

5.3 Conclusion 74

6 CONCLUSION 77

REFERENCES 79

LIST OF FIGURES

FIGURES

Figure 2.1 The maximum density $n_{\max}$ as a function of the anisotropy ratio ω for $gN = 400$. Numerically obtained GP simulations (dots) follow the 2D TF (dashed) approximation for smaller anisotropies and the 1D TF (dash-dotted) in the large anisotropy limit. The insets display cross-sections of the density profile along the y-axis for selected values of ω, demonstrating the crossover from the 2D TF to the 1D TF regime in large anisotropies. The numerical method used to obtain the ground states in GP simulations with Wick rotation of time $t \to -\mathrm{i}\tau$ is discussed in Sec.3.1.5 10

Figure 3.1 In the MPS method, the coefficients $\psi_{n_1 n_2 \cdots n_N}$ of Fock states, which are in the form of an Nth order tensor (a), are obtained by multiplying N-many matrices (b). 29

Figure 4.1 Comparison of mean excitation energies of soliton (blue) and vortex (orange) states for $N = 500$ and $g = 1$. Dashed lines refer to the variational states defined in Eqs. (4.1), whereas the solid lines show the energies of numerically obtained excitations. 33

Figure 4.2 Comparison of densities of a single-vortex (a), a solitonic vortex (b), and a soliton (c) excitations obtained for $\omega = 30$, $Ng = 500$. The single vortex is obtained with a variation function φ_{v}, where the solitonic vortex and the dark soliton are obtained with imaginary time evolution with corresponding symmetry constraints mentioned in the text. 34

Figure 4.3 Time evolution of a dark soliton in a trapped BEC for two different trap anisotropies, both with $g = 1$ and $N = 400$. The colorbars show the density of BECs. Top row: For $\omega = 3$, the soliton is dynamically unstable and decays via the snake instability, leading to the formation of vortex structures. Bottom row: For $\omega = 35$, the soliton remains stable and persists without significant deformation. Note that the vertical axis (y) is scaled differently in the two panels to reflect the change in trap geometry. 36

Figure 4.4 Density profile of the variational wavefunction defined in Eq. 4.3 in a condensate with constant density n. We choose the parameter $\alpha = 0.0$ (a & d), 0.5 (b & e), and 1.0 (c & f). We choose $\beta = 0$ in the top figures (a, b & c) and $\beta = 0.4$ for the remaining (d, e & f). 38

Figure 4.5 Phase space of the variational dynamical system defined by Eqs.(4.25) in the complex $A = \alpha + \mathrm{i}\beta$ plane, illustrating the dependence of the flow topology on the perturbation wavenumber k. The colorbars indicate the potential energy $U(\alpha, \beta)$ calculated with Eq.(4.4b), and the arrows show the direction of the flow in the phase space. For large $k = 2.0\sqrt{\mu}$,(top), the origin is a stable center, and all nearby trajectories form closed orbits, indicating dynamically stable soliton configurations. For small $k = 0.5\sqrt{\mu}$(bottom), the origin becomes a saddle point and two stable fixed points appear along the $\beta = 0$ axis, signaling a stable vortex-antivortex array. 43

Figure 4.6 The real-time dynamical evolution of an unstable dark soliton for $gN = 200$ inside a trapping potential with a near-critical anisotropy ratio $\omega = 8$. The colorbar shows the density. Approaching the critical anisotropy, the unstable dark soliton decays through an odd-in-y perturbation with a single vortex at the center. 50

Figure 4.7 The time evolution of the overlap function $F(t)$ defined in Eq.(4.62) for two different trap anisotropies and $gN = 200$. Below the critical anisotropy (circle), the dark soliton decays into vortices and $F(t)$ rapidly drops below 1% of its initial value, whereas beyond the critical value (square), the overlap F stays almost the same. 57

Figure 4.8 Critical anisotropy ratio ω_c as a function of the parameter gN. Orange dots indicate the values obtained from numerical GP simulations. The numerical uncertainties are smaller than the marker size for all simulation points. Three theoretical predictions are shown for comparison: the constant-density approximation (dotted), the 2DTF model (dashed), and the 1DTF model (dash-dotted). The constant-density model slightly underestimates the critical anisotropy, and the 1DTF model appears to overestimate it, whereas the 2DTF model provides an excellent fit to the numerical data. 58

Figure 5.1 Geometry of the 2D rotating atomic Bose gas in the Landau gauge and schematic representation of the eigenfunctions of the noninteracting Hamiltonian. 63

Figure 5.2 (a) The phase diagram of a rapidly rotating anisotropic Bose gas described by the Hamiltonian (5.8) for $N = 5$ as a function of the interaction strength g and anisotropy γ. The color bar indicates the von Neumann entanglement entropy calculated with DMRG. The red dots are obtained from ED by finding the change of the ground state momentum (see the main text). (b) The von Neumann entropy (solid line) and particle-hole excitation gap (5.16) (dashed line) along the horizontal cuts in the phase diagram. (c) The overlap between the ground state calculated with ED and the $\nu = 1/2$ Laughlin state along the same cuts. 67

Figure 5.3 (Top) Energy spectrum of the Hamiltonian (5.8) for $N = 5$ bosons with $g = 10$ and $\gamma^{-1} = 4$, 10 and 30, which is cut through the FQH phase in Fig. 5.2 vertically. We choose the number of sites to be 11 to have a symmetric spectrum (density) with respect to the origin $K = 0$ ($i = 0$). Ground state is labeled with (orange) marks for better visibility. (Bottom) Occupations $\langle n_i \rangle$ in the ground state for the trap minima located in the middle site which shows transition from the Tao-Thouless state to the Laughlin state and then to the quasi-1D state, as the anisotropy ratio γ tuned from thin-cylinder to two-dimensional and then to wide-cylinder limit regimes. 70

Figure 5.4 (Top) energy spectrum of a vortex lattice obtained with $(\gamma N)^{-1} = 2.2$ and $g/N = 0.6$ and a Meissner phase with $(\gamma N)^{-1} = 2.2$ and $g/N = 0.1$. (Bottom) Density profiles of the ground state related to the given energy spectrum above. The given density for the vortex lattice is obtained with a linear combination of the degenerate ground states with $K = \pm 2$. 72

Figure 5.5 Entanglement entropy S_{vN} as a function of the interaction strength g for $N = 5$, 8, and 10 bosons for (a) $(\gamma N)^{-1} = 1.50$ and (b) $(\gamma N)^{-1} = 2.00$. The entropy during the phase transition between the Meissner and vortex lattice phases forms a tip in the entanglement spectrum, and rapidly increases with the number of atoms N, which can be used as a signature of a diverging behaviour in the second-order phase transition. . 73

Figure 5.6 Entanglement entropy per particle S_{vN}/N as a function of the interaction strength g for $N = 5$, 8, and 10 bosons in the half filling case $\nu = 1/2$ and in the pure edge limit $(\gamma N)^{-1} = 2.75$. The scaling with g/N gives a critical point $g_c/N \approx 0.5$. 73

LIST OF ABBREVIATIONS

ABBREVIATIONS

1D	1 Dimensional
2D	2 Dimensional
3D	3 Dimensional
FQH	Fractional quantum Hall
IQH	Integer quantum Hall
BEC	Bose-Einstein condensate
GP	Gross-Pitaevskii
TF	Thomas-Fermi
LLL	Lowest Landau level
ED	Exact diagonaliation
DMRG	Density Matrix Renormalization Group

CHAPTER 1

INTRODUCTION

Bose–Einstein condensates (BECs) provide a highly controllable platform for exploring diverse quantum many-body phenomena, ranging from nonlinear solitary excitations to strongly correlated topological phases. Enabled by the precise manipulation of trapping geometries, interaction strengths, and dimensionality in ultracold atomic systems, BECs allow unprecedented access to control their dynamical aspects and quantum phases [1, 2, 3, 4]. This thesis investigates two such aspects in Bose gases under anisotropic confinement: the dynamical instability of dark solitons and the emergence of fractional quantum Hall (FQH) phases in the rapid rotation limit.

The first part of this thesis investigates dark solitons—localized nonlinear excitations with a density dip and a phase jump—that appear as exact solutions to the one-dimensional (1D) Gross–Pitaevskii (GP) equation in repulsive Bose gases [5, 1]. Although stable in quasi-1D systems, solitons become unstable in higher dimensions due to transverse modulations, resulting in the so-called snake instability [6, 7]. This leads to their decay into vortex lines or rings, depending on trap anisotropy [8, 9]. While previous studies based on Bogoliubov-de Gennes theory successfully identified unstable modes [10, 11], they are limited to linear regimes and homogeneous settings [12]. To overcome this, we develop a variational framework that captures soliton bending and vortex-antivortex formation. Using Lagrangian dynamics, we identify critical anisotropy values of the trap for the stability of the soliton [13]. Our analytical predictions are in good agreement with full numerical simulations of the GP equation

The second part focuses on strongly correlated phases in rapidly rotating Bose gases, where the condensate is confined to the lowest Landau level (LLL), and FQH–like

states emerge [2, 3] in the strong interaction regime. In rotating frames, the Coriolis force mimics the Lorentz force, allowing ultracold atoms to experience effective magnetic fields [2]. As the rotation rate approaches the trap frequency, a dense vortex lattice forms [14, 15], which eventually melts into a strongly correlated liquid described by Laughlin-type states around filling factor $\nu \sim 6$ [16, 17]. However, the role of anisotropy and edges in this transition remains underexplored [18, 19, 20]. We construct a microscopic model for a rapidly rotating Bose gas in an anisotropic two-dimensional (2D) trap, project it onto the LLL in the Landau gauge, and derive a 1D lattice model with long-range interactions. Using exact diagonalization (ED) and density matrix renormalization group (DMRG) methods, we identify a phase diagram featuring condensates, vortex lattices, and FQH phases.

This thesis is organized as follows. Chapter 2 provides the necessary theoretical background for both studies, including derivations of relevant models and effective descriptions in the presence of rotation and anisotropy. Chapter 3 introduces the numerical methods used in both studies. Chapter 4 presents the variational analysis of the snake instability in anisotropic BECs. Chapter 5 introduces a rich phase diagram of a rapidly rotating anisotropic Bose gas and discusses the emergence of FQH phases. Finally, Chapter 6 summarizes the key results and concludes the thesis.

CHAPTER 2

THEORETICAL BACKGROUND

2.1 Weakly Interacting Bosonic Quantum Gases

The realization of BECs in cold, dilute alkali-metal gases [21, 22, 23] has led to the emergence of an exciting new field that continues to grow. Typically, these systems are characterized by a macroscopic condensate wave function, $\psi(r, t)$, which describes both the static and dynamic behavior of the BEC [1, 24]. With the introduction of GP theory, which is detailed in the following section, the dynamical and theoretical analysis of these states becomes more accessible both analytically and numerically.

Later experiments produced rotating condensates, starting with a small number of vortices [25, 26] and progressing to larger vortex arrays [14, 27]. Similar to what was observed in rotating superfluid Helium-4 [28], the vortices exhibit quantized circulation, which arises from the single-valued nature of the condensate wave function, ψ. Rapidly rotating Bose gases are particularly significant due to their ability to realize strongly correlated quantum phases in a highly controllable and clean experimental environment. By adjusting the inter-particle interactions—either by varying their strength through Feshbach resonances or modifying their character using dipolar forces—experimentalists can investigate scenarios where the physics diverges dramatically from that of weakly interacting condensates [2].

At sufficiently high rotation rates, the system enters a regime in which the number of vortices becomes comparable to the number of particles. In this regime, conventional mean-field descriptions fail, and the condensate transitions to a landscape of strongly correlated states [16, 29]. Interestingly, these phases are the bosonic counterparts of

the FQH states [2] that were originally found in 2D electron gases subjected to strong magnetic fields [30].

Consequently, rotating Bose gases provide a powerful platform for exploring quantum Hall-like phenomena in a new context—one where interaction and geometry can be precisely controlled. This makes them not only a subject of intrinsic theoretical interest but also a promising avenue for discovering new states of matter that lack direct analogs in traditional condensed matter systems.

2.1.1 The Gross-Pitaevskii Theory

The GP theory, named after Eugene Gross[31] and Lev Pitaevskii[32], is a mean-field theory where all particles are assumed to be inside the same single-particle state, i.e., the condensate state [33]. Thus, the many-body state with N bosons can be written as a symmetric product of single-particle wave functions as

$$\Psi\left(\tilde{\boldsymbol{r}}_1, \tilde{\boldsymbol{r}}_2, \ldots, \tilde{\boldsymbol{r}}_N\right) = \prod_{i=1}^{N} \phi^{(3)}\left(\tilde{\boldsymbol{r}}_i\right), \tag{2.1}$$

where the wave function $\phi^{(3)}(\tilde{\boldsymbol{r}})$ is normalized to 1.

The two-body interaction between atoms in the condensate $U_{\text{eff}}(\tilde{\boldsymbol{r}}_i, \tilde{\boldsymbol{r}}_j)$ will be treated as a contact interaction with s-wave scattering length a_s[1]. Then, the Hamiltonian of the many-body system with N-many bosons, each of which has mass m, becomes as

$$H = \sum_{i=1}^{N} \left[\frac{\tilde{\boldsymbol{p}}_i^2}{2m} + V_{\text{3D}}\left(\tilde{\boldsymbol{r}}_i\right)\right] + \tilde{g}_{\text{3D}} \sum_{i<j} \delta\left(\tilde{\boldsymbol{r}}_i - \tilde{\boldsymbol{r}}_j\right), \tag{2.2}$$

where $V_{\text{3D}}(\tilde{\boldsymbol{r}})$ is the external potential, and $\tilde{g}_{\text{3D}} = 4\pi\hbar^2 a_s/m$ is the three-dimensional (3D) interaction strength. The expected energy of the mean-field state (2.1) is easily calculated as

$$E = N \int d^3r \left(\frac{\hbar^2}{2m}|\tilde{\nabla}\phi^{(3)}(\tilde{\boldsymbol{r}})|^2 + V_{\text{3D}}(\tilde{\boldsymbol{r}})|\phi^{(3)}(\tilde{\boldsymbol{r}})|^2 + \frac{(N-1)}{2}\tilde{g}_{\text{3D}}|\phi^{(3)}(\tilde{\boldsymbol{r}})|^4\right). \tag{2.3}$$

We scale the wave function $\phi^{(3)}(\tilde{\boldsymbol{r}})$ as $\phi^{(3)}(\tilde{\boldsymbol{r}}) \to \frac{1}{\sqrt{N}}\phi^{(3)}(\tilde{\boldsymbol{r}})$ to associate the particle density $n(\tilde{\boldsymbol{r}})$ as

$$n(\tilde{\boldsymbol{r}}) = |\phi^{(3)}(\tilde{\boldsymbol{r}})|^2 \tag{2.4}$$

since the normalization of the wave function changes to

$$\int d^3r|\phi^{(3)}(\tilde{\boldsymbol{r}})|^2 = N. \tag{2.5}$$

In this way, the energy of the system can be written without explicit dependence on the particle number N if the number is very large, that is, $N \gg 1 \implies N-1 \approx N$:

$$E_{GP}^{(3D)}[\phi^{(3)}, \phi^{(3)*}] = \int d^3r \left(\frac{\hbar^2}{2m}|\tilde{\nabla}\phi^{(3)}(\tilde{\boldsymbol{r}})|^2 + V_{\text{3D}}(\tilde{\boldsymbol{r}})|\phi^{(3)}(\tilde{\boldsymbol{r}})|^2 + \frac{\tilde{g}_{\text{3D}}}{2}|\phi^{(3)}(\tilde{\boldsymbol{r}})|^4 \right). \tag{2.6}$$

The obtained energy functional is called the GP energy in 3D. In order to find the state $\phi^{(3)}(\tilde{\boldsymbol{r}})$ that minimizes the energy E_{GP}, we use the calculus of variations. We search for the minimum energy such that the deviation in energy δE_{GP} becomes zero. We should also pay attention to the particle number constraint introduced in Eq. (2.5). The deviation in the wave function should not violate the normalization because, in our model, we take into account a fixed number of particles in the condensate. Thus, we should minimize the quantity $E - \tilde{\mu}_{\text{3D}}N$ with $\tilde{\mu}_{\text{3D}}$ being a Lagrange multiplier. The small change $\delta E_{GP} - \tilde{\mu}_{\text{3D}}\delta N$ can be obtained by small deviations in the wave-functions $\delta\phi^{(3)}$ and $\delta\phi^{(3)*}$ around the solutions $\phi^{(3)}$ and $\phi^{(3)*}$, respectively. In order to obtain $\delta E - \tilde{\mu}_{\text{3D}}\delta N = 0$ for all possible small deviations $\delta\phi^{(3)*}$ and $\delta\phi^{(3)}$, the solutions $\phi^{(3)}$ and $\phi^{(3)*}$ should satisfy the following equation and its complex conjugate, respectively:

$$\frac{-\hbar^2}{2m}\tilde{\nabla}^2\phi^{(3)}(\tilde{\boldsymbol{r}}) + V_{\text{3D}}(\tilde{\boldsymbol{r}})\phi^{(3)}(\tilde{\boldsymbol{r}}) + \tilde{g}_{\text{3D}}|\phi^{(3)}(\tilde{\boldsymbol{r}})|^2\phi^{(3)}(\tilde{\boldsymbol{r}}) = \tilde{\mu}_{\text{3D}}\phi^{(3)}(\tilde{\boldsymbol{r}}). \tag{2.7}$$

The equation obtained above is called the time-independent GP equation. It will be a valid approximation as long as the effective potential U_{eff} is a good approximation for the two-body interactions in the system, and the particle number in the condensate is nearly the same as the total number of particles, which is ensured in the weakly interacting systems.

2.1.2 BEC in Traps and Dimensional Reduction

In experimental settings, BECs are typically confined using external trapping potentials, often harmonic in form. When the trap is strongly anisotropic, the motion of particles along one or more spatial directions can be effectively frozen out, and the

condensate behaves as a lower-dimensional system. To illustrate this, consider a 3D anisotropic harmonic trap described by the potential

$$V_{\text{3D}}(\tilde{x},\tilde{y},\tilde{z}) = \frac{m\tilde{\omega}_x^2}{2}\tilde{x}^2 + \frac{m\tilde{\omega}_y^2}{2}\tilde{y}^2 + \frac{m\tilde{\omega}_z^2}{2}\tilde{z}^2. \tag{2.8}$$

When the trapping strength is large enough so that the interaction energy per particle, $\tilde{g}_{\text{3D}}n$, is much smaller than the energy spacing $\hbar\tilde{\omega}_z$ between trap levels in the $\tilde{z}$-direction, the condensate remains in the ground state of the harmonic potential along $\tilde{z}$, and we can write the 3D wavefunction as [18]

$$\phi^{(3)}(\tilde{\boldsymbol{r}}) = \phi^{(2)}(\tilde{\boldsymbol{r}}_\perp)\,\frac{1}{\pi^{1/4}a_z^{1/2}}\exp\left(-\frac{\tilde{z}^2}{2a_z^2}\right), \tag{2.9}$$

where $a_z = \sqrt{\hbar/m\tilde{\omega}_z}$ is the harmonic oscillator length in the $\tilde{z}$-direction, and $\tilde{\boldsymbol{r}}_\perp$ is the position vector inside the $\tilde{x}\tilde{y}$-plane. We note that the spatial extent of the condensate in each direction is assumed to be still much larger than the scattering length a_s, allowing us to use the contact interaction approximation for the two-body interaction. Substituting this ansatz into the 3D GP energy functional in Eq. (2.6) and integrating over the $\tilde{z}$-direction yields the effective 2D GP energy functional [34]:

$$E_{GP}^{(2D)}[\phi^{(2)},\phi^{(2)*}] = \int d^2\tilde{r}_\perp\left(\frac{\hbar^2}{2m}|\tilde{\nabla}_\perp\phi^{(2)}|^2 + V_{2D}(\tilde{x},\tilde{y})|\phi^{(2)}|^2 + \frac{\hbar\tilde{\omega}_z}{2}|\phi^{(2)}|^2 + \frac{\tilde{g}_{\text{3D}}}{\sqrt{2\pi}a_z}\frac{1}{2}|\phi^{(2)}|^4\right), \tag{2.10}$$

where $V_{2D}(\tilde{x},\tilde{y}) = \frac{m\tilde{\omega}_x^2}{2}\tilde{x}^2 + \frac{m\tilde{\omega}_y^2}{2}\tilde{y}^2$.

Minimizing $E_{GP}^{(2D)}$ with respect to $\phi^{(2)*}$ while keeping N fixed leads to the time-independent 2D GP equation:

$$\frac{-\hbar^2}{2m}\tilde{\nabla}_\perp^2\phi^{(2)}(\tilde{\boldsymbol{r}}_\perp) + V_{\text{2D}}(\tilde{\boldsymbol{r}}_\perp)\phi^{(2)}(\tilde{\boldsymbol{r}}_\perp) + \tilde{g}_{\text{2D}}|\phi^{(2)}(\tilde{\boldsymbol{r}}_\perp)|^2\phi^{(2)}(\tilde{\boldsymbol{r}}_\perp) = \tilde{\mu}_{\text{2D}}\phi^{(2)}(\tilde{\boldsymbol{r}}_\perp), \tag{2.11}$$

where the effective 2D interaction strength and chemical potential are

$$\tilde{\mu}_{\text{2D}} = \tilde{\mu}_{\text{3D}} - \frac{\hbar\tilde{\omega}_z}{2}, \tag{2.12}$$

$$\tilde{g}_{\text{2D}} = \frac{\sqrt{8\pi}\hbar^2 a_s}{ma_z}. \tag{2.13}$$

To obtain the time-dependent version of the GP equation, we start from the Lagrangian formulation $L = T - E_{GP}^{(2D)}$, where the kinetic term is

$$T = \frac{\mathrm{i}\hbar}{2}\int \mathrm{d}^2\tilde{r}_\perp\,\left(\phi^{(2)*}\dot{\phi^{(2)}} - \phi^{(2)}\dot{\phi^{(2)}}^*\right), \tag{2.14}$$

where the notation $\dot{\psi}$ represents the partial derivative of a function ψ with respect to time $\tilde{t}$. The Euler-Lagrange equations for the wavefunction $\phi^{(2)}$ can be found by applying functional derivatives to the Lagrangian L. Thus, the wavefunction $\phi^{(2)}(\tilde{\boldsymbol{r}}_\perp, \tilde{t})$ that maximizes the Lagrangian L satisfies the following time-dependent equation:

$$\mathrm{i}\hbar\frac{\partial\phi^{(2)}}{\partial\tilde{t}} = -\frac{\hbar^2}{2m}\tilde{\nabla}_\perp^2\phi^{(2)} + V_{\mathrm{2D}}(\tilde{\boldsymbol{r}}_\perp)\phi^{(2)} + \tilde{g}_{\mathrm{2D}}|\phi^{(2)}|^2\phi^{(2)}, \tag{2.15}$$

which is referred to as the time-dependent 2D GP equation.

We now consider a further dimensional reduction: If $\tilde{\omega}_y \gg \tilde{\omega}_x$, the condensate is tightly confined in the $\tilde{y}$-direction and approximately Gaussian as $\phi^{(2)}(x,y) = \phi^{(1)}(x)\frac{1}{\sqrt[4]{\pi a_y^2}}e^{-\tilde{y}^2/2a_y^2}$ with $a_y = \sqrt{\hbar/m\tilde{\omega}_y}$. Integrating out the $\tilde{y}$-direction in the 2D GP energy functional, we obtain the effective 1D GP energy:

$$E_{GP}^{(\mathrm{1D})}[\phi^{(1)}, \phi^{(1)*}] = \int_{-\infty}^{\infty}\mathrm{d}\tilde{x}\left(\frac{\hbar^2}{2m}\left|\frac{\mathrm{d}\phi^{(1)}}{\mathrm{d}\tilde{x}}\right|^2 + \frac{m\tilde{\omega}_x^2}{2}\tilde{x}^2|\phi^{(1)}|^2 + \frac{\tilde{g}_{\mathrm{1D}}}{2}|\phi^{(1)}|^4\right), \tag{2.16}$$

with effective 1D coupling

$$\tilde{g}_{\mathrm{1D}} = \frac{\tilde{g}_{\mathrm{2D}}}{\sqrt{2\pi}a_y} = \frac{2\hbar^2 a_s}{m a_z a_y}. \tag{2.17}$$

The corresponding time-independent 1D GP equation becomes

$$-\frac{\hbar^2}{2m}\frac{\mathrm{d}^2}{\mathrm{d}\tilde{x}^2}\phi^{(1)} + \frac{m\tilde{\omega}_x^2\tilde{x}^2}{2}\phi^{(1)} + \tilde{g}_{\mathrm{1D}}|\phi^{(1)}|^2\phi^{(1)} = \tilde{\mu}_{\mathrm{1D}}\phi^{(1)}, \tag{2.18}$$

where $\tilde{\mu}_{\mathrm{1D}} = \tilde{\mu}_{\mathrm{2D}} - \frac{\hbar\tilde{\omega}_y}{2}$.

2.1.3 Dimensionless Form of the GP Equations

To simplify analysis and numerical simulations, we non-dimensionalize the GP equations. For the 2D case, we will take the unit length as the harmonic oscillator length a_x and the unit energy as $\hbar\tilde{\omega}_x$; thus, we scale every position as $\tilde{\boldsymbol{r}}_\perp \to a_x\boldsymbol{r}_\perp$ and chemical potential as $\tilde{\mu}_{\mathrm{2D}} \to \hbar\tilde{\omega}_x\mu$, and the wavefunction as $\phi^{(2)} \to a_x^{-1}\psi = \sqrt{\frac{m\tilde{\omega}_x}{\hbar}}\psi$ to preserve the normalization to N. The resulting dimensionless form of the 2D GP energy functional and the corresponding time-independent 2D GP equation becomes

$$E_{GP}[\psi,\psi^*] = \int d^2r_\perp\left(\frac{1}{2}|\nabla_\perp\psi|^2 + \left(\frac{x^2}{2} + \frac{\omega^2y^2}{2}\right)|\psi|^2 + \frac{g}{2}|\psi|^4\right), \tag{2.19}$$

$$-\frac{1}{2}\nabla_\perp^2\psi + \left(\frac{x^2}{2} + \frac{\omega^2y^2}{2}\right)\psi + g|\psi|^2\psi = \mu\psi, \tag{2.20}$$

where $g = \sqrt{8\pi}\frac{a_s}{a_z}$ is the dimensionless 2D interaction strength and $\omega = \tilde{\omega}_y/\tilde{\omega}_x$ is the anisotropy ratio. The corresponding time-dependent equation is obtain by scaling time $\tilde{t} \to \tilde{\omega}_x^{-1}t$:

$$-\frac{1}{2}\nabla_\perp^2\psi + \left(\frac{x^2}{2} + \frac{\omega^2 y^2}{2}\right)\psi + g|\psi|^2\psi = \mathrm{i}\frac{\partial}{\partial t}\psi. \tag{2.21}$$

The dimensionless form of the 1D GP equation, however, becomes

$$-\frac{1}{2}\frac{\mathrm{d}^2}{\mathrm{d}x^2}\psi^{(1)} + \frac{x^2}{2}\psi^{(1)} + g_{1\mathrm{D}}|\psi^{(1)}|^2\psi^{(1)} = \mu_{1\mathrm{D}}\psi^{(1)}, \tag{2.22}$$

where $g_{1\mathrm{D}} = 2\frac{a_s a_x}{a_z a_y}$ is the dimensionless 1D interaction strength and $\mu_{1\mathrm{D}} = \mu - \omega/2$ is the effective dimensionless chemical potential in 1D.

2.1.4 Thomas-Fermi approximation

For sufficiently large clouds, an accurate expression for the ground-state energy may be obtained by neglecting the kinetic energy term in the GP equation [1]. From Eq.(2.20), one approximates that the large clouds satisfy

$$\left(\frac{x^2}{2} + \frac{\omega^2 y^2}{2} + g|\psi|^2\right)\psi \approx \mu\psi \tag{2.23}$$

in the region where both side has the same sign; in other words, the left side is greater than zero. Hence, we write 2D Thomas-Fermi (TF) density as

$$n_{2\mathrm{DTF}}(\boldsymbol{r}_\perp) = |\psi(\boldsymbol{r}_\perp)|^2 = \frac{1}{g}\left(\mu - \frac{x^2}{2} - \frac{\omega^2 y^2}{2}\right)\Theta(2\mu - x^2 - \omega^2 y^2), \tag{2.24}$$

where Θ is the Heavisede theta function.

The boundary of the cloud is therefore given by

$$V(\boldsymbol{r}_\perp) = \frac{x^2}{2} + \frac{\omega^2 y^2}{2} = \mu,$$

which corresponds to an ellipse with major and minor axes being respectively defined

$$R_x = \sqrt{2\mu} \quad \text{and} \quad R_y = \frac{\sqrt{2\mu}}{\omega}. \tag{2.25}$$

Spatial integral of 2D TF density gives the number of particles in the condensate state, and we calculate the chemical potential and TF radii in terms of the number of atoms

N, the anisotropy ω, and the interaction strength g as

$$\mu = \sqrt{\frac{gN\omega}{\pi}}. \tag{2.26}$$

The validity of this model depends on the TF radii being significantly larger than the healing length ξ, which is defined as the length scale at which the density changes. The healing length can be approximated around the center using the central density $n_{\text{2DTF}}(0) = \mu/g$ as in Ref. [1]:

$$\frac{1}{2\xi^2} \approx g\, n_{\text{2DTF}}(0) = \mu \implies \xi = \frac{1}{\sqrt{2\mu}}. \tag{2.27}$$

Thus, the validity of TF density has two criteria:

$$R_x \gg \xi \implies gN \gg \frac{\pi}{4\omega}, \tag{2.28}$$

$$R_y \gg \xi \implies gN \gg \frac{\pi}{4}\omega. \tag{2.29}$$

In the large anisotropy limit, the condensate wavefunction may have a Gaussian profile along the squeezed y-direction and a TF profile along the x-direction, as discussed in Sec. 2.1.3. We will refer to this regime as 1D TF and use the effective 1D GP equation (2.22) to represent the x-dependent part of the condensate wavefunction. The approximated 1D TF density has an inverse parabola in the x-direction:

$$|\psi^{(1)}(x)|^2 \approx \frac{1}{g_{\text{1D}}}\left(\mu_{\text{1D}} - \frac{x^2}{2}\right)\Theta(2\mu_{\text{1D}} - x^2). \tag{2.30}$$

The integration of the 1D TF density leads to the relation of μ_{1D} in terms of physical quantities as

$$\mu_{\text{1D}} = \left(\frac{9N^2 g_{\text{1D}}^2}{32}\right)^{1/3} = \left(\frac{9\omega N^2 g^2}{64\pi}\right)^{1/3}. \tag{2.31}$$

We now examine 2D condensate wavefunction in two distinct limits: (i) low anisotropy limit where 2D TF can be used and (ii) large anisotropy limit where only x-compınent of the wavefunction is in TF limit.

$$\psi_{\text{2DTF}}(x,y) = \sqrt{\frac{\mu}{g} - \frac{x^2}{2g} - \frac{y^2\omega}{2g}}\Theta(2\mu - x^2 - \omega^2 y^2), \tag{2.32a}$$

$$\psi_{\text{1DTF}}(x,y) = \sqrt[4]{\frac{\omega}{\pi}} e^{-\omega y^2/2}\sqrt{\frac{\mu_{\text{1D}}}{g_{\text{1D}}} - \frac{x^2}{2g_{\text{1D}}}}\Theta(2\mu_{\text{1D}} - x^2). \tag{2.32b}$$

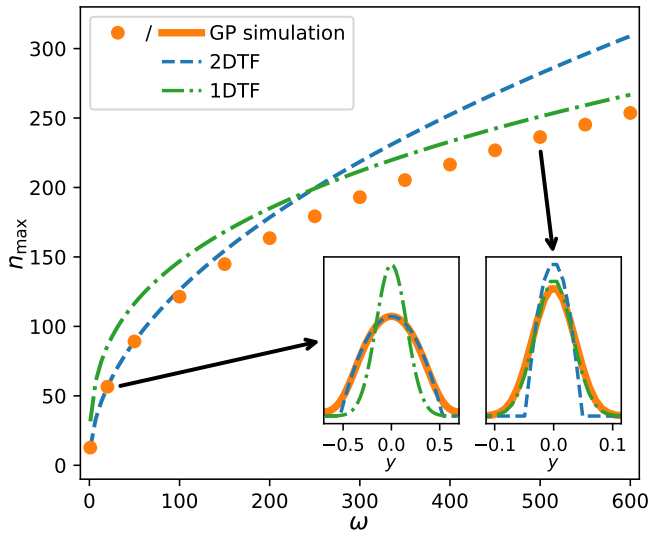

Figure 2.1: The maximum density $n_{\max}$ as a function of the anisotropy ratio ω for $gN = 400$. Numerically obtained GP simulations (dots) follow the 2D TF (dashed) approximation for smaller anisotropies and the 1D TF (dash-dotted) in the large anisotropy limit. The insets display cross-sections of the density profile along the y-axis for selected values of ω, demonstrating the crossover from the 2D TF to the 1D TF regime in large anisotropies. The numerical method used to obtain the ground states in GP simulations with Wick rotation of time $t \to -\mathrm{i}\tau$ is discussed in Sec.3.1.5

We note that we use the definition of the anisotropy ratio $\omega = \tilde{\omega}_y/\tilde{\omega}_y = a_x^2/a_y^2$. Therefore, the two maximum TF densities become

$$n_{\mathrm{2DTF}}(0,0) = \sqrt{\frac{N\omega}{\pi g}} \quad \text{and} \quad n_{\mathrm{1DTF}}(0,0) = \left(\frac{9\omega N^2}{16\sqrt{2}\pi g}\right)^{1/3} \tag{2.33}$$

The intersection point of the two analytical expressions for $n_{\mathrm{2DTF}}(0)$ and $n_{\mathrm{1DTF}}(0)$ gives the crossover occurs at transition ansiotropy as

$$\omega_s = \pi \left(\frac{9}{16\sqrt{2}}\right)^2 gN \simeq 0.497\, gN. \tag{2.34}$$

In Figure 2.1, we plot the central density obtained from numerical simulations as a function of the anisotropy parameter ω. The results clearly reveal a crossover from the 2D TF to the 1D TF regime. For small anisotropies, the numerics closely follow the 2D TF scaling, whereas for large anisotropies, the behavior transitions to match the 1D TF prediction.

2.1.5 Solitons

Solitons, otherwise known as solitary waves, are a special type of excitation solutions that arise from non-linear wave equations. They maintain their shape by balancing the effects of dispersion and non-linearity. In self-defocusing (repulsive) non-linear media, solitons are characterized by a dip in density and a change in the phase of the solution around the soliton's position. These structures are observed in optical experiments as dark sections of the density. This is why they are called dark solitons[6, 1, 5]. However, we only refer to the solution with density becoming exactly zero at the soliton position and a $\pi-$phase jump instead of a smooth change in the phase when we use the term dark soliton in this study. Such structures can be obtained in various nonlinear media, such as optical fibers[35, 36], thin magnetic thin films[37], and cold atom condensates[5].

To derive the mathematical form of a soliton in 1D, we follow the calculations in Ref. [1] and consider a wave function in the form of

$$\psi(x,t) = f(x-ut)e^{-\mathrm{i}\mu t}$$

with properly scaled physical quantities $x, t, \mu...$ One can notice that the mentioned wave function can satisfy the 1D GP equation without any external confinement, i.e., $V(x) = 0$:

$$\mu f - \mathrm{i}uf' = -\frac{1}{2}f'' + g|f|^2 f, \tag{2.35}$$

where we denote the spatial derivative of the function f as f'. We will assume such a moving wave will transform to a spatially constant form at infinities $x \to \pm\infty$ as

$$|\psi|^2 \to \frac{\mu}{g} =: n_0. \tag{2.36}$$

We rewrite the complex function using two real-valued functions as

$$f(x-ut) = \sqrt{n_0}\Big(f_1(x-ut) + \mathrm{i}f_2(x-ut)\Big), \tag{2.37}$$

with the limiting form

$$f_1^2 + f_2^2 \to 1 \quad \text{as} \quad x \to \pm\infty.$$

The equation obtained in (2.35) can be written in real and imaginary parts as

$$+uf_2' = -\frac{1}{2}f_1'' + \mu(f_1^2 + f_2^2 - 1)f_1$$
$$-uf_1' = -\frac{1}{2}f_2'' + \mu(f_1^2 + f_2^2 - 1)f_2$$

We take the imaginary part of the wavefunction f_2 constant as in Ref. [1]. The equations above transform to

$$f_1'' = \mu 2 f_1 \left(f_1^2 + f_2^2 - 1\right) \tag{2.38a}$$
$$f_1' = \frac{\mu f_2}{u}\left(1 - f_1^2 - f_2^2\right) \tag{2.38b}$$

Taking the derivative of the second equation (2.38b) and making a comparison with the first one leads to the relation for constant f_2 as

$$f_2 = \frac{u}{\sqrt{\mu}}$$

Before solving the differential equation, we make slight modifications:

$$f_1' = \sqrt{\mu} f_0^2 \left(1 - \left(\frac{f_1}{f_0}\right)^2\right) \quad \text{where} \quad f_0 := \sqrt{1 - f_2^2}.$$
$$\implies \frac{1}{\sqrt{\mu} f_0}\frac{\mathrm{d}}{\mathrm{d}x}\left(\frac{f_1}{f_0}\right) = 1 - \left(\frac{f_1}{f_0}\right)^2.$$

Transforming $x \to \bar{x}/\sqrt{\mu} f_0$, we obtain the differantial equation of $\tanh(\bar{x})$ for f_1/f_0. This concludes our calculation: The soliton state is defined as

$$\psi_s(x,t) = \left(\sqrt{n_0}\sqrt{1 - \frac{u^2}{n_0 g}}\tanh\left(\frac{x - ut}{\xi_s}\right) + \mathrm{i}\frac{u}{\sqrt{g}}\right) e^{-\mathrm{i}g n_0\, t}, \tag{2.39}$$

where

$$\xi_s = \frac{1}{\sqrt{\mu - u^2}} \tag{2.40}$$

is the dimensionless soliton healing length.

We refer to the stationary solitons, with $u = 0$, as dark solitons in the remainder of this thesis, and investigate their stabilities both analytically and numerically in Chapter 4.

2.1.6 Bose Gas in Rotating Traps

In a reference frame rotating with angular velocity $\boldsymbol{\Omega} = \Omega\hat{\boldsymbol{z}}$ around the z-axis, where Ω is dimensionless rotating frequency in units of $\tilde{\omega}_x$, the system's Hamiltonian transforms to [38, 2].

$$H^{(\Omega)} = H - \boldsymbol{\Omega} \cdot \boldsymbol{L}, \tag{2.41}$$

where

$$\boldsymbol{L} = \boldsymbol{r}_\perp \times (-\mathrm{i}\nabla_\perp)$$

is the dimensionless angular momentum operator. The contribution to the Hamiltonian is calculated directly as

$$\boldsymbol{\Omega} \cdot \boldsymbol{L} = -\mathrm{i}\Omega \left(x \frac{\partial}{\partial y} - y \frac{\partial}{\partial x} \right).$$

Hence, the one-body part of the Hamiltonian in Eq. (2.21) can be rewritten as

$$\begin{aligned} H_0^{(\Omega)} &= -\frac{1}{2}\nabla_\perp^2 + \frac{1}{2}(x^2 + \omega^2 y^2) + \mathrm{i}\Omega \left(x \frac{\partial}{\partial y} - y \frac{\partial}{\partial x} \right) \\ &= \frac{1}{2}\left((p_x + \Omega y)^2 + (p_y - \Omega x)^2 \right) + \frac{1}{2}(1 - \Omega^2)x^2 + \frac{1}{2}(\omega^2 - \Omega^2)y^2, \end{aligned} \tag{2.42}$$

where

$$p_x = -\mathrm{i}\frac{\partial}{\partial x} \quad \text{and} \quad p_y = -\mathrm{i}\frac{\partial}{\partial y}$$

are dimensionless momentum operators in 2D space. The kinetic part of this Hamiltonian is equivalent to that of a particle with charge q in an effective gauge field $\boldsymbol{A} = A_x\hat{i} + A_y\hat{j}$, where the components of the vector field satisfy the following equations:

$$qA_x = -\Omega y, \tag{2.43a}$$

$$qA_y = +\Omega x. \tag{2.43b}$$

The corresponding effective magnetic field applied to the Bose gas satisfies the equality

$$q\boldsymbol{B} = q\nabla_\perp \times \boldsymbol{A} = 2\boldsymbol{\Omega}. \tag{2.44}$$

This correspondence implies that the Coriolis force in the rotating frame plays the same role as the Lorentz force on a charged particle in a uniform magnetic field [2].

In fact, throughout this context, "rotation" and "magnetic field" are often used interchangeably when referring to this equivalence. Therefore, we can create a synthetic magnetic field that can be felt by electrically neutral Bose atoms.

When the condensate is rotated above a critical threshold, singular vortices form with quantized circulations. At higher rotation rates, more vortices appear [39] and eventually arrange into a triangular lattice of singularities [14, 15, 40] similar to Abrikosov vortex lattice in type-II superconductors under strong magnetic fields [41]. The number of vortices formed in the condensate increases with Ω, given approximately by [3]

$$N_{\mathrm{v}}(\Omega) \approx n_v \pi R_{\perp}^2(\Omega) = \Omega R_{\perp}^2(\Omega). \tag{2.45}$$

In the rotating frame, the effective radial confinement is reduced to $\frac{1}{2}(1-\Omega^2)r^2$ in the isotropic setups, i.e., $\omega = 1$. The centrifugal effect reduces the radial trapping strength, causing the condensate to expand radially, and due to conservation of the number of atoms, this radial expansion is accompanied by compression along the rotation axis. Additionally, TF energy functional and resulting density profiles remain formally similar to the non-rotating case, but now with a modified radial potential. This leads to a rotation-dependent chemical potential [3]:

$$\mu_{\mathrm{TF}}(\Omega) = \mu_{\mathrm{TF}}(0)\,(1-\Omega)^{2/5}\,. \tag{2.46}$$

As Ω approaches unity, the radial confinement effectively vanishes, causing both the chemical potential and central density $\mu_{\mathrm{TF}}(\Omega)/g$ to decrease toward zero. The radial extent of the condensate also grows with increasing rotation, scaling as [39, 18, 3]

$$\frac{R_{\perp}(\Omega)}{R_{\perp}(0)} = \left(1-\Omega^2\right)^{-3/10}, \tag{2.47}$$

illustrating the dilating effect of the centrifugal force.

In the regime where the vortex density becomes comparable to the particle density, the system enters a strongly correlated phase [2]. Theoretical studies predict that such states are bosonic analogues of the FQH states observed in 2D electron gases under strong magnetic fields [16]. These systems can be viewed as bosonic analogues of the strongly correlated phases that exhibit the FQH effect of electrons in semiconductors[30]. Hence, these systems provide a clean platform to explore the physics of quantum Hall physics [30] in ultracold atomic setups.

2.2 Quantum Hall States

In 1880 [42], Hall discovered that electronic systems produce a perpendicular current to the external electric field under the influence of a magnetic field. The transverse conductivity σ_{xy} of the produced current is observed to be inversely proportional to the magnetic field strength B. However, in the regime of strong magnetic fields and low temperatures, it was observed that the transverse conductivity was quantized at special values in the form of [30]

$$\sigma_{xy} = \nu \frac{e^2}{h}.$$

The discovery of integer (where $\nu \in \mathbb{Z}$) [43] and fractional (where ν is a certain fraction, such as $\frac{1}{3}, \frac{2}{5} \dots$) [44] quantization of the transverse conductivity and their theoretical explanations [45, 46] led to a paradigm shift in our understanding of phases of matter and phase transitions. These systems are no longer characterized solely by symmetry breaking and local order parameters, but also by topological order[47]—a form of quantum order showing long-range entanglement, emergent gauge structures and emergent quasiparticles with fractional charge and anyonic statistics[48] offering a promising platform for topological quantum computation[49].

In this section, we will show simple non-interacting models used in the investigation of these interesting systems. First, we focus on integer quantum Hall (IQH) systems. We derive the Landau levels for two gauge fields and discuss their importance in describing IQH systems. Then, we will comment on FQH, which is a more sophisticated setup and the target of this thesis. We present a toy model wavefunction to represent such a system in the small-particle limit, as suggested by Laughlin.

2.2.1 Integer Quantum Hall Effect and Landau Levels

The IQH effect is a striking manifestation of quantum mechanics in 2D electron systems subject to strong perpendicular magnetic fields. It is characterized by the quantization of the Hall conductivity in integer multiples of e^2/h, independent of microscopic sample details. This quantization in the transverse conductivity σ_{xy} is extraordinarily precise and robust against disorder and sample imperfections, making

it an essential tool for resistance metrology [30]. A fundamental understanding of the IQH effect begins with the behavior of non-interacting electrons confined to two dimensions in the presence of a strong magnetic field, which leads to the formation of discrete energy levels known as Landau levels [50, 51].

2.2.1.1 Landau Gauge

In this subsection, we will follow the derivations shown in the Ref.[51]. In the Landau gauge, the vector potential is chosen as

$$\boldsymbol{A} = -By\,\hat{x},$$

which satisfies the magnetic field $\boldsymbol{B} = B\hat{z}$ perpendicular to the system plane. Then, the single-particle Hamiltonian for a particle of charge q and mass m in such a magnetic field is written as

$$H = \frac{1}{2m}\left[(p_x + qBy)^2 + p_y^2\right]. \tag{2.48}$$

Due to translational invariance in the x-direction, or the vanishing commutation relation

$$[H, p_x] = 0,$$

momentum becomes a good quantum number labeling the quantum states of the Hamiltonian (2.48). In other words, any eigenstate $\varphi(x, y)$ of the Hamiltonian $\hat{H}$ is also an eigenstate of the momentum operator p_x; thus, it has a planewave characteristic along the x-direction. Let us write the wavefunction as

$$\varphi(x, y) = \varphi_k(x, y) = e^{\mathrm{i}kx}\phi_k(y),$$

which reduces the problem to a 1D harmonic oscillator in y with the effective Schrödinger equation

$$H\varphi_k = H(e^{\mathrm{i}kx}\phi_k) = e^{\mathrm{i}kx}H_k\phi_k = e^{\mathrm{i}kx}\epsilon_k\phi_k$$

where

$$H_k = -\frac{\hbar^2}{2m}\frac{d^2}{dy^2} + \frac{m\omega_c^2}{2}(y + k\ell_B^2)^2,$$

where $\ell_B = \sqrt{\hbar/eB}$ is the magnetic length and $\omega_c = \sqrt{qB/m}$ is cyclotron frequency. This is a quantum harmonic oscillator centered at $y_k = -k\ell_B^2$ oscillating

with frequency ω_c. Thus, the normalized eigenfunctions of the Hamiltonian (2.48) are [52]

$$\varphi_{n,k}(x,y) = \frac{1}{\sqrt{L_x}} e^{ikx} \frac{1}{\sqrt{2^n n! \ell_B \sqrt{\pi}}} H_n\left(\frac{y + k\ell_B^2}{\ell_B}\right) e^{-\frac{1}{2\ell_B^2}(y+k\ell_B^2)^2}, \tag{2.49}$$

where H_n are the Hermite polynomials [53, 52], and L_x is the system size in the x-direction. The corresponding eigenvalues become

$$\epsilon_{n,k} = \hbar\omega_c \left(n + \frac{1}{2}\right).$$

The energy spectrum of the model has sharp peaks around distinct energy levels known as Landau levels, thanks to the massive degeneracy of each level.

Adopting a periodic boundary condition along the x-direction, the wavenumbers k's are quantized as

$$k = \frac{2\pi}{L_x}\bar{n}, \tag{2.50}$$

where $\bar{n}$ is an integer. Each value of $k = k_{\bar{n}}$ corresponds to a different guiding center $y_k = y_{\bar{n}}$, so the allowed $k_{\bar{n}}$ values are constrained by the system size L_y such that the guiding center is located inside the system:

$$\frac{-L_y}{2} \leq y_{\bar{n}} \leq \frac{L_y}{2} \implies \frac{-N_v}{2} \leq \bar{n} \leq \frac{N_v}{2},$$

where

$$N_\phi = \frac{L_x L_y}{2\pi\ell_B^2} \tag{2.51}$$

is referred to as the number of magnetic flux quanta in the system because the right-hand side of the equation can be obtained as a ratio of the total magnetic flux $\Phi = BL_xL_y$ in the system to the magnetic flux quanta $\Phi_0 = h/q$ for a q charged particle [51]. We note that the quantization of wavenumbers $k_{\bar{n}}$ makes the degeneracy of each Landau level $N_\phi + 1$ controlled linearly by the magnetic strength B or the area of the 2D system L_xL_y; therefore, in the thermodynamic limit, we conclude with a large degeneracy for each level.

When the number of particles N is equal to an integer multiple of the degeneracy $N_\phi + 1$, the filling factor $\nu = \frac{N}{N_\phi+1}$ becomes an integer. We deliberately denote the filling factor with ν because it is the same quantity seen in the transverse conductivity in the previous section. Hence, whenever ν-many Landau levels are filled in the 2D

system, the Hall response σ_{xy} becomes integer multiply of the conductance quanta e^2/h, or more precisely

$$\sigma_{xy} = \nu \frac{e^2}{h}.$$

2.2.2 Fractional Quantum Hall Effect and Laughlin State

FQH states cannot be explained using non-interacting theories. Instead, they reflect strong electron correlations, giving rise to emergent phenomena such as fractional charge of excitations, anyonic statistics, topological order, long-range entanglement, incompressibility, and a finite excitation gap to neutral and charged modes [30, 48, 51].

Laughlin's proposal for the ground state wavefunction at filling fraction $\nu = 1/m$ is:

$$\psi\left(z_i\right) = \prod_{i<j} \left(z_i - z_j\right)^m e^{-\sum_{i=1}^{n} |z_i|^2 / 4l_B^2}. \tag{2.52}$$

This wavefunction is clearly anti-symmetric when m is an odd integer. In the case of m being an even integer, it can be interpreted as a quantum Hall state for bosons [2, 4]. The pre-factor vanishes with a zero of order m whenever two electrons come together. At the same time, the exponential factor decreases rapidly whenever the electrons move too far from the origin. As a result, the wavefunction is peaked on configurations that balance these two effects [30].

Numerical simulations indicate that, for a small number of particles, this wavefunction has over 99% overlap with the true ground state, which arises from both Coulomb repulsion and several other repulsive potentials V [54].

In this thesis, we study a 2D bosonic system under effective magnetic fields as discussed in Sec. 2.1.6. Specifically, we found that the numerically obtained ground state exhibits a large overlap with the bosonic Laughlin wavefunction with $\nu = 1/2$, signaling compelling evidence that the system realizes a fractional quantum Hall phase characterized by topological order, incompressibility, and emergent anyonic excitations.

CHAPTER 3

NUMERICAL METHODS

3.1 Numerical Methods for Partial Differential Equations

To simulate the nonlinear partial differential equation given in Eq. (2.21), we begin by discretizing the continuous wavefunction $\psi(x, y, t)$ defined over a two-dimensional spatial domain. Our goal is to numerically evolve this function using various integration methods and compare their performance in this section.

3.1.1 Discretization of 2D wavefunction

We represent the continuous function $\psi(x, y, t)$ on a uniform rectangular 2D spatial grid. Specifically, we define a rectangular grid consisting of N_x points along the x-axis and N_y points along the y-axis. The grid spacing in each direction is denoted by Δx and Δy, respectively. The wavefunction $\psi(x, y, t)$ is then approximated by a matrix with elements $\psi_{i,j}(t)$, which represents the value of the function at a specific grid point:

$$\psi_{i,j}(t) \approx \psi(x_i, y_j, t)$$

with

$$x_i = i\,\Delta x, \quad \text{for } i = \frac{N_x}{2} - 1 \cdots - 1, 0, 1, \ldots, \frac{N_x}{2},$$

$$y_j = j\,\Delta y, \quad \text{for } j = \frac{N_y}{2} - 1 \cdots - 1, 0, 1, \ldots, \frac{N_y}{2},$$

where N_x and N_y are taken even integers.

This discretization results in a two-dimensional complex-valued matrix of shape (N_x, N_y), which evolves in time. The matrix structure allows us to apply finite difference meth-

ods or spectral methods (e.g., Fourier transforms) to compute spatial derivatives, and various time-stepping algorithms to evolve the wavefunction forward in time.

After spatial discretization of the GP wave function, the problem reduces to a system of coupled ordinary differential equations in the form

$$\mathrm{i}\frac{d\psi_{i,j}}{dt} = \hat{H}[\psi]_{i,j,k,l}\ \psi_{k,l}\ , \tag{3.1}$$

where $\hat{H}[\psi]$ is the GP operator that simulates the differential operation in Eq. (2.20). The repeating spatial indices are summed as the Einstein summation convention. We note that the obtained coupled differential equations are nonlinear because they explicitly depend on the applied state ψ itself.

Similar to the spatial coordinates, we need to discretize the time with small time steps Δt as

$$t_n = n\,\Delta t, \quad \text{for } n = 0, 1, 2, \dots\ ,$$

so that we can simulate the GP equation (2.21) or correspondingly Eq.(3.1). We use different methods to simulate the differential equation and explain them briefly in the following sections.

3.1.2 Central Finite Difference Method and Discretization of the 2D GPE

Firstly, we focus on the right-hand side of the Eq. (3.1), which simulates the differential operation seen in the GP equation (2.20). The Laplacian operator contains second-order derivatives, which we approximate using the central finite difference method. At a given grid point (i, j), the second derivative in the x-direction is:

$$\left.\frac{\partial^2\psi}{\partial x^2}\right|_{i,j} \approx \frac{\psi_{i+1,j} - 2\psi_{i,j} + \psi_{i-1,j}}{\Delta x^2},$$

and in the y-direction:

$$\left.\frac{\partial^2\psi}{\partial y^2}\right|_{i,j} \approx \frac{\psi_{i,j+1} - 2\psi_{i,j} + \psi_{i,j-1}}{\Delta y^2}.$$

Thus, the Laplacian becomes:

$$\nabla^2\psi_{i,j} \approx \frac{\psi_{i+1,j} - 2\psi_{i,j} + \psi_{i-1,j}}{\Delta x^2} + \frac{\psi_{i,j+1} - 2\psi_{i,j} + \psi_{i,j-1}}{\Delta y^2}. \tag{3.2}$$

Therefore, using the central finite difference approximation of the Laplacian, the 2D GP equation is approximated with the following algebraic equations between matrix indices:

$$i\frac{d\psi_{i,j}}{dt} = -\frac{1}{2}\left[\frac{\psi_{i+1,j} - 2\psi_{i,j} + \psi_{i-1,j}}{\Delta x^2} + \frac{\psi_{i,j+1} - 2\psi_{i,j} + \psi_{i,j-1}}{\Delta y^2}\right] + V_{i,j}\psi_{i,j} + g|\psi_{i,j}|^2\psi_{i,j}, \tag{3.3}$$

where $V_{i,j}$ gives the value of the 2D anisotropic potential at the space grid (x_i, y_i).

3.1.3 Forward Euler Method

The Forward Euler method is a simple yet fundamental technique for numerically integrating time-dependent partial differential equations. When applied to the time-dependent GP equation, it provides an explicit first-order time-stepping scheme [55, 56, 57]. In this method, the time derivative in Eq. (3.1) is approximated by a finite difference:

$$\left.\frac{\mathrm{d}\psi_{i,j}}{\mathrm{d}t}\right|_{t=t_n} \approx \frac{\psi_{i,j}^{n+1} - \psi_{i,j}^{n}}{\Delta t}, \tag{3.4}$$

where ψ^n denotes the matrix elements at time t_n. Substituting this into Eq. (3.1) and rearranging, we obtain the Forward Euler update rule:

$$\psi_{i,j}^{n+1} = \psi_{i,j}^{n} - i\Delta t\hat{H}[\psi^n]_{i,j,k,l}\ \psi_{k,l}^{n}. \tag{3.5}$$

This scheme is explicit; that is, the right-hand side of Eq. (3.5) depends only on the quantities evaluated at the current time step n, allowing ψ^{n+1} to be computed directly. We use the central finite difference method to discretize the Laplacian ∇^2 as in Eq (3.3) to construct the 4-tensor $\hat{H}[\psi^n]$ at every time step due to its non-linear behavior.

While the Forward Euler method offers low computational cost and ease of implementation, its first-order accuracy and conditional stability make it suitable primarily for short-time simulations or for testing purposes. In subsequent sections, we will consider more robust and accurate integrators.

3.1.4 Crank-Nicolson Method

The Crank–Nicolson method is another widely used time integration scheme for solving time-dependent partial differential equations, particularly those involving second-order spatial derivatives. Here, we approximate the time derivative in Eq. (3.1) using the centered difference:

$$\left.\frac{\mathrm{d}\psi_{i,j}}{\mathrm{d}t}\right|_{t=t_n+\Delta t/2} \approx \frac{\psi_{i,j}^{n+1}-\psi_{i,j}^{n}}{\Delta t}, \tag{3.6}$$

and evaluate the right-hand side of Eq.(3.1) at the midpoint in time using the trapezoidal rule:

$$\left.\frac{\mathrm{d}\psi_{i,j}}{\mathrm{d}t}\right|_{t=t_n+\Delta t/2} \approx \frac{1}{2}\left[\hat{H}[\psi^{n+1}]_{i,j,k,l}\,\psi_{k,l}^{n+1}+\hat{H}[\psi^{n}]_{i,j,k,l}\,\psi_{k,l}^{n}\right]. \tag{3.7}$$

Therefore, the update rule for the Crank-Nicolson method can be obtained as

$$\psi^{n+1}=\left(\hat{I}+\frac{\mathrm{i}\Delta t}{2}\hat{H}[\psi^{n+1}]\right)^{-1}\left(\hat{I}-\frac{\mathrm{i}\Delta t}{2}\hat{H}[\psi^{n}]\right)\psi^{n}\,, \tag{3.8}$$

where $\hat{I}$ is diagonal 4-tensor with indices $(\hat{I})_{i,j,k,l}=\delta_{i,k}\delta_{j,l}$ with $\delta_{i,j}$ is the Kronecker delta. This equation is implicit, since the wavefunction at the next time step, ψ^{n+1}, appears on both sides of the equation, so it becomes impossible to calculate the right-hand side before knowing the answer in the non-linear case, i.e., $g\neq 0$.

In the non-interacting ($g=0$) case, the non-linear part vanishes in Eq. (3.3); thus, we can construct the 4-tensor $\hat{H}$ without depending on the state ψ itself. We can obtain a new 4-tensor M as

$$M=\left(\hat{I}+\frac{\mathrm{i}\Delta t}{2}\hat{H}\right)^{-1}\left(\hat{I}-\frac{\mathrm{i}\Delta t}{2}\hat{H}\right)$$

and take repeatedly product of constant tensor M during the time evolution.

However, in the interacting case with $g\neq 0$, we need to approximate the next form of the state ψ^{n+1} in Eq. (3.8) using either iterative techniques or a split-step method. In this thesis, we do not investigate such methods. Even in the non-interacting case, however, the Crank-Nicolson method becomes inefficient from the computational time aspect.

3.1.5 Split-Step Fourier Method

We finally introduce the Split-Step Fourier Method, a spectral operator-splitting technique designed to treat the kinetic and potential (including nonlinear) contributions separately and efficiently.

To proceed, we first decompose the full Hamiltonian operator $\hat{H}$ into two parts,

$$\hat{H} = \hat{T} + \hat{V},$$

where $\hat{T} = -\frac{1}{2}\nabla^2$ represents the kinetic energy operator, and $\hat{V}$ is the potential operator containing the external potential and the nonlinear interaction,

$$\hat{V}[\psi]_{i,j} = V_{i,j} + g|\psi^n_{i,j}|^2$$

The formal solution to the evolution equation over a small time step Δt is

$$\psi^{n+1}_{i,j} = e^{-i\Delta t(\hat{T}+\hat{V})}\psi^n_{i,j}$$

Notice that time evolution under the potential operator $\hat{V}$ is diagonal for the 2D state ψ; thus, we can find the exponential time evolution matrix by just taking the exponentiation of the diagonal elements as

$$e^{-i\Delta t\hat{V}}\psi^n_{i,j} = e^{-i\Delta t\left(V_{i,j}+g|\psi^n_{i,j}|^2\right)}\psi^n_{i,j}$$

Similarly, the kinetic term in the Hamiltonian becomes diagonal when it is applied to the Fourier decomposition of the 2D state ψ. We define the discrete Fourier and the corresponding inverse Fourier decompositions as

$$\mathcal{F}[\psi]_{\alpha,\beta} = \tilde{\psi}_{\alpha,\beta} = \sum_{i,j} \psi_{i,j}\, e^{\mathrm{i}(x_i k^{(x)}_\alpha + y_j k^{(y)}_\beta)}, \tag{3.9a}$$

$$\mathcal{F}^{-1}[\tilde{\psi}]_{i,j} = \psi_{i,j} = \sum_{\alpha,\beta} \tilde{\psi}_{\alpha,\beta}\, e^{-\mathrm{i}(x_i k^{(x)}_\alpha + y_j k^{(y)}_\beta)}, \tag{3.9b}$$

where $k^{(x)}_\alpha$ and $k^{(y)}_\beta$ are discrete wavevectors defined as

$$k^{(x)}_\alpha = \frac{2\pi}{N_x\Delta x}\,\alpha, \quad \text{for } \alpha = \frac{N_x}{2} - 1 \cdots -1, 0, 1, \ldots, \frac{N_x}{2},$$

$$k^{(y)}_\beta = \frac{2\pi}{N_y\Delta y}\,\beta, \quad \text{for } \beta = \frac{N_y}{2} - 1 \cdots -1, 0, 1, \ldots, \frac{N_y}{2}.$$

Then, the kinetic term can be calculated as

$$\begin{aligned} e^{-i\Delta t\hat{T}}\psi^n_{i,j} &= e^{-i\Delta t\hat{T}}\sum_{\alpha,\beta}\tilde{\psi}_{\alpha,\beta}\, e^{-\mathrm{i}(x_i k^{(x)}_\alpha + y_i k^{(y)}_\beta)} \\ &= \sum_{\alpha,\beta}\tilde{\psi}_{\alpha,\beta}\, e^{-i\Delta t\hat{T}} e^{-\mathrm{i}(x_i k^{(x)}_\alpha + y_i k^{(y)}_\beta)} \\ &= \sum_{\alpha,\beta}\tilde{\psi}_{\alpha,\beta}\, e^{-i\Delta t\frac{\left(k^{(x)}_\alpha\right)^2+\left(k^{(y)}_\beta\right)^2}{2}} e^{-\mathrm{i}(x_i k^{(x)}_\alpha + y_i k^{(y)}_\beta)}. \end{aligned}$$

We define the 4-tensor T with diagonal terms

$$T_{\alpha,\beta} = \frac{\left(k^{(x)}_\alpha\right)^2 + \left(k^{(y)}_\beta\right)^2}{2}.$$

Then, we can denote the time evolution under just the kinetic part as

$$e^{-i\Delta t\hat{T}}\psi^n_{i,j} = \mathcal{F}\left[e^{-\mathrm{i}\Delta t\, T}\mathcal{F}^{-1}\left[\psi^n\right]\right]_{i,j}.$$

Because the operators $\hat{T}$ and $\hat{V}$ do not commute, we cannot separate the full time evolution $e^{-i\Delta t(\hat{T}+\hat{V})}$ as $e^{-i\Delta t\,\hat{T}}e^{-i\Delta t\,\hat{V}}$. Instead, we can use the Baker-Campbell-Hausdorff formula [53]:

$$\begin{aligned} Z &= \log\left(e^{-i\Delta t\,\hat{T}}e^{-i\Delta t\,\hat{V}}\right) \\ &= -i\Delta t\,\hat{T} - i\Delta t\,\hat{V} + \frac{(-i\Delta t)^2}{2}[\hat{T},\hat{V}] + O(\Delta t^3)\cdots. \end{aligned} \tag{3.10}$$

where $[\hat{T},\hat{V}]$ represent commutator of the operators $\hat{T}$ and $\hat{V}$. We use a symmetric separation as $e^{-i\Delta t\,\hat{V}/2}e^{-i\Delta t\,\hat{T}}e^{-i\Delta t\,\hat{V}/2}$ because in that case we decrease the error of the approximation down to $O(\Delta t^3)$.

$$e^{-i\Delta t(\hat{T}+\hat{V})} \approx e^{-i\Delta t\,\hat{V}/2}e^{-i\Delta t\,\hat{T}}e^{-i\Delta t\,\hat{V}/2}. \tag{3.11}$$

Hence, we obtain the update formula for the Split-Step Fourier Method:

$$\psi^{n+1} = e^{-i\frac{\Delta t}{2}\,\hat{V}}\mathcal{F}\left[e^{-\mathrm{i}\Delta t\, T}\mathcal{F}^{-1}\left[e^{-i\frac{\Delta t}{2}\,\hat{V}}\psi^n\right]\right] \tag{3.12}$$

The method is highly efficient due to the use of the Fast Fourier Transform routines for switching between real and momentum space, and it is particularly well-suited for

periodic boundary conditions. Moreover, it provides excellent accuracy and numerical stability over long-time integrations, especially when the time step Δt is small and the wavefunction remains sufficiently smooth. In contrast to explicit finite-difference schemes, which approximate spatial derivatives with truncated series, the Split-Step Fourier Method represents derivatives spectrally via Fourier modes. This enables the method to achieve exponential convergence with respect to spatial resolution for sufficiently regular solutions, making it a particularly powerful tool for simulating nonlinear wave dynamics in Bose–Einstein condensates and related systems.

3.2 Exact Diagonalization

The Exact Diagonalization (ED) method is a numerically exact approach for studying quantum many-body systems of finite size. The fundamental idea is to represent the system's Hamiltonian as a matrix in a properly chosen many-body basis, most commonly the Fock basis, and then numerically diagonalize this matrix to obtain the full spectrum and eigenstates. Despite its computational limitations due to exponential scaling with system size, ED offers a non-perturbative and conceptually transparent way to analyze strongly correlated systems, especially when analytical methods are intractable.

In this thesis, we will investigate the bosonic quantum gas with contact interaction described in Sec. 2.1. The corresponding GP mean-field energy functional is obtained as in Eq. (2.19). However, we would like to solve the many-body problem exactly without depending on such an ansatz approximation. To achieve this, we obtain the second-quantized Hamiltonian of the corresponding many-body system

$$\hat{H} = \int \mathrm{d}^2 r_\perp \left[\hat{\Psi}^\dagger(\boldsymbol{r}_\perp) \left(-\frac{1}{2}\nabla_\perp^2 + V(\boldsymbol{r}_\perp) \right) \hat{\Psi}(\boldsymbol{r}_\perp) + \frac{g}{2} \hat{\Psi}^\dagger(\boldsymbol{r}_\perp) \hat{\Psi}^\dagger(\boldsymbol{r}_\perp) \hat{\Psi}(\boldsymbol{r}_\perp) \hat{\Psi}(\boldsymbol{r}_\perp) \right], \tag{3.13}$$

where $\hat{\Psi}(\boldsymbol{r}_\perp)$ and $\hat{\Psi}^\dagger(\boldsymbol{r}_\perp)$ are bosonic annihilation and creation operators with commutation $[\hat{\Psi}(\boldsymbol{r}_\perp), \hat{\Psi}^\dagger(\boldsymbol{r}'_\perp)] = \delta^{(2)}(\boldsymbol{r}_\perp - \boldsymbol{r}'_\perp)$ with $\delta^{(2)}$ is 2D Dirac delta function. We

expand the bosonic operators as [58]

$$\hat{\Psi}(\boldsymbol{r}_\perp) = \sum_\lambda \varphi_\lambda(\boldsymbol{r}_\perp)\hat{a}_\lambda, \tag{3.14}$$

$$\hat{\Psi}^\dagger(\boldsymbol{r}_\perp) = \sum_\lambda \varphi^*_\lambda(\boldsymbol{r}_\perp)\hat{a}^\dagger_\lambda, \tag{3.15}$$

where set $\{\varphi_\lambda(\boldsymbol{r}_\perp)\}$ defines a complete basis and $\hat{a}_\lambda$ and $\hat{a}^\dagger_\lambda$ are annhilitaion and creation operators for bosons in the defined state λ with commutaion relation $[\hat{a}_\lambda, \hat{a}^\dagger_{\lambda'}] = \delta_{\lambda,\lambda'}$. The two-body interaction elements are calculated as

$$\langle\lambda|\hat{H}|\lambda'\rangle = \int \mathrm{d}^2 r_\perp \left[\varphi^*_\lambda(\boldsymbol{r}_\perp)\left(-\frac{1}{2}\nabla^2_\perp + V(\boldsymbol{r}_\perp)\right)\varphi_{\lambda'}(\boldsymbol{r}_\perp)\right].$$

Similary the four-point interaction elements of the Hamiltonian are calculated as

$$\langle\lambda_1\lambda_2|\hat{H}|\lambda'_1\lambda'_2\rangle = \int \mathrm{d}^2 r_\perp \left[\frac{g}{2}\varphi^*_{\lambda_1}(\boldsymbol{r}_\perp)\varphi^*_{\lambda_2}(\boldsymbol{r}_\perp)\varphi_{\lambda'_2}(\boldsymbol{r}_\perp)\varphi_{\lambda'_1}(\boldsymbol{r}_\perp)\right].$$

We will show the explicit form of these terms in Chapter 5 using LLL basis in the Landau gauge as introduced in Sec.2.2.1.1.

Unfortunately, for N many bosons in N_s many basis states, the number of available states

$$\binom{N + N_s - 1}{N}$$

becomes very large with increasing N or N_s. Therefore, to study realistic physical systems, we need to use approximation methods instead of constructing the whole basis and solving with diagonalization methods.

3.3 Density Matrix Renormalization Group

The DMRG[59, 60] is considered one of the most powerful numerical tools to investigate strongly correlated quantum systems in 1D [61, 62]. It is a variational method to find a many-body ground state for a given Hamiltonian $\hat{H}$. In other words, it searches for a many-body state

$$|\psi\rangle = \sum_{n_1 n_2 \cdots n_L} \psi_{n_1,n_2,\cdots,n_L} |n_1, n_2, \cdots, n_L\rangle \tag{3.16}$$

that gives the minimum energy $E = \langle\psi| \hat{H} |\psi\rangle$, where $\psi_{n_1,n_2,\cdots,n_L}$ is a complex coefficient of the corresponding many-particle state in the 1D lattice with L many sites. Thus, the many-body problem of finding the ground state transforms to finding the coefficients $\psi_{n_1,n_2,\cdots,n_L}$ such that the corresponding many-body state minimizes the energy E. In the following subsections, we will review how DMRG handles the variational routine, and what method can be used to represent the coefficients $\psi_{n_1,n_2,\cdots,n_L}$ for lower computing costs.

3.3.1 Reduced Density Matrix and Truncation in DMRG Algorithms

The main principle of DMRG algorithms is to divide the quantum chain into two subchains. Let us divide the chain introduced in Eq. (3.16) at the site a as

$$|\psi\rangle = \sum_{n_1 n_2 \ldots n_a} \sum_{n_{a+1} \ldots n_L} \psi_{n_1,n_2,\ldots,n_L} |n_1, n_2, \cdots, n_a\rangle \otimes |n_{a+1}, \cdots, n_L\rangle . \tag{3.17}$$

We refer to the state at the left side of the tensor product as $|l\rangle$ and the one at the right side as $|r\rangle$. We denote the corresponding Hilbert spaces as $\mathcal{H}_L$ and $\mathcal{H}_R$ with dimensions $N_l = d\ a$ and $N_r = d(L-a)$, respectively , where d is the maximum occupation number at a given site in the chain. Thus, we can effectively define the same state with a $N_l \times N_r$ matrix with indices $\psi_{l,r}$ as

$$|\psi\rangle = \sum_{l=1}^{N_l} \sum_{r=1}^{N_r} \psi_{l,r} |l\rangle \otimes |r\rangle , \tag{3.18}$$

where the coefficients are exactly equal to the corresponding ones in the first equation (3.16).

Because dealing with large matrices causes computational problems, one understandably may want to approximate the many-body state $|\psi\rangle$ rather than storing it exactly for larger values of d or L. In that case, the actual dimensions N_l and N_r are truncated to lower values $\tilde{N}_l$ and $\tilde{N}_r$, respectively. We have to make sure to use the most important bipartite states $|l\rangle$ and $|r\rangle$ with largest probabilities by minimizing the 2-norm distance $\left||\psi\rangle - |\tilde{\psi}\rangle\right|^2$ between the current ground state $|\psi\rangle$ and its truncated version $|\tilde{\psi}\rangle$. The corresponding truncation method involves selecting the eigenstates of the density matrix with the largest eigenvalues w_a. Then, one can define the truncation

error [61, 62]

$$\epsilon = 1 - \sum_{a=1}^{\tilde{N}} w_a, \tag{3.19}$$

where $\tilde{N}$ is the reduced dimension for a general density matrix. In the bipartite problem discussed above, we reduced the dimensions of one of the bipartite states, so we work with the reduced density matrix of the corresponding part, which is obtained by taking the trace of the other part of the chain:

$$\hat{\rho}_L = \mathrm{Tr_R}(\hat{\rho}) = \sum_{l,r,l'} \psi_{l,r} \Big(|l\rangle \otimes |r\rangle \Big) \Big(\langle l'| \otimes \langle r| \Big) \psi^*_{l',r}, \tag{3.20a}$$

$$\hat{\rho}_R = \mathrm{Tr_L}(\hat{\rho}) = \sum_{l,r,r'} \psi_{l,r} \Big(|l\rangle \otimes |r\rangle \Big) \Big(\langle l| \otimes \langle r'| \Big) \psi^*_{l,r'}. \tag{3.20b}$$

Hence, the truncation of each subchain is done by choosing the first $\tilde{N}_l$ and $\tilde{N}_r$ eigenstates of the matrices ρ_L and ρ_R with coefficients

$$(\rho_L)_{l,l'} = \sum_r \psi_{l,r} \psi^*_{l',r} \quad \text{and} \quad (\rho_R)_{r,r'} = \sum_l \psi_{l,r} \psi^*_{l,r'},$$

respectively. Thus, the truncated version of the many-body ground state $|\tilde{\psi}\rangle$ serves as a good approximation unless the truncation error ϵ increases large enough with the chain size L. Luckily, in an D-dimensional bipartite quantum system with short-range interaction, the ground state with an energy gap has von Neumann entropy in the order of the area of the intersection region between $(D-1)$-dimensional subparts L^{D-1}. This behaviour of the entropy is called area-law[63, 64, 65, 66] and the von Neumann entropy is defined as

$$S_{\mathrm{vN}} = -\mathrm{Tr}\Big(\rho_L \log_2(\rho_L)\Big) = -\mathrm{Tr}\Big(\rho_R \log_2(\rho_R)\Big). \tag{3.21}$$

Thus, in a 1D quantum system with relevant conditions, we expect the von Neumman entropy calculated with summation of the eigenvalues of reduced density matrices w_a to be of the order of $L^{D-1} = L^{1-1} = 1$, so it does not increase rapidly with the size of the chain. In this way, one can increase the chain length L considerably beyond what is feasible with other numerical methods and reliably use the truncation trick for constant values of $\tilde{N}_r$ and $\tilde{N}_l$, thanks to the area-law behaviour of the ground state of a 1D quantum system.



(a) (b)

Figure 3.1: In the MPS method, the coefficients $\psi_{n_1 n_2 \cdots n_N}$ of Fock states, which are in the form of an Nth order tensor (a), are obtained by multiplying N-many matrices (b).

3.3.2 DMRG with Matrix Product States

In this project, we are using the ITensor package[67] to perform DMRG routines. It uses the Matrix Product State (MPS) method to represent the coefficients $\psi_{n_1,n_2,\ldots,n_L}$, which is an L-dimensional tensor, with a multiplication of matrices as

$$|\psi\rangle = \sum_{n_1 n_2 \cdots n_N} A^{n_1} A^{n_2} \cdots A^{n_N} \, |n_1, n_2, \cdots, n_N\rangle \,, \tag{3.22}$$

which is illustrated in Fig.3.1

The MPS method uses a Singular Value Decomposition method to tear the L-tensor ψ into a multiplication of matrices (2-tensors) as illustrated in Fig.3.1. Each matrix has at most $\chi \times \chi$ size, where χ is referred to as the truncation dimension. During the DMRG calculations, only one or two neighbor matrices are used in the variation routine. The matrices are varied such that they diagonalize the matrix elements $\langle\lambda|\hat{H}|\lambda\rangle$ that affect them. The first χ-many eigenvalues are chosen to construct the new version of matrices, similarly to what we discussed in the DMRG routine in the previous section. The site number of the target matrices is swept back and forth on the quantum chain until the MPS converges on a state, which is approximated as the ground state of the many-body chain.

CHAPTER 4

SNAKE INSTABILITY IN BOSE-EINSTEIN CONDENSATE IN ANISOTROPIC TRAPS

The stability of soliton solutions highly depends on the dimensionality of the system. When the dimension is higher than one, solitons tend to become unstable, leading to what is known as the snake instability. The term is coined due to the bending behavior of the soliton during the decay process[68, 6, 69]. This phenomenon is thoroughly investigated through the existence of imaginary oscillation energies with the Bogoliubov-de Gennes (BdG) formalism[10, 70, 11]. Their instability is first observed experimentally in nonlinear optics[71, 72]. Shortly after, solitonic structures in atomic BECs are realized[73, 74], and their decay process into vortex rings is well-documented in 3D condensates[75, 76]. However, it is possible to obtain solitonic vortex structures as decay products instead of vortex rings under certain conditions, such as when the anisotropy of the confinement of the condensate is large enough, as predicted theoretically [77, 8, 9] and observed experimentally [78]. It is important to note that when the confinement is extended even further to establish a quasi-1D configuration, dynamical instabilities are suppressed, and solitons become stable excitations. [8, 9, 13]. Even the particle-like oscillation and collisions between multiple solitons are theoretically and experimentally observed in this regime [79, 80, 81, 82]. In addition to squeezing the condensate, stable solitons are formed under the influence of some exotic traps[83], and dipolar condensates[84].

Although there have been extensive studies on the stability of solitons in the literature, there is a lack of analytical investigations on snake instability apart from the BdG analysis. In our study, we suggest a variational wavefunction to study the stability of solitons. Our aim is to represent both soliton and aligned vortex-antivortex configura-

tions within the same variational wavefunction. We use the GP equation to represent the BECs and study the corresponding field Lagrangian for our variational function. We find that the soliton instability can be suppressed by tuning system parameters, such as the anisotropy of the harmonic potential, consistent with earlier results in the literature [8, 9, 13].

The chapter is organized as follows: In Section 4.1, we use both a variational wavefunction and direct simulation of the full 2D GP equation to obtain the excitation energies of dark solitons and vortices and their relation with respect to the change in the anisotropy of the trap potential. In Section 4.2, we discuss how we perform a real-time simulation of dark solitons and present the snake instability. We show that a strong anisotropy results in a stabilization of the dark soliton. In Section 4.3, we introduce our variational wavefunction and examine the excitation states it represents with two variational parameters. Then, in Section 4.4, we study the stability of dark soliton excitation in three scenarios: (i) constant density, (ii) Thomas-Fermi profile, and (iii) Gaussian density. We use the Euler-Lagrange equations for the parameters to search for any imaginary oscillation frequencies depending on the physical parameters in the Hamiltonian. We assume that any instability of the parameters in our wavefunction corresponds to the snake instability in the arising structure. In the Sec. 4.5, we compare our findings with numerical calculations, and finally, in the Sec. 4.6, we conclude the chapter by discussing our results.

4.1 Excitation Energies of Solitons and Vortices in Anisotropic Trap

To understand the instability of the dark soliton, we first investigate the energies of both soliton and single-vortex excitations. First, we use variational wavefunctions φ_{s} and φ_{v} defined as

$$\varphi_{\mathrm{s}}(\boldsymbol{r}_\perp, \xi_s) = \psi_0(\boldsymbol{r}_\perp) \tanh\left(\frac{x}{\xi_{\mathrm{s}}}\right), \tag{4.1a}$$

$$\varphi_{\mathrm{v}}(\boldsymbol{r}_\perp, \xi_v) = \psi_0(\boldsymbol{r}_\perp) e^{\mathrm{i}\phi} \frac{r_\perp/\xi_{\mathrm{v}}}{\sqrt{2 + r_\perp^2/\xi_{\mathrm{v}}^2}} \tag{4.1b}$$

to represent soliton and vortex excitation of the Bose gas, respectively [1]. Here, ψ_0 denotes the ground state condensate wavefunction. The parameters (r, ϕ) are the polar

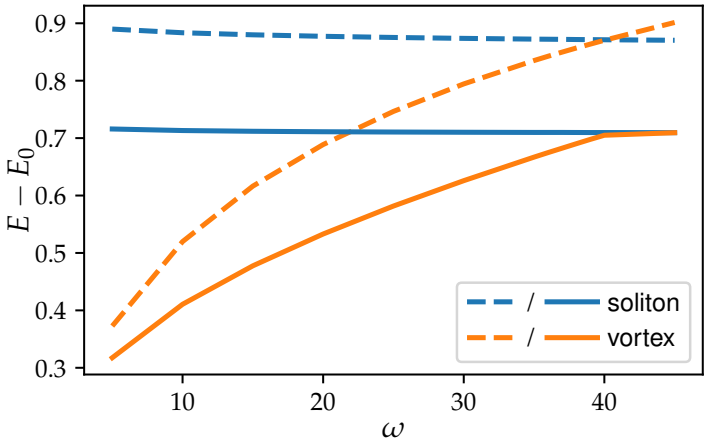

Figure 4.1: Comparison of mean excitation energies of soliton (blue) and vortex (orange) states for $N = 500$ and $g = 1$. Dashed lines refer to the variational states defined in Eqs. (4.1), whereas the solid lines show the energies of numerically obtained excitations.

coordinates. The healing lengths ξ_s and ξ_v can be treated as variational parameters to minimize the expectation values $\langle \hat{H}_{GP} \rangle$, which can be approximated to the energy of the state E. Then, the excitation energy can be calculated as the energy difference $E_{ex} = E - E_0 = \langle \hat{H}_{GP} \rangle - E_0$, where E_0 is the ground state energy of the condensate state ψ_0.

We obtain the the ground state ψ_0 by solving GP equation numerically for various anisotropy ratios ω by keeping the particle number N and the interaction strength g constant. We compare the excitation energies of both solutions and observe that an increase in the anisotropy ratio ω enables dark solitons being energetically favorable than a single vortex, as illustrated in Fig. 4.1.

We also obtain these excitations by solving Eq. (2.21) numerically under the influence of specific symmetry constraints. For example, to obtain a dark soliton solution ψ_s, we restrict our condensate function to have an odd symmetry in the x-direction throughout the numerical simulation, i.e., $\psi_s(x, y) = -\psi_s(-x, y)$. The imaginary time evolution of a function under such a symmetry results in a dark soliton solution. To obtain a vortex solution ψ_v, featuring a single vortex at the core of the condensate, we first introduce a single flux, $e^{i\phi}$, to the center of our initial constant function, ψ_i. In addition to the initial flux, we apply odd-parity symmetry constraint during the time

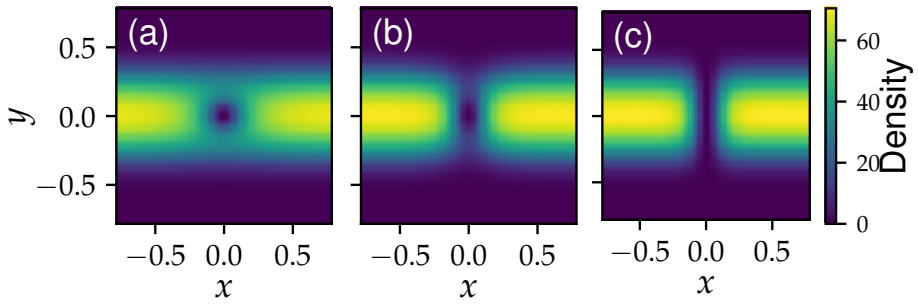

Figure 4.2: Comparison of densities of a single-vortex (a), a solitonic vortex (b), and a soliton (c) excitations obtained for $\omega = 30$, $Ng = 500$. The single vortex is obtained with a variation function $\varphi_{\rm v}$, where the solitonic vortex and the dark soliton are obtained with imaginary time evolution with corresponding symmetry constraints mentioned in the text.

evolution, i.e. $\psi_{\rm v}(\boldsymbol{r}) = e^{\pm {\rm i}\pi}\psi_{\rm v}(-\boldsymbol{r}) = -\psi_{\rm v}(-\boldsymbol{r})$. This symmetry constraint keeps the flux center fixed at the core of the function and facilitates rapid convergence to a single-vortex state. When the energies of these numerically obtained solutions $\psi_{\rm s}$ and $\psi_{\rm v}$ are measured, it is seen that these are slightly more favorable in comparison with their variational counterparts defined in Eqs. (4.1), as seen in Fig. 4.1. This outcome is expected since these solutions are obtained by numerically solving the differential equation rather than relying on an ansatz wavefunction form.

We note two crucial results that can be observed from Fig. 4.1: The first one is that the odd-parity constraint cannot yield a single-vortex excitation for large anisotropy ratios. Instead, the simulation converges to a dark soliton solution with odd symmetry only along the x-axis. The reason is that the imaginary time evolution seeks a state with minimum energy under the applied symmetry constraint, and for large anisotropies, dark solitons become the state with the lowest energy satisfying the parity symmetry requirement. Thus, we obtain the overlap between the energies in large anisotropies in Fig. 4.1. The second result that we would like to emphasize is that while the numerically obtained single-vortex state has a similar energy to the variational function for low anisotropies, the energy difference opens rapidly. It is because we obtain a solitonic vortex rather than a circularly symmetric single vortex for the intermediate values of anisotropy ω [77, 8]. We present the density profiles of the mentioned states in Fig.4.2. Both the energy and density profiles of solitonic

vortices signal that a solitonic vortex is a linear combination of a single vortex and soliton states. This observation was our main motivation for our ansatz wavefunction, described in detail in the following section.

4.2 Numerical Observation of Snake Instability

To obtain a stationary soliton configuration within the trapped condensate, we initialize the wavefunction with a nodal line along the $x = 0$ axis and enforce odd parity under reflection $x \to -x$. This symmetry condition ensures the presence of a dark soliton centered at $x = 0$, as the density must vanish along this plane. We then evolve the GP equation in imaginary time. This relaxes the system to a metastable state consistent with the imposed symmetry. The resulting wavefunction corresponds to a dark soliton embedded within the anisotropic ground-state density profile of the condensate.

To assess the stability of the soliton, we evolve the system in real time starting from the stationary soliton configuration. The presence of small perturbations—whether from numerical noise or residual excitation—provides a natural seed for instability. If the soliton is unstable, we observe the nodal plane bending over time and eventually breaking into more complex structures such as vortices. In contrast, a stable soliton maintains its profile with negligible deformation for extended durations. We find that simulating the dynamics over a time window corresponding to four to six trap periods in the x-direction ($t \sim 4\pi$ to 6π) is sufficient to determine stability. Figure 4.3 illustrates this behavior: the left panel shows the soliton bending and decaying into vortex structures for a weakly anisotropic trap ($\omega = 3$), while the right panel displays a long-lived, stable soliton for a strongly anisotropic trap ($\omega = 35$). Note that the vertical (y) axis is scaled differently in the two panels to account for the varying trap anisotropy.

The snake instability manifests itself through two intertwined mechanisms: the transverse bending of the soliton plane and the subsequent fragmentation of the nodal line into point-like topological defects. The soliton, initially characterized by a planar density node and a localized phase jump, becomes dynamically unstable when trans-

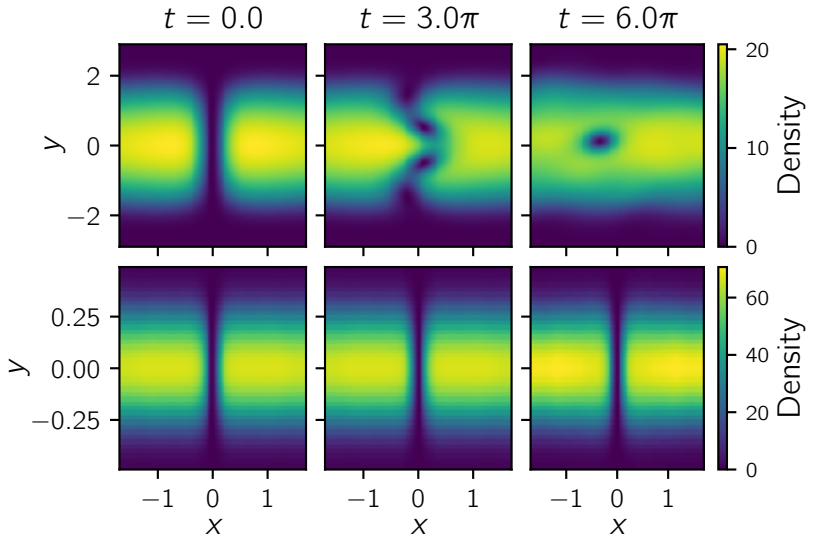

Figure 4.3: Time evolution of a dark soliton in a trapped BEC for two different trap anisotropies, both with $g = 1$ and $N = 400$. The colorbars show the density of BECs. Top row: For $\omega = 3$, the soliton is dynamically unstable and decays via the snake instability, leading to the formation of vortex structures. Bottom row: For $\omega = 35$, the soliton remains stable and persists without significant deformation. Note that the vertical axis (y) is scaled differently in the two panels to reflect the change in trap geometry.

verse modulations are energetically favorable. As the soliton bends, regions of higher curvature incur a kinetic energy cost due to increased phase gradients. In a condensate that is sufficiently narrow along the transverse direction, there is simply not enough spatial extent for such bending to occur without excessive energy penalty, leading to dynamical stabilization of the soliton.

However, the bending of the nodal plane is not the sole feature of the instability. The nodal line itself is susceptible to fragment into a sequence of point nodes, each accompanied by localized phase winding. These point defects correspond to vortex-antivortex pairs aligned along the former soliton plane. Viewed from a distance, the alternating vortices collectively maintain the overall phase structure imposed by the original soliton, including the characteristic π phase shift across the nodal region. The vortex cores may appear anisotropic due to the geometry of the trap and the inhomogeneity of the condensate. Our numerical simulations reveal both bending

and vortex formation, in agreement with experimental observations of dark soliton decay in trapped BECs [76].

4.3 Variational Wavefunction

We want to study analytically the dynamical process during the transition of a dark soliton to vortices. To achieve this goal, we try to write a variational function that captures both a dark soliton and aligned vortices on a single footing. We write the function

$$\psi(x,y) = \sqrt{n(x,y)}\bigg(\tanh(x/\xi_s) + \mathrm{i}\alpha\,\mathrm{sech}(x/\xi_s)\sin(ky)\bigg), \tag{4.2}$$

where $n(x,y)$ is the density profile of the condensate state far away from the soliton section, ξ_s is the healing length of the soliton, k is a constant that determines the location of vortices, and α is our variational parameter. By adjusting the parameter α from 0 to 1, one can see that the wavefunction evolves from a dark soliton to an aligned vortex-antivortex configuration. The top panel of Fig. 4.4 presents the density profile of our variational function for different values of α. When $\alpha = 0$, the second term in the function vanishes, leaving us with a dark soliton. On the other hand, for $\alpha = 1$, the function yields an aligned vortex-antivortex structure at the center. For intermediate values of α, our variational wavefunction can represent an aligned solitonic vortex-antivortex configuration as well. The vortices produced by our wavefunction are positioned where the sine function equals zero. Therefore, the distance between a neighbor vortex and antivortex becomes π/k.

During the decay caused by snake instability in BECs, the zero section of the dark soliton bends as a snake-like shape. This bending results in vortex–antivortex pairs forming approximately at the nodal points of the "snake". To describe this, we modify the hyperbolic functions in equation (4.2) to include spatial bending by letting $\frac{x}{\xi_s} \to \frac{x}{\xi_s} - \beta\sin(ky)$, where β is the amplitude of the bending. In this work, we investigate instability of soliton states, so our primary focus is the limit $\beta \to 0$. This limit transforms our wavefunction into

$$\psi(x,y) \approx \sqrt{n(x,y)}\bigg(\tanh\left(\frac{x}{\xi_s}\right) + \mathrm{i}(\alpha+\mathrm{i}\beta)\,\mathrm{sech}\left(\frac{x}{\xi_s}\right)\sin(ky)\bigg). \tag{4.3}$$

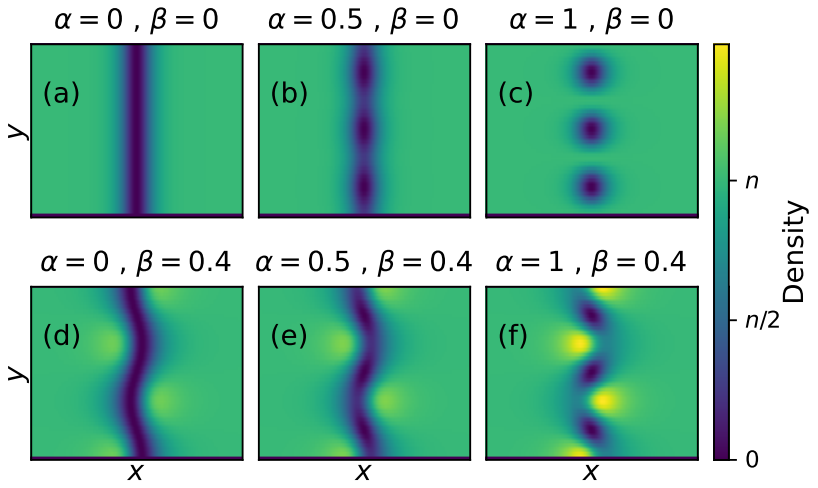

Figure 4.4: Density profile of the variational wavefunction defined in Eq. 4.3 in a condensate with constant density n. We choose the parameter $\alpha = 0.0$ (a & d), 0.5 (b & e), and 1.0 (c & f). We choose $\beta = 0$ in the top figures (a, b & c) and $\beta = 0.4$ for the remaining (d, e & f).

In the bottom panel of Fig.4.4, we also give the density profiles with non-zero imaginary part of the parameter $\beta = 0.4$.

4.4 Stability Analysis of Dark Soliton

We search for any instability in our function (4.3) around the position $(\alpha, \beta) = (0, 0)$ in the parameter space since this position represents a dark soliton without any snake-like deformation and assume that the existence of imaginary oscillation frequencies indicates that the corresponding dark soliton is unstable and will undergo snake instability. We derive the differential equations for parameters α and β using the field Lagrangian $L = T - U$, where T and U represent the kinetic and potential functionals, respectively. They are defined as

$$T = \frac{\mathrm{i}}{2} \int \psi^* \dot{\psi} - \psi \dot{\psi}^* \mathrm{d}^2 r, \tag{4.4a}$$

$$U = \int \left(\frac{|\nabla \psi|^2}{2} + V(\boldsymbol{r})|\psi|^2 + \frac{g|\psi|^4}{2} - \mu|\psi|^2 \right) \mathrm{d}^2 r \tag{4.4b}$$

in the dimensionless form. We note that the Euler-Lagrange equation for ψ^* results in the GP equation. We investigate our system in a particle bath with a constant chemical

potential μ to adjust the condensate density at points far from the dark soliton. For analytical convenience, we consider the length of the system in the x direction to be much larger than the soliton healing length ξ_s, allowing us to treat it as infinitely long in the x direction. We denote the integrations of each term in Eq. (4.4b) as U_t, U_v, U_g, and U_μ, respectively. We note that the resulting Lagrangian may include terms not depending on the variational parameters α and β. Since those terms does not have any influence on the resulting equations, we will omit those terms in the rest of this work.

4.4.1 Condensate with Constant Density

First, we consider the simplest approximation: a uniform background density $n(x, y) = n$ in the absence of an external potential, i.e., $V(\boldsymbol{r}) = 0$. This choice enables us to perform straightforward calculations of the spatial integrals in Lagrangian (4.4) and analytically traceable dynamics for the snake instability. Since we consider an infinite condensate along the y-direction, the spatial integrals introduced in Eqs.(4.4) will be divergent. Using the periodicity along the y-direction, we only perform integration in the domain $D = \{(x, y) \mid x \in \mathbb{R}, -\frac{h}{2} < y < \frac{h}{2}\}$, where the squeezing length h is chosen such that the domain D contains N_v many vortces:

$$h = \frac{N_\mathrm{v}\pi}{k}. \tag{4.5}$$

The first term in the kinetic functional T becomes

$$\begin{aligned}\psi^*\dot{\psi} = n\Big[&\tanh(x/\xi_s)\mathrm{i}(\dot{\alpha} + \mathrm{i}\dot{\beta})\mathrm{sech}(x/\xi_s)\sin(ky) \\ &+ (\alpha - \mathrm{i}\beta)(\dot{\alpha} + \mathrm{i}\dot{\beta})\mathrm{sech}^2(x/\xi_s)\sin^2(ky)\Big].\end{aligned} \tag{4.6}$$

Therefore,

$$T = \frac{\mathrm{i}}{2}\int \psi^*\dot{\psi} - \psi\dot{\psi}^*\mathrm{d}^2r = -\int \Im\{\psi^*\dot{\psi}\}\mathrm{d}^2r$$

$$\implies T = -n\int_{-\infty}^{\infty}\mathrm{d}x\int_{-h/2}^{h/2}\mathrm{d}y\left[\underbrace{\dot{\alpha}\tanh(x/\xi_s)\mathrm{sech}(x/\xi_s)}_{\text{odd symmetry in x-dir.}}\sin(ky)\right. \tag{4.7}$$

$$\left. -(\beta\dot{\alpha}-\alpha\dot{\beta})\mathrm{sech}^2(x/\xi_s)\sin^2(ky)\right] \tag{4.8}$$

$$\implies T = n2\xi_s\frac{h}{2}(\beta\dot{\alpha}-\alpha\dot{\beta}) = n\xi_s h(\beta\dot{\alpha}-\alpha\dot{\beta}). \tag{4.9}$$

To calculate the kinetic energy term U_t, we need to obtain

$$\nabla\psi = \hat{i}\frac{1}{\xi_s}\sqrt{n}\Big[\mathrm{sech}^2(x/\xi_s) - \mathrm{i}(\alpha+\mathrm{i}\beta)\tanh(x/\xi_s)\mathrm{sech}(x/\xi_s)\sin(ky)\Big] + \hat{j}\sqrt{n}\mathrm{i}(\alpha+\mathrm{i}\beta)\mathrm{sech}(x/\xi_s)k\cos(ky) \tag{4.10}$$

$$\implies |\nabla\psi|^2 = \frac{1}{\xi_s^2}n\Big[\mathrm{sech}^4(x/\xi_s) + 2\beta\mathrm{sech}^3(x/\xi_s)\tanh(x/\xi_s)\sin(ky) + (\alpha^2+\beta^2)\mathrm{sech}^2(x/\xi_s)\tanh^2(x/\xi_s)\sin^2(ky)\Big] + n(\alpha^2+\beta^2)\mathrm{sech}^2(x/\xi_s)k^2\cos^2(ky) \tag{4.11}$$

Hence, by omitting the first term that does not depend on the variational parameters, we obtain

$$\implies U_t = \int \mathrm{d}^2r\frac{1}{2}|\nabla\psi|^2 \tag{4.12}$$

$$= \frac{1}{2}n\int_{-\infty}^{\infty}\mathrm{d}x\int_{-h/2}^{h/2}\mathrm{d}y\left[\frac{2\beta}{\xi_s^2}\underbrace{\mathrm{sech}^3(x/\xi_s)\tanh(x/\xi_s)}_{\text{odd symmetry in x-dir.}}\sin(ky)\right.$$

$$+\frac{1}{\xi_s^2}(\alpha^2+\beta^2)\mathrm{sech}^2(x/\xi_s)\tanh^2(x/\xi_s)\sin^2(ky) \tag{4.13}$$

$$\left.+k^2(\alpha^2+\beta^2)\mathrm{sech}^2(x/\xi_s)k^2\cos^2(ky)\right]$$

$$\implies U_t = \frac{n}{2}(\alpha^2+\beta^2)\left[\frac{1}{\xi_s^2}\frac{2\xi_s}{3}\frac{h}{2} + 2\xi_s k^2\frac{h}{2}\right]$$

$$= n\xi_s h(\alpha^2+\beta^2)\left(\frac{1}{6\xi_s^2}+\frac{k^2}{2}\right) \tag{4.14}$$

The density of the variational function becomes

$$|\psi|^2 = n\Big[\tanh^2(x/\xi_s) + (\alpha^2+\beta^2)\text{sech}^2(x/\xi_s)\sin^2(ky) \\ -2\beta\tanh(x/\xi_s)\text{sech}(x/\xi_s)\sin(ky)\Big]. \tag{4.15}$$

Hence, we can calulate the chemical potential term U_μ as

$$\begin{aligned}
\implies U_\mu &= -\mu\int \mathrm{d}^2r\ |\psi|^2 \\
&= -\mu n\int_{-\infty}^{\infty}\mathrm{d}x\int_{-h/2}^{h/2}\mathrm{d}y\ \Big[(\alpha^2+\beta^2)\text{sech}^2(x/\xi_s)\sin^2(ky) \\
&\qquad -2\beta\underbrace{\tanh(x/\xi_s)\text{sech}(x/\xi_s)}_{\text{odd symmetry in x-dir.}}\sin(ky)\Big] \qquad (4.16)\\
\implies U_\mu &= -\mu n\xi_s h(\alpha^2+\beta^2). \qquad (4.17)
\end{aligned}$$

To calculate the non-linear interaction term U_g, we firstly obtain

$$|\psi|^4 = n^2\Big[\tanh^4(x/\xi_s) + (\alpha^2+\beta^2)^2\text{sech}^4(x/\xi_s)\sin^4(ky) \\ +4\beta^2\tanh^2(x/\xi_s)\text{sech}^2(x/\xi_s)\sin^2(ky) \\ +2(\alpha^2+\beta^2)\tanh^2(x/\xi_s)\text{sech}^2(x/\xi_s)\sin^2(ky) \\ -4\beta\tanh^3(x/\xi_s)\text{sech}(x/\xi_s)\sin(ky) \\ -4(\alpha^2+\beta^2)\beta\tanh(x/\xi_s)\text{sech}^3(x/\xi_s)\sin^3(ky)\Big] \tag{4.18}$$

Therefore, we calculate the interaction term U_g as

$$\implies U_g = \frac{g}{2}\int \mathrm{d}^2 r\ |\psi|^4 \tag{4.19}$$

$$= \frac{g}{2}n^2 \int_{-\infty}^{\infty} \mathrm{d}x \int_{-h/2}^{h/2} \mathrm{d}y \Bigg[(\alpha^2+\beta^2)^2 \mathrm{sech}^4(x/\xi_s)\sin^4(ky)$$

$$+ 4\beta^2 \tanh^2(x/\xi_s)\mathrm{sech}^2(x/\xi_s)\sin^2(ky)$$

$$+ 2(\alpha^2+\beta^2)\tanh^2(x/\xi_s)\mathrm{sech}^2(x/\xi_s)\sin^2(ky) \tag{4.20}$$

$$- 4\beta \underbrace{\tanh^3(x/\xi_s)\mathrm{sech}(x/\xi_s)}_{\text{odd symmetry in x-dir.}} \sin(ky) \to 0$$

$$- 4(\alpha^2+\beta^2)\beta \underbrace{\tanh(x/\xi_s)\mathrm{sech}^3(x/\xi_s)}_{\text{odd symmetry in x-dir.}} \sin^3(ky) \to 0 \Bigg]$$

$$\implies U_g = \frac{g}{2}n^2\left[(\alpha^2+\beta^2)^2\frac{4\xi_s}{3}\frac{3h}{8} + 2(\alpha^2+3\beta^2)\frac{2\xi_s}{3}\frac{h}{2}\right]$$

$$\implies U_g = gn^2\xi_s h\frac{1}{3}(\alpha^2+3\beta^2) + gn^2\xi_s h\frac{1}{4}(\alpha^2+\beta^2)^2. \tag{4.21}$$

Hence, we obtain all the terms in the Lagrangian L. After scaling every term with $(n\xi_s h)^{-1}$, our resulting Lagrangian becomes as

$$\begin{aligned} L = T - U = (\beta\dot{\alpha} - \alpha\dot{\beta}) - (\alpha^2+\beta^2)\left(\frac{1}{6\xi_s^2} + \frac{k^2}{2} - \mu\right) \\ -\frac{gn}{3}(\alpha^2+3\beta^2) - \frac{gn}{4}(\alpha^2+\beta^2)^2. \end{aligned} \tag{4.22}$$

The resulting Euler-Lagrange equations for variational paramaters α and β are

$$\dot{\alpha} = \left[\frac{1}{6\xi_s^2} + \frac{k^2}{2} - \mu + gn\right]\beta + \frac{gn}{2}\beta(\alpha^2+\beta^2), \tag{4.23a}$$

$$\dot{\beta} = -\left[\frac{1}{6\xi_s^2} + \frac{k^2}{2} - \mu + \frac{gn}{3}\right]\alpha - \frac{gn}{2}\alpha(\alpha^2+\beta^2). \tag{4.23b}$$

We can use the standard expressions of the soliton healing length ξ_s and the background density n in terms of the chemical potential μ and the interaction strength g:

$$\xi_s = \sqrt{2}\xi = \frac{1}{\sqrt{\mu}}, \tag{4.24a}$$

$$n = \frac{\mu}{g}, \tag{4.24b}$$

After applying the identities between ξ_s, μ,n, we obtain the differential equations below:

$$\dot{\alpha} = \left[\frac{\mu}{6} + \frac{k^2}{2}\right]\beta + \frac{\mu}{2}(\alpha^2 + \beta^2)\beta, \tag{4.25a}$$

$$\dot{\beta} = -\left[\frac{k^2}{2} - \frac{\mu}{2}\right]\alpha - \frac{\mu}{2}(\alpha^2 + \beta^2)\alpha. \tag{4.25b}$$

As in Fig.4.5, we can observe two distinct regimes. For large values of k, the origin $(\alpha, \beta) = (0, 0)$ is the only fixed point, and all nearby trajectories form closed orbits around it. This behavior indicates stable, bounded oscillations of the variational parameters (α, β), which correspond to a soliton that resists vortex formation and bending. In this regime, the soliton is dynamically stable against snake instability.

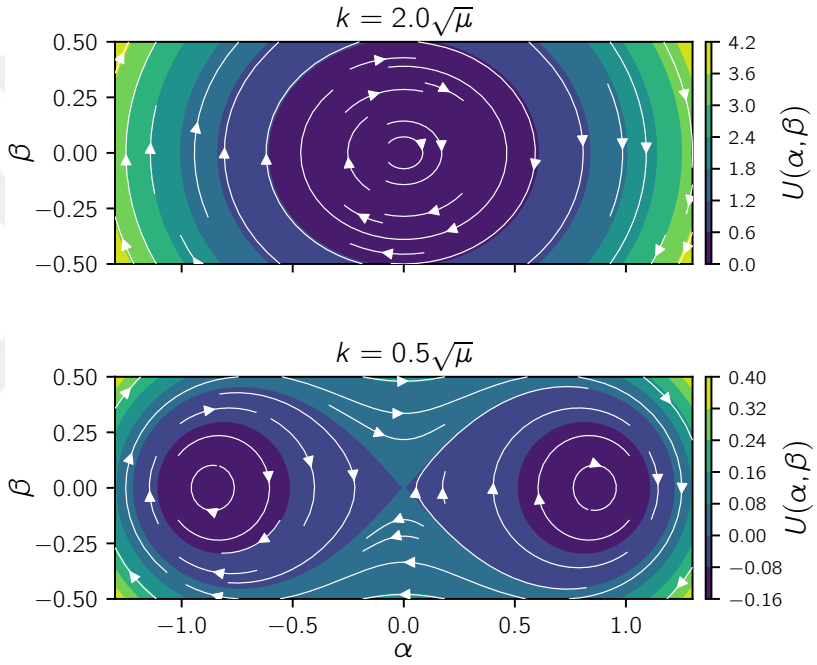

Figure 4.5: Phase space of the variational dynamical system defined by Eqs.(4.25) in the complex $A = \alpha + \mathrm{i}\beta$ plane, illustrating the dependence of the flow topology on the perturbation wavenumber k. The colorbars indicate the potential energy $U(\alpha, \beta)$ calculated with Eq.(4.4b), and the arrows show the direction of the flow in the phase space. For large $k = 2.0\sqrt{\mu}$,(top), the origin is a stable center, and all nearby trajectories form closed orbits, indicating dynamically stable soliton configurations. For small $k = 0.5\sqrt{\mu}$(bottom), the origin becomes a saddle point and two stable fixed points appear along the $\beta = 0$ axis, signaling a stable vortex-antivortex array.

Since we examine the stability around $(\alpha, \beta) = (0, 0)$, we can linearize the non-

linear coupled equations around the origin of the parameter space. The obtained eigenfrequency Ω of the oscillation around the dark soliton satisfies the following equation:

$$\Omega^2 = \left(\frac{\mu}{6} + \frac{k^2}{2}\right)\left(\frac{k^2}{2} - \frac{\mu}{2}\right). \tag{4.26}$$

Therefore, our method suggests the suppression of snake instability with long-wavelength perturbations with $k^2 > \mu$. This also leads to the unstable modes having the relation $0 < k\xi_s < 1$, which coincides with Ref.[85]

Now, we use the analytical results derived from the linearized dynamics to estimate the critical trap anisotropy required for stabilizing the dark soliton using the physical intuition in Ref.[13]. The key assumption is that unstable transverse modes can only be excited if their wavelength fits within the transverse extent of the condensate. In particular, we assume that modes with wavelengths larger than the size of the condensate along the y-direction are suppressed. We estimate the stabilization threshold by requiring that the smallest wavelength unstable mode λ_c no longer fits within the condensate. In the TF limit, the transverse extent of the condensate is given by $2R_y$, defined in Eq.(2.25), and demanding $2R_y \lesssim \lambda_c$ yields a condition on the critical wavenumber $k_c = 2\pi/\lambda_c$:

$$k_c R_y = \pi. \tag{4.27}$$

To link this criterion to the anisotropy of the trapping potential, we use the definitions of chemical potential μ in (2.26), TF radius R_y in Eq.(2.25), and the critical wavevector $k_c = \sqrt{\mu}$. We obtain the relation for the critical anisotropy as

$$\omega_c = \frac{2}{\pi^3} gN \approx 0.0645\, gN. \tag{4.28}$$

This result indicates that the soliton is stabilized against the snake instability for anisotropies larger than ω_c. Notably, ω_c is smaller than the crossover anisotropy $\omega_s \approx 0.497\, gN$ identified earlier, where the system transitions from the 2DTF to the 1DTF regime. This suggests that stabilization occurs well before the condensate enters the quasi-one-dimensional limit, consistent with our observation that the soliton becomes dynamically stable while the condensate density is still well described by the 2DTF profile. In the next section, we refine our variational approach by incorporating the spatial inhomogeneity of the condensate density assuming a 2DTF background profile for $n(x, y)$.

4.4.2 Condensate with Thomas-Fermi Density

After studying a constant density system, we examine a more experimentally-realizable setup under the influence of an external potential $V(y) = \omega^2 y^2/2 \neq 0$ along the squeezing direction. We assume the contribution coming from the potential does not dominate over the self-interaction of the condensate, so that we can use the TF approximation for the density profile along the relevant direction:

$$n(y) = n\left(1 - \frac{y^2}{R_y^2}\right), \tag{4.29}$$

where R_y is the 2D TF radius in the squeezing direction derived in Sec.2.1.4. Therefore, our variational wavefunction transforms into

$$\psi = \sqrt{n}\sqrt{1 - \frac{y^2}{R_y^2}}\Big[\tanh\left(x/\xi_s\right) + \mathrm{i}(\alpha + \mathrm{i}\beta)\mathrm{sech}(x/\xi_s)\sin(ky)\Big]. \tag{4.30}$$

We show the calculation of each Lagrangian term in detail below:

The first term in the kinetic functional T becomes

$$\begin{aligned}\psi^*\dot{\psi} = n\left(1 - \frac{y^2}{R_y^2}\right)\Big[&\tanh(x/\xi_s)\mathrm{i}(\dot{\alpha} + \mathrm{i}\dot{\beta})\mathrm{sech}(x/\xi_s)\sin(ky) \\ &+(\alpha - \mathrm{i}\beta)(\dot{\alpha} + \mathrm{i}\dot{\beta})\mathrm{sech}^2(x/\xi_s)\sin^2(ky)\Big],\end{aligned}$$

so the functional T becomes

$$\begin{aligned}T &= \frac{\mathrm{i}}{2}\int \psi^*\dot{\psi} - \psi\dot{\psi}^*\mathrm{d}^2r = -\int \Im\{\psi^*\dot{\psi}\}\mathrm{d}^2r \\ \implies T &= -n\int_{-\infty}^{\infty}\mathrm{d}x\int_{-R_y}^{R_y}\mathrm{d}y\left(1 - \frac{y^2}{R_y^2}\right)\Big[\dot{\alpha}\underbrace{\cancelto{0}{\tanh(x/\xi_s)\mathrm{sech}(x/\xi_s)}}_{\text{odd symmetry in x-dir.}}\sin(ky) \\ &\qquad - (\beta\dot{\alpha} - \alpha\dot{\beta})\mathrm{sech}^2(x/\xi_s)\sin^2(ky)\Big] \\ \implies T &= n\xi_s R_y(\beta\dot{\alpha} - \alpha\dot{\beta})f(kR_y),\end{aligned} \tag{4.31}$$

where we define $f(x)$ as

$$f(x) = \frac{4}{3} + \frac{\cos(2x)}{x^2} - \frac{\sin(2x)}{2x^3}. \tag{4.32}$$

While calculating the derivation with respect to y, we act only on the perturbation term $\sin(ky)$, not on the background density $\sqrt{1 - y^2/R_y^2}$, because we only approximate that the density follows the TF profile as in Eq.(4.29). This approximation

is valid only in the regions where the self-interaction energy dominates over the kinetic contribution, containing spatial derivatives, as discussed in Sec.2.1.4. Approaching the edges, where the density (4.29) vanishes, the kinetic term will have a non-negligible effect and alter the density profile, and our approximation (4.29) validates. In fact, if we calculated the derivative of the density profile $\sqrt{1-y^2/R_y^2}$, we would find a diverging term in the Lagrangian. In order to overcome this issue, we choose not to perform the derivation of the density profile $\sqrt{1-y^2/R_y^2}$ and assume the solitonic perturbation makes a larger contribution to the kinetic term U_t. We will revisit this issue in the following subsection and continue the calculation as follows:

$$\begin{aligned}\implies |\nabla\psi|^2 \approx \frac{1}{\xi_s^2} n\left(1-\frac{y^2}{R_y^2}\right)\Big[&\mathrm{sech}^4(x/\xi_s) + 2\beta\,\mathrm{sech}^3(x/\xi_s)\tanh(x/\xi_s)\sin(ky)\\ &+(\alpha^2+\beta^2)\mathrm{sech}^2(x/\xi_s)\tanh^2(x/\xi_s)\sin^2(ky)\Big]\\ &+n\left(1-\frac{y^2}{R_y^2}\right)(\alpha^2+\beta^2)\mathrm{sech}^2(x/\xi_s)k^2\cos^2(ky).\end{aligned}$$

We again ignore the terms in the integrand that have no dependence on the variational parameters and do not show the calculations regarding those:

$$\begin{aligned}U_t = \frac{1}{2}n\int_{-\infty}^{\infty}\mathrm{d}x\int_{-h/2}^{h/2}\mathrm{d}y\Bigg[&\frac{2\beta}{\xi_s^2}\left(1-\frac{y^2}{R_y^2}\right)\underbrace{\mathrm{sech}^3(x/\xi_s)\tanh(x/\xi_s)}_{\text{odd symmetry in x-dir.}}\sin(ky)\to 0\\ &+\frac{1}{\xi_s^2}(\alpha^2+\beta^2)\mathrm{sech}^2(x/\xi_s)\left(1-\frac{y^2}{R_y^2}\right)\tanh^2(x/\xi_s)\sin^2(ky)\\ &+k^2(\alpha^2+\beta^2)\left(1-\frac{y^2}{R_y^2}\right)\mathrm{sech}^2(x/\xi_s)k^2\cos^2(ky)\Bigg]\\ \implies U_t = n\xi_s R_y(\alpha^2+\beta^2)&\left(\frac{1}{6\xi_s^2}+\frac{k^2}{2}\right)f(kR_y).\end{aligned} \tag{4.33}$$

In this model, the density becomes

$$\begin{aligned}|\psi|^2 = n\left(1-\frac{y^2}{R_y^2}\right)\Big[&\tanh^2(x/\xi_s)+(\alpha^2+\beta^2)\mathrm{sech}^2(x/\xi_s)\sin^2(ky)\\ &-2\beta\tanh(x/\xi_s)\mathrm{sech}(x/\xi_s)\sin(ky)\Big].\end{aligned}$$

Hence, we can calculate the chemical potential energy term U_μ in the Lagrangian as

$$\begin{aligned} U_\mu &= -\mu \int \mathrm{d}^2 r\ |\psi|^2 \\ &= -\mu n \int_{-\infty}^{\infty} \mathrm{d}x \int_{-R_y}^{R_y} \mathrm{d}y\ \left(1 - \frac{y^2}{R_y^2}\right) \Bigg[(\alpha^2+\beta^2)\mathrm{sech}^2(x/\xi_s)\sin^2(ky) \\ &\quad - 2\beta \underbrace{\tanh(x/\xi_s)\mathrm{sech}(x/\xi_s)}_{\text{odd symmetry in x-dir.}} \overset{\to 0}{\sin(ky)} \Bigg] \end{aligned}$$

$$\implies U_\mu = -\mu n \xi_s R_y (\alpha^2+\beta^2) f(kR_y), \tag{4.34}$$

and the trapping potential term U_v as

$$\begin{aligned} U_v &= \frac{\omega^2}{2} \int \mathrm{d}^2 r\ y^2 |\psi|^2 \\ &= \frac{\omega^2}{2} n \int_{-\infty}^{\infty} \mathrm{d}x \int_{-R_y}^{R_y} \mathrm{d}y\ \left(y^2 - \frac{y^4}{R_y^2}\right) \Bigg[(\alpha^2+\beta^2)\mathrm{sech}^2(x/\xi_s)\sin^2(ky) \\ &\quad - 2\beta \underbrace{\tanh(x/\xi_s)\mathrm{sech}(x/\xi_s)}_{\text{odd symmetry in x-dir.}} \overset{\to 0}{\sin(ky)} \Bigg]. \end{aligned}$$

$$\implies U_v = \omega^2 n \xi_s R_y^3 (\alpha^2+\beta^2) g_1(kR_y), \tag{4.35}$$

where we define

$$g_1(x) = \frac{2}{15} + \frac{x^2-3}{2x^4}\cos(2x) + \frac{3-5x^2}{4x^5}\sin(2x). \tag{4.36}$$

To calculate the interaction term U_g, first, we calculate

$$\begin{aligned} |\psi|^4 = n^2 \left(1 - \frac{y^2}{R_y^2}\right)^2 \Bigg[&\tanh^4(x/\xi_s) + (\alpha^2+\beta^2)^2 \mathrm{sech}^4(x/\xi_s)\sin^4(ky) \\ &+4\beta^2 \tanh^2(x/\xi_s)\mathrm{sech}^2(x/\xi_s)\sin^2(ky) \\ &+2(\alpha^2+\beta^2)\tanh^2(x/\xi_s)\mathrm{sech}^2(x/\xi_s)\sin^2(ky) \\ &-4\beta \tanh^3(x/\xi_s)\mathrm{sech}(x/\xi_s)\sin(ky) \\ &-4(\alpha^2+\beta^2)\beta \tanh(x/\xi_s)\mathrm{sech}^3(x/\xi_s)\sin^3(ky) \Bigg]. \end{aligned}$$

$$\implies U_g = \frac{g}{2}\int \mathrm{d}^2 r\ |\psi|^4$$

$$= \frac{gn^2}{2}\int_{-\infty}^{\infty}\mathrm{d}x\int_{-R_y}^{R_y}\mathrm{d}y\ \left(1-\frac{y^2}{R_y^2}\right)^2\Bigg[(\alpha^2+\beta^2)^2\mathrm{sech}^4(x/\xi_s)\sin^4(ky)$$

$$+4\beta^2\tanh^2(x/\xi_s)\mathrm{sech}^2(x/\xi_s)\sin^2(ky)$$

$$+2(\alpha^2+\beta^2)\tanh^2(x/\xi_s)\mathrm{sech}^2(x/\xi_s)\sin^2(ky)$$

$$-4\beta\underbrace{\tanh^3(x/\xi_s)\mathrm{sech}(x/\xi_s)}_{\text{odd symmetry in x-dir.}}\sin(ky) \to 0$$

$$-4(\alpha^2+\beta^2)\beta\underbrace{\tanh(x/\xi_s)\mathrm{sech}^3(x/\xi_s)}_{\text{odd symmetry in x-dir.}}\sin^3(ky) \to 0\Bigg].$$

$$\implies U_g = \frac{gn^2}{2}\left[(\alpha^2+\beta^2)^2\frac{4\xi_s}{3}R_y g_2(kR_y)+(\alpha^2+3\beta^2)\frac{4\xi_s}{3}R_y g_3(kR_y)\right]. \quad (4.37)$$

where we define $g_2(x)$ and $g_3(x)$ as

$$g_2(x) = \frac{2}{5}+\frac{3}{2x^4}\cos(2x)-\frac{3}{128x^4}\cos(4x)+\frac{4x^2-3}{4x^5}\sin(2x)$$
$$-\frac{16x^2-3}{512x^5}\sin(4x), \quad (4.38)$$

$$g_3(x) = \frac{8}{15}+\frac{3\cos(2x)}{2x^4}+(4x^2-3)\frac{\sin(2x)}{4x^5}. \quad (4.39)$$

After scaling every term in the Lagrangian with $(n\xi_s R_y f(kR_y))^{-1}$, our resulting Lagrangian becomes as

$$L = T - U$$

$$= (\beta\dot{\alpha}-\alpha\dot{\beta})-\left[\left(\frac{1}{6\xi_s^2}+\frac{k^2}{2}\right)-\mu+\omega^2R_y^2\tilde{g}_1(kR_y)+\frac{2gn}{3}\tilde{g}_3(kR_y)\right](\alpha^2+\beta^2) \quad (4.40)$$

$$-\frac{4gn}{3}\beta^2\tilde{g}_3(kR_y)-\frac{2gn}{3}(\alpha^2+\beta^2)^2\tilde{g}_2(kR_y),$$

where the functions with tilde $\tilde{g}_1$, $\tilde{g}_2$, and $\tilde{g}_3$ are just scaled versions with $f(kR_y)^{-1}$ of the corresponding functions g_1, g_2, and g_3

The resulting Euler-Lagrange equations for variational paramaters α and β become

$$\dot{\alpha} = \left[\left(\frac{1}{6\xi_s^2} + \frac{k^2}{2} - \mu \right) + \omega^2 R_y^2 \tilde{g}_1(kR_y) + 2gn\tilde{g}_3(kR_y) \right] \beta + \frac{4gn}{3}\beta(\alpha^2 + \beta^2)\tilde{g}_2(kR_y), \tag{4.41a}$$

$$\dot{\beta} = -\left[\left(\frac{1}{6\xi_s^2} + \frac{k^2}{2} - \mu \right) + \omega^2 R_y^2 \tilde{g}_1(kR_y) + \frac{2gn}{3}\tilde{g}_3(kR_y) \right] \alpha - \frac{4gn}{3}\alpha(\alpha^2 + \beta^2)\tilde{g}_2(kR_y). \tag{4.41b}$$

Noticing $g_1(x) + g_3(x) = f(x)/2$ and using the identities

$$\frac{1}{\xi_s^2} = \mu, \tag{4.42a}$$

$$R_y^2\omega^2 = 2\mu, \tag{4.42b}$$

$$gn = \mu, \tag{4.42c}$$

we simplify the equations to

$$\dot{\alpha} = \left[\frac{\mu}{6} + \frac{k^2}{2} \right] \beta + \frac{4\mu}{3}\beta(\alpha^2 + \beta^2)\tilde{g}_2(kR_y), \tag{4.43a}$$

$$\dot{\beta} = \left[\frac{\mu}{2} - \frac{k^2}{2} - \frac{4\mu}{3}\tilde{g}_1(kR_y) \right] \alpha - \frac{4\mu}{3}\alpha(\alpha^2 + \beta^2)\tilde{g}_2(kR_y). \tag{4.43b}$$

Again, we examine the stability around $(\alpha, \beta) = (0, 0)$ by linearizing the non-linear coupled equations around the origin of the parameter space. The square of the eigen-frequency Ω of the oscillation around the dark soliton becomes

$$\Omega(k)^2 = \left(\frac{\mu}{6} + \frac{k^2}{2} \right) \left(\frac{\mu}{2} - \frac{k^2}{2} - \frac{4\mu}{3}\frac{g_1(kR_y)}{f(kR_y)} \right). \tag{4.44}$$

The stabilization criterion of the dark soliton in this model can be calculated by setting the terms in the second parenthesis to zero. Using the 2DTF definition of μ (2.26), we obtain that the stabilization for the perturbation with mode k is established when the anisotropy ω has larger values than the critical ansitropy $\omega_c(k)$ satisfying the relation

$$\frac{\omega_c(k)}{gN} = \frac{4}{\pi(kR_y)^2} \left(\frac{1}{2} - \frac{4}{3}\frac{g_1(kR_y)}{f(kR_y)} \right). \tag{4.45}$$

The right-hand side of the equation is a monotonic decreasing function and diverges in the long-wavelength limit. This means the ansatz introduced in Eq.(4.30) does not provide a maximum anisotropy ratio ω freezing all perturbations, causing snake instability. This artifact of the model is discussed in the following subsection.

However, we can still use this model to interpret the suppression of snake instability in 2D anisotropic Bose gases. We will use a similar physical intuition introduced in the previous section; that is, we will assume modes with smaller wavenumbers after a critical wavenumber k_c will be assumed to be non-excitable due to the size of the system. Before choosing an appropriate value for the critical wavenumber k_c to investigate the stabilization of snake instability, we provide the numerical time evolution of the 2D GP equation with anisotropic trap near the critical anisotropy suppressing snake instability in Fig.4.6. As presented, the last mode survives near the critical anisotropy has a wavelength satisfying $\frac{\lambda_c}{2} \approx 2R_y$, which yields a relation for the wavenumber

$$k_c R_y \approx \frac{\pi}{2}$$

rather than the one introduced in Eq.(4.27) and in Ref.[13].

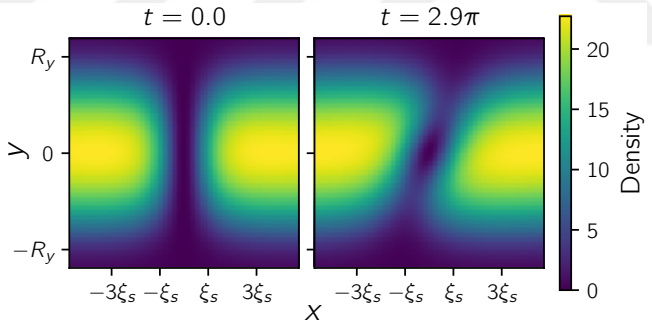

Figure 4.6: The real-time dynamical evolution of an unstable dark soliton for $gN = 200$ inside a trapping potential with a near-critical anisotropy ratio $\omega = 8$. The color-bar shows the density. Approaching the critical anisotropy, the unstable dark soliton decays through an odd-in-y perturbation with a single vortex at the center.

To make a physically motivated choice, we consider the fact that in the TF regime, the local chemical potential varies across the transverse direction as $\mu(y) = \mu\left(1 - y^2/R_y^2\right)$. In the constant-density approximation, the last unstable mode corresponds to $k \simeq \sqrt{\mu}$. In analogy, we now take the transverse average of the local healing scale and

define an effective wavenumber

$$\bar{k}_c = \frac{k_c}{2R_y} \int_{-R_y}^{R_y} \sqrt{1 - \frac{y^2}{R_y^2}}\, dy = k_c\, \frac{\pi}{4}, \tag{4.46}$$

which yields

$$\bar{k}_c R_y = \frac{\pi}{2} \implies k_c R_y = 2. \tag{4.47}$$

Substituting this value into Eq. (4.45) defines the critical anisotropy:

$$\omega_c = \frac{1}{\pi}\left(\frac{1}{2} - \frac{4g_1(2)}{3f(2)}\right) gN \simeq 0.0847\, gN. \tag{4.48}$$

This estimate represents an improved stabilization threshold that incorporates both the inhomogeneous background density and the spatial structure of the perturbation.

4.4.3 Condensate with Gaussian Density Profile

The variational approach developed in the previous section provides valuable insight into the dynamical stability of a dark soliton in an anisotropic trap. However, it also exhibits an important notable shortcoming that we now aim to address: The current analysis predicts the existence of unstable modes in the long-wavelength limit (small k) for any finite condensate, even though the background density vanishes outside a finite region. Physically, however, transverse modulations with wavelengths exceeding the size of the condensate should be suppressed due to the lack of supporting density at large y. The presence of persistent long-wavelength instability despite the finite extent of the condensate is thus an unphysical artifact of the current formulation.

To study the snake instability in this geometry, we now construct a variational ansatz analogous to Eq. (4.2), including transverse modulations and using the same Gaussian envelope:

$$\psi = \frac{\sqrt{n}}{\sqrt[4]{\pi\sigma_y^2}} e^{-\frac{y^2}{2\sigma_y^2}} \Big[\tanh\left(x/\xi_s\right) + \mathrm{i}(\alpha + \mathrm{i}\beta)\, \mathrm{sech}(x/\xi_s) \sin(ky) \Big], \tag{4.49}$$

where σ_y is the Gaussian width in the confined direction, and n is the constant parameter that controls the peak density.

The functional T is calculated as

$$
\begin{aligned}
T &= \frac{\mathrm{i}}{2}\int \psi^*\dot{\psi} - \psi\dot{\psi}^*\mathrm{d}^2r = -\int \Im\{\psi^*\dot{\psi}\}\mathrm{d}^2r \\
\implies T &= -\frac{n}{\sigma_y\sqrt{\pi}}\int_{-\infty}^{\infty}\mathrm{d}x\int_{-\infty}^{\infty}\mathrm{d}y\, e^{-\frac{y^2}{\sigma_y^2}}\Big[\underbrace{\dot{\alpha}\tanh(x/\xi_s)\mathrm{sech}(x/\xi_s)}_{\text{odd symmetry in x-dir.}}\to 0\ \sin(ky) \\
&\qquad\qquad -(\beta\dot{\alpha}-\alpha\dot{\beta})\mathrm{sech}^2(x/\xi_s)\sin^2(ky)\Big] \\
\implies T &= n\xi_s\left(1-e^{-k^2\sigma_y^2}\right)(\beta\dot{\alpha}-\alpha\dot{\beta}) \qquad (4.50)
\end{aligned}
$$

We calculate the kinetic energy term U_t using the full derivative:

$$
\begin{aligned}
U_t &= \int \mathrm{d}^2r\frac{1}{2}|\nabla\psi|^2 \\
&= \frac{1}{2}\frac{n}{\sigma_y\sqrt{\pi}}\int_{-\infty}^{\infty}\mathrm{d}x\int_{-\infty}^{\infty}\mathrm{d}y\,\Bigg[\frac{2\beta}{\xi_s^2}e^{-\frac{y^2}{\sigma_y^2}}\underbrace{\mathrm{sech}^3(x/\xi_s)\tanh(x/\xi_s)}_{\text{odd symmetry in x-dir.}}\to 0\ \sin(ky) \\
&+\frac{1}{\xi_s^2}e^{-\frac{y^2}{\sigma_y^2}}(\alpha^2+\beta^2)\mathrm{sech}^2(x/\xi_s)\tanh^2(x/\xi_s)\sin^2(ky) \\
&+e^{-\frac{y^2}{\sigma_y^2}}(\alpha^2+\beta^2)\mathrm{sech}^2(x/\xi_s)\left(\frac{y^2}{\sigma_y^4}\sin^2(ky)+k^2\cos^2(ky)\right) \\
&-e^{-\frac{y^2}{\sigma_y^2}}(\alpha^2+\beta^2)\mathrm{sech}^2(x/\xi_s)\underbrace{2k\frac{y}{\sigma_y^2}\sin(ky)\cos(ky)}_{\text{odd symmetry in y-dir.}}\to 0\Bigg]
\end{aligned}
$$

$$
\begin{aligned}
U_t &= \frac{n}{2}(\alpha^2+\beta^2)\Bigg[\frac{1}{\xi_s^2}\frac{2\xi_s}{3}\frac{\left(1-e^{-k^2\sigma_y^2}\right)}{2} \\
&\quad +2\xi_s\frac{1}{4\sigma^2}\left(1-e^{-k^2\sigma_y^2}+2k^2\sigma_y^2e^{-k^2\sigma_y^2}\right)+k^2 2\xi_s\frac{\left(1-e^{-k^2\sigma_y^2}\right)}{2}\Bigg] \\
\implies U_t &= n\xi_s\left(1-e^{-k^2\sigma_y^2}\right)(\alpha^2+\beta^2)\left(\frac{1}{6\xi_s^2}+\frac{1}{4\sigma_y^2}\right)+n\xi_s(\alpha^2+\beta^2)\frac{k^2}{2} \qquad (4.51)
\end{aligned}
$$

The density becomes

$$
\begin{aligned}
|\psi|^2 = \frac{n}{\sqrt{\pi}\sigma_y}e^{-\frac{y^2}{\sigma_y^2}}\Bigg[&\tanh^2(x/\xi_s)+(\alpha^2+\beta^2)\mathrm{sech}^2(x/\xi_s)\sin^2(ky) \\
&-2\beta\tanh(x/\xi_s)\mathrm{sech}(x/\xi_s)\sin(ky)\Bigg].
\end{aligned}
$$

Therefore, we calculate the chemical potential term U_μ as

$$\begin{aligned} U_\mu &= -\mu \int \mathrm{d}^2 r\ |\psi|^2 \\ &= -\mu \frac{n}{\sqrt{\pi}\sigma_y} \int_{-\infty}^{\infty} \mathrm{d}x \int_{-\infty}^{\infty} \mathrm{d}y e^{-\frac{y^2}{\sigma_y^2}} \Bigg[(\alpha^2+\beta^2)\mathrm{sech}^2(x/\xi_s)\sin^2(ky) \\ &\quad - 2\beta \underbrace{\tanh(x/\xi_s)\mathrm{sech}(x/\xi_s)}_{\text{odd symmetry in x-dir.}} \cancelto{0}{} \sin(ky) \Bigg] \\ \implies U_\mu &= -\mu n \xi_s \left(1 - e^{-k^2\sigma_y^2}\right)(\alpha^2+\beta^2), \end{aligned} \tag{4.52}$$

and trapping the potential term U_v as

$$\begin{aligned} U_v &= \frac{\omega^2}{2} \int \mathrm{d}^2 r\ y^2 |\psi|^2 \\ &= \frac{\omega^2}{2} \frac{n}{\sqrt{\pi}\sigma_y} \int_{-\infty}^{\infty} \mathrm{d}x \int_{-\infty}^{\infty} \mathrm{d}y\ y^2 e^{-\frac{y^2}{\sigma_y^2}} \Bigg[(\alpha^2+\beta^2)\mathrm{sech}^2(x/\xi_s)\sin^2(ky) \\ &\quad - 2\beta \underbrace{\tanh(x/\xi_s)\mathrm{sech}(x/\xi_s)}_{\text{odd symmetry in x-dir.}} \cancelto{0}{} \sin(ky) \Bigg] \\ \implies U_v &= n\xi_s \frac{\omega^2\sigma_y^2}{4}\left(1 - e^{-k^2\sigma_y^2}\right)(\alpha^2+\beta^2) + n\xi_s \frac{\omega^2\sigma_y^2}{2}(k\sigma_y)^2 e^{-k^2\sigma_y^2}(\alpha^2+\beta^2). \end{aligned} \tag{4.53}$$

The square of the density is

$$\begin{aligned} |\psi|^4 = \frac{n^2}{\pi\sigma_y^2} e^{-\frac{2y^2}{\sigma_y^2}} \Bigg[& \tanh^4(x/\xi_s) + (\alpha^2+\beta^2)^2 \mathrm{sech}^4(x/\xi_s)\sin^4(ky) \\ & + 4\beta^2 \tanh^2(x/\xi_s)\mathrm{sech}^2(x/\xi_s)\sin^2(ky) \\ & + 2(\alpha^2+\beta^2)\tanh^2(x/\xi_s)\mathrm{sech}^2(x/\xi_s)\sin^2(ky) \\ & - 4\beta \tanh^3(x/\xi_s)\mathrm{sech}(x/\xi_s)\sin(ky) \\ & - 4(\alpha^2+\beta^2)\beta \tanh(x/\xi_s)\mathrm{sech}^3(x/\xi_s)\sin^3(ky) \Bigg]. \end{aligned}$$

Thus, the self-interaction term U_g becomes

$$
\begin{aligned}
U_g &= \frac{g}{2}\int \mathrm{d}^2 r\ |\psi|^4 \\
&= \frac{g}{2}\frac{n^2}{\pi\sigma_y^2}\int_{-\infty}^{\infty}\mathrm{d}x\int_{-\infty}^{\infty}\mathrm{d}y\ e^{-\frac{2y^2}{\sigma_y^2}}\Bigg[(\alpha^2+\beta^2)^2\mathrm{sech}^4(x/\xi_s)\sin^4(ky) \\
&\qquad + 4\beta^2\tanh^2(x/\xi_s)\mathrm{sech}^2(x/\xi_s)\sin^2(ky) \\
&\qquad + 2(\alpha^2+\beta^2)\tanh^2(x/\xi_s)\mathrm{sech}^2(x/\xi_s)\sin^2(ky) \\
&\qquad - 4\beta\underbrace{\tanh^3(x/\xi_s)\mathrm{sech}(x/\xi_s)}_{\text{odd symmetry in y-dir.}}\sin(ky) \\
&\qquad - 4(\alpha^2+\beta^2)\beta\underbrace{\tanh(x/\xi_s)\mathrm{sech}^3(x/\xi_s)}_{\text{odd symmetry in y-dir.}}\sin^3(ky)\Bigg]
\end{aligned}
$$

$$
\begin{aligned}
\implies U_g &= \frac{g}{2}\frac{n^2}{\pi\sigma_y^2}\Bigg[(\alpha^2+\beta^2)^2\frac{4\xi_s}{3}\frac{\sigma_y\sqrt{\pi}}{8\sqrt{2}}\left(3-4e^{-k^2\sigma_y^2/2}+e^{-2k^2\sigma_y^2}\right) \\
&\qquad + 2(\alpha^2+3\beta^2)\frac{2\xi_s}{3}\frac{\sigma_y\sqrt{\pi}}{2\sqrt{2}}\left(1-e^{-k^2\sigma_y^2/2}\right)\Bigg] \\
U_g &= \frac{gn^2\xi_s}{3\sigma_y\sqrt{2\pi}}\left(1-e^{-k^2\sigma_y^2/2}\right)(\alpha^2+3\beta^2) \\
&\qquad + \frac{gn^2\xi_s}{12\sigma_y\sqrt{2\pi}}\left(3-4e^{-k^2\sigma_y^2/2}+e^{-2k^2\sigma_y^2}\right)(\alpha^2+\beta^2)^2 \qquad (4.54)
\end{aligned}
$$

After scaling every term in Eq.(4.50)-(4.54)with $\left(n\xi_s(1-e^{-z^2})\right)^{-1}$, where $z=k\sigma_y$, our resulting Lagrangian becomes as

$$
\begin{aligned}
L &= T-U \\
&= (\beta\dot{\alpha}-\alpha\dot{\beta}) - (\alpha^2+\beta^2)\left[\frac{1}{6\xi_s^2}+\frac{1}{4\sigma_y^2}+\frac{z^2}{2\sigma_y^2}\left(\frac{1+\omega^2\sigma_y^4e^{-z^2}}{1-e^{-z^2}}\right)-\mu+\frac{\omega^2\sigma_y^2}{4}\right] \\
&- \frac{gn}{3\sigma_y\sqrt{2\pi}}\frac{1-e^{-z^2/2}}{1-e^{-z^2}}(\alpha^2+3\beta^2) - \frac{gn}{12\sigma_y\sqrt{2\pi}}\frac{3-4e^{-z^2/2}+e^{-2k^2\sigma_y^2}}{1-e^{-z^2}}(\alpha^2+\beta^2)^2.
\end{aligned} \qquad (4.55)
$$

Using the relations

$$\tilde{\mu} = \mu - \frac{1+\omega^2\sigma_y^2}{4\sigma_y^2}, \tag{4.56a}$$

$$\tilde{g} = \frac{g}{\sqrt{2\pi}\sigma_y}, \tag{4.56b}$$

$$n = \frac{\tilde{\mu}}{\tilde{g}} = \left(\frac{3N}{8\sqrt{\pi}\sigma_y g^2}\right)^{2/3}, \tag{4.56c}$$

$$\xi_s^2 = \frac{1}{\tilde{\mu}}, \tag{4.56d}$$

the Lagrangian can be rewritten as

$$L = \beta\dot{\alpha} - \alpha\dot{\beta} + \left(\frac{5\tilde{\mu}}{6} - \frac{z^2}{2\sigma_y^2}\frac{1+\omega^2\sigma_y^4 e^{-z^2}}{1-e^{-z^2}}\right)(\alpha^2+\beta^2) - \frac{\tilde{\mu}}{3}\frac{1}{1+e^{-z^2}}(\alpha^2+3\beta^2) - \frac{\tilde{\mu}}{12}\frac{3-4e^{-z^2/2}+e^{-2z^2}}{1-e^{-z^2}}((\alpha^2+\beta^2))^2. \tag{4.57}$$

The linearized dynamical equations take the form

$$\dot{\alpha} = -\left[\frac{5}{6}\tilde{\mu} - \frac{\tilde{\mu}}{(1+e^{-z^2/2})} - \frac{z^2(1+\omega^2\sigma_y^4 e^{-z^2})}{2\sigma_y^2(1-e^{-z^2})}\right]\beta, \tag{4.58a}$$

$$\dot{\beta} = +\left[\frac{5}{6}\tilde{\mu} - \frac{\tilde{\mu}}{3(1+e^{-z^2/2})} - \frac{z^2(1+\omega^2\sigma_y^4 e^{-z^2})}{2\sigma_y^2(1-e^{-z^2})}\right]\alpha. \tag{4.58b}$$

A key observation is that, unlike in the TF treatment, the above equations admit completely stable solutions for all k, including the low-wavenumber limit $k \to 0 \implies z \to 0$. Using the relation

$$\sigma_y = \frac{1}{\sqrt{\omega}},$$

the oscillation eigenfrequency satisfy the equation

$$\Omega^2 = \left(\frac{\tilde{\mu}}{3} - \omega\right)\left(\frac{2\tilde{\mu}}{3} - \omega\right), \tag{4.59}$$

which takes positive values when $\omega < \frac{\tilde{\mu}}{3}$ or $\omega > \frac{2\tilde{\mu}}{3}$. This result yields a simple condition for complete stabilization in the large anisotropy limit:

$$\omega \geq \frac{2}{3}\tilde{\mu}. \tag{4.60}$$

Using the 1DTF expression for $\tilde{\mu}$, the condition obtained above defines the critical anisotropy ratio in the Gaussian density model:

$$\omega_c = \left(\frac{2}{3}\right)^{3/2}\frac{3}{8\sqrt{\pi}}\,gN \simeq 0.115\,gN. \tag{4.61}$$

This value is still too low to justify the 1DTF limit used in its derivation. In this sense, the calculation is internally inconsistent, as it predicts stabilization in a parameter regime where the assumed Gaussian profile is no longer appropriate. Nonetheless, the calculation provides an important insight: admit completely stable solutions for all k, including the low-wavenumber limit $k \to 0 \implies z \to 0$.

4.5 Comparison with Numerical Simulations

To validate the analytical predictions and accurately determine the critical anisotropy for stabilization, we perform time-dependent GP simulations for varying trap geometries. For each value of anisotropy ω, we begin by preparing a stationary soliton configuration. This is achieved by imposing odd parity under reflection $x \to -x$, which enforces a nodal plane at $x = 0$, and evolving the GP equation in imaginary time. This procedure yields a metastable soliton state consistent with the imposed symmetry and the given trap parameters.

Once the initial soliton state is prepared, we evolve the system in real time and monitor its dynamical stability. To quantify the persistence of the soliton, we define a time-dependent overlap function

$$F(t) = \left| \int \mathrm{d}x\, \mathrm{d}y\, \psi^*(x, y, t)\, \psi(x, y, 0)\, \frac{1}{\cosh^2(x/\xi_s)} \right|, \tag{4.62}$$

which measures the projection of the evolving wavefunction onto the initial soliton state, weighted by the localized profile of the soliton. For a stable soliton, this quantity exhibits bounded oscillations over time, reflecting coherent motion of the perturbation. In contrast, for an unstable soliton, $F(t)$ remains initially steady but then exhibits an abrupt decay at a time determined by the growth of unstable modes seeded by numerical noise.

Figure 4.7 illustrates this behavior by showing the time evolution of $F(t)$ for two representative cases: one in the stable regime and one in the unstable regime. We define the soliton to be dynamically stable if the value of $F(t)$ remains within 1% of its initial value over a duration of $\omega_x t = 5\pi$, corresponding to several trap periods. While the exact threshold for stability could in principle depend on the length of the

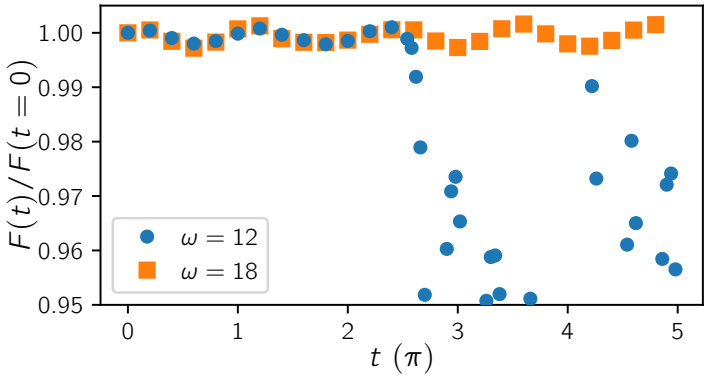

Figure 4.7: The time evolution of the overlap function $F(t)$ defined in Eq.(4.62) for two different trap anisotropies and $gN = 200$. Below the critical anisotropy (circle), the dark soliton decays into vortices and $F(t)$ rapidly drops below 1% of its initial value, whereas beyond the critical value (square), the overlap F stays almost the same.

simulation and the sensitivity to numerical noise, we find that this criterion is robust given our numerical accuracy and observed error accumulation.

Applying this stability condition across a range of parameters, we extract the critical anisotropy ω_c as a function of interaction strength and particle number. Remarkably, we find that the resulting critical line is well approximated by

$$\omega_c^{(\mathrm{num})} = 0.0833\, gN, \tag{4.63}$$

which agrees closely with our analytical prediction $\omega_c \simeq 0.0847\, gN$ derived from the variational model with a TF background, as compared in Fig.4.8. The numerical and analytical values are so close that the match is likely somewhat fortuitous; however, it reinforces the validity of the underlying physical picture.

4.6 Conclusion

In this chapter, we investigated the snake instability of dark solitons in two-dimensional BECs confined by anisotropic harmonic traps. While previous studies have primarily relied on Bogoliubov-de Gennes linear stability analysis, we proposed an alternative analytical framework based on a carefully constructed variational wavefunction. This

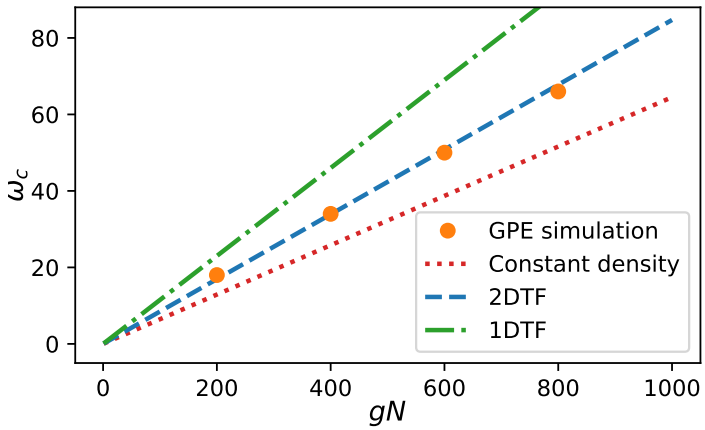

Figure 4.8: Critical anisotropy ratio ω_c as a function of the parameter gN. Orange dots indicate the values obtained from numerical GP simulations. The numerical uncertainties are smaller than the marker size for all simulation points. Three theoretical predictions are shown for comparison: the constant-density approximation (dotted), the 2DTF model (dashed), and the 1DTF model (dash-dotted). The constant-density model slightly underestimates the critical anisotropy, and the 1DTF model appears to overestimate it, whereas the 2DTF model provides an excellent fit to the numerical data.

variational ansatz provides a unified description of dark solitons, solitonic vortices, and single vortex states using a small number of tunable parameters.

We first tested our approach in a simplified setup with constant background density and demonstrated that the suppression of the snake instability for vertical wave numbers k satisfying $k^2 > \sqrt{\mu}$ is consistent with earlier analytical predictions [85, 13]. We then extended our analysis to include a harmonic trapping potential, which strongly influences the condensate density profile. Assuming a TF-like profile along the squeezed direction, we examined how spatially varying density affects the suppression of snake instability. Our variational results showed excellent agreement with full numerical solutions of the GP equation. Additionally, we demonstrated that instability modes at low k can also be suppressed when the density profile is chosen to be a smooth function, such as a Gaussian. In this case, the inclusion of transverse kinetic energy contributes to the stabilization of all perturbation modes, including long-wavelength ones.

Beyond serving as an effective analytical tool for understanding soliton decay and vortex formation in 2D, our variational framework opens several promising research directions. One natural extension is to three-dimensional condensates, where the decay of solitons can give rise to vortex rings—structures that require more sophisticated ansätze to describe [86, 87]. Another is the generalization to gray solitons, which move with finite velocity and thus require disentangling the soliton's motion from the instability modes [88]. Our approach may also be adapted to incorporate dissipative effects such as thermal damping or atom loss, which are important for understanding the long-time dynamics and decay pathways of solitons in realistic experimental settings [70, 89]. Furthermore, with recent advances in the creation of flat box potentials and designer confinement geometries, our method could be used to explore soliton stability and vortex dynamics in a wide variety of external potentials [83]. Together, these extensions promise to advance the theoretical understanding of nonlinear excitations and their instabilities in quantum fluids.

CHAPTER 5

VORTICES AND FRACTIONAL QUANTUM HALL STATES IN A RAPIDLY ROTATING ANISOTROPIC BOSE GAS

In this section, we present a theoretical framework for a rapidly rotating anisotropic Bose gas. Starting from the second-quantized Hamiltonian for a rotating Bose gas with contact interactions in two dimensions, we focus on the rapid rotation limit—where the rotation frequency matches the weak trap frequency—and show how the system maps to the Landau gauge in cylindrical geometry. In this setting, the presence of edges along the open direction of the cylinder plays a crucial role in shaping the system's properties. By projecting the full Hamiltonian (including both kinetic and interaction terms) onto the LLL, we derive a compact two-parameter model that captures the effects of interaction strength, rotation rate, and anisotropy. This model resembles a tight-binding chain with all-to-all long-range interactions and features both conventional conserved quantities, such as the total number of particles in the chain, and unconventional ones, such as the center of mass coordinate—which corresponds to the total momentum along the translationally invariant (periodic) direction.

Using exact diagonalization (ED) [90, 91] and density matrix renormalization group (DMRG) methods [67, 92], we uncover a phase diagram that unifies uniform BECs, various vortex lattice structures, and strongly correlated phases, while also highlighting the distinctive physics arising from the system's edges. To identify different phases with broken symmetries and/or topological order, we employ a variety of diagnostic tools, including the particle-hole energy gap, entanglement entropy, and the overlap with the Laughlin wavefunction in cylindrical geometry.

This section is organized as follows: In Sec. 5.1, we introduce the model Hamiltonian projected to the LLL. In Sec. 5.2, we present details of the phase diagram featuring a

uniform Bose gas, various vortex lattices, and FQH states. In Sec. 5.3, we present a discussion of our results and finish with conclusions and outlook.

5.1 Model

We consider a single-component quasi-two-dimensional bosonic gas rotating about the z-axis, which is perpendicular to the confinement plane. By integrating out the z-direction, we obtain a two-dimensional Hamiltonian [93]

$$\hat{H} = \int \mathrm{d}^2 r \left[\hat{\Psi}^\dagger(\mathbf{r}) \hat{H}_0 \hat{\Psi}(\mathbf{r}) + \frac{g_{\mathrm{2D}}}{2} \hat{\Psi}^\dagger(\mathbf{r}) \hat{\Psi}^\dagger(\mathbf{r}) \hat{\Psi}(\mathbf{r}) \hat{\Psi}(\mathbf{r}) \right], \tag{5.1}$$

where $\mathbf{r} = (x, y)$, $\hat{\Psi}(\mathbf{r})$ and $\hat{\Psi}^\dagger(\mathbf{r})$ are bosonic annihilation and creation operators with commutation $[\hat{\Psi}(\mathbf{r}), \hat{\Psi}^\dagger(\mathbf{r}')] = \delta(\mathbf{r}-\mathbf{r}')$, $g_{\mathrm{2D}} = \sqrt{8\pi}\hbar^2 a_s / a_z m$ is the effective 2D interaction strength, a_s is the s-wave scattering length, a_z is the harmonic oscillator length in the z-direction, and m is the mass. The non-interacting Hamiltonian $\hat{H}_0$ describes a rapidly rotating system with angular velocity $\Omega\hat{z}$ and anisotropic trapping potential, written in the rotating reference frame as

$$\hat{H}_0 = -\frac{\hbar^2}{2m}\nabla^2 + \frac{1}{2}m\omega_x^2 x^2 + \frac{1}{2}m\omega_y^2 y^2 - \Omega L_z, \tag{5.2}$$

$L_z = x p_y - y p_x$ is the z-component of angular momentum, ω_x and ω_y are trap frequencies in the x- and y-directions, respectively.

In what follows, we focus on the anisotropic rapid rotation limit defined as $\Omega \approx \omega_x$ and $\Omega < \omega_y$. In this limit, we assume the trapping in the x-direction vanishes so that our model describes a 2D system trapped only in the y-direction. Applying a gauge transformation to our field operators $\hat{\Psi} \rightarrow e^{\mathrm{i}m\Omega xy/\hbar}\hat{\Psi}$ leaves the interaction term invariant, but the single-particle Hamiltonian becomes

$$\hat{H}_0 = \frac{1}{2m}(-\mathrm{i}\hbar\partial_x + 2m\Omega y)^2 - \frac{\hbar^2}{2m}\partial_y^2 + \frac{1}{2}m(\omega_y^2 - \Omega^2)y^2 \tag{5.3}$$

This is the non-interacting Hamiltonian of the quantum Hall system in the Landau gauge with added trap potential in the y-direction, as discussed in Sec.2.2.1.1. The effective electron charge q^* and magnetic field B^* map to $q^*B^* = 2m\Omega$ [2]. Since the Hamiltonian commutes with the momentum operator in the x-direction $\hat{p}_x$, the eigenfunctions are of the form $e^{\mathrm{i}kx}\phi_k(y)$. We assume periodic boundary conditions

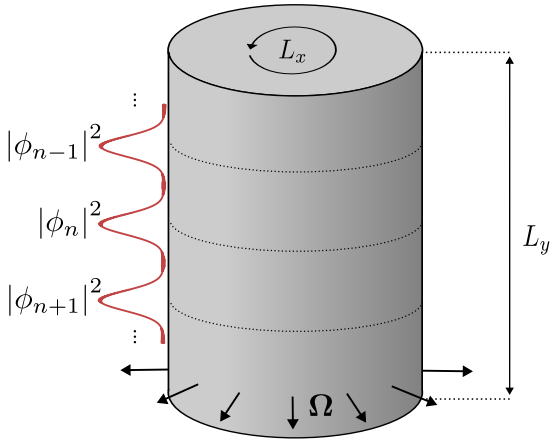

Figure 5.1: Geometry of the 2D rotating atomic Bose gas in the Landau gauge and schematic representation of the eigenfunctions of the noninteracting Hamiltonian.

along the x-direction; thus, the wavevectors can be written as $k = 2\pi n/L_x$ where L_x is the size of the system in the x-direction, as illustrated in Figure 5.1.

The effective Hamiltonian $\hat{H}_n$ for the functions $\phi_n(y) \equiv \phi_{k_n}(y)$ can be obtained as

$$\hat{H}_n = -\frac{\hbar^2\partial_y^2}{2m} + \frac{1}{2}m\omega_c^2(y+y_n)^2 + \frac{\hbar^2 k_n^2}{2m_*}, \tag{5.4}$$

where $\omega_c = \sqrt{3\Omega^2+\omega_y^2}$, $\frac{m}{m_*} = 1 - \frac{4\Omega^2}{\omega_c^2}s$, $y_n = \frac{2\Omega}{\omega_c}k_n\ell^2$, and $\ell^2 = \frac{\hbar}{m\omega_c}$. The effective Hamiltonian $\hat{H}_n$ corresponds to the familiar quantum harmonic oscillator localized at the center $y = -y_n$. Thus, the eigenvalues with the lowest oscillation energy of the effective Hamiltonian H_n are

$$\varepsilon_n = \frac{\hbar\omega_c}{2} + \frac{\hbar^2 k^2}{2m^*}, \tag{5.5}$$

and the corresponding normalized eigenfunctions are

$$\varphi_n(x,y) = \frac{1}{\sqrt{L_x}}e^{ik_n x}\frac{1}{(\pi\ell^2)^{1/4}}e^{-\frac{1}{2\ell^2}(y+y_n)^2}. \tag{5.6}$$

Assuming that the Landau level spacing $\hbar\omega_c$ is much bigger than other energy scales in the system, we project the Hamiltonian to the LLL using the expansion of the field operators

$$\hat{\Psi}(x,y) = \sum_n \hat{a}_n\varphi_n(x,y) \tag{5.7}$$

where $\hat{a}_n$ and $\hat{a}_n^\dagger$ are canonical bosonic annihilation and creation operators in state φ_n with commutation $[\hat{a}_n, \hat{a}_{n'}^\dagger] = \delta_{n,n'}$. Hence, the full many-body Hamiltonian takes the

following form in the LLL manifold [94]

$$\hat{H} = \sum_{n} n^2 \hat{a}_n^\dagger \hat{a}_n + \sum_{n_1,n_2,n_3} V_{n_1,n_2,n_3} \hat{a}_{n_1}^\dagger \hat{a}_{n_2}^\dagger \hat{a}_{n_3} \hat{a}_{n_4}, \tag{5.8}$$

where $n_4 = n_1 + n_2 - n_3$, and the interaction matrix elements are written as

$$V_{n_1,n_2,n_3} = g e^{-2\pi^2\gamma^2\left[(n_1-n_3)^2+(n_2-n_3)^2\right]}, \tag{5.9}$$

with the dimensionless interaction strength given by

$$g = \frac{1}{2\pi^2} \frac{L_x}{\ell} \frac{m_*}{m} \frac{a_s}{a_z}. \tag{5.10}$$

In Eq. (5.8), we rescale the total Hamiltonian with energy $\frac{\hbar^2}{2m_*}\frac{4\pi^2}{L_x^2}$, drop the overall constant $\frac{1}{4\pi^2}\frac{m_*}{m}\frac{L_x^2}{\ell^2}$ from the quadratic term, which corresponds to the zero-point energy of the LLL, and define

$$\gamma = \frac{\ell}{L_x} \frac{2\Omega}{\omega_c}. \tag{5.11}$$

This expression is renormalized by the trapping factor $2\Omega/\omega_c$ with respect to the earlier definition in Ref. [95]. The Hamiltonian in Eq. (5.8) conserves the total number of particles, which can be written as

$$N = \sum_{n} \hat{a}_n^\dagger \hat{a}_n. \tag{5.12}$$

Furthermore, due to the translational invariance along the x-direction, total momentum along x is also conserved, which we write in dimensionless form as

$$K = \sum_{n} n \hat{a}_n^\dagger \hat{a}_n. \tag{5.13}$$

Overall, we mapped our rapidly rotating anisotropic 2D many-body problem in Eq.(5.1) to an effective chain of atoms inside a harmonic trap with long-range interaction in Eq.(5.8). We emphasize that the effective trap potential is solely the result of the anisotropy of the harmonic confinement in the original problem. If the trap were isotropic, then we would not have such a contribution in our Hamiltonian (5.8) due to diverging behaviour of m_* in the isotropic limit. The ground state in this limit would correspond to the Laughlin wave function as studied in Refs.[95, 96].

Thanks to the trapping potential in the chain model, the interacting Bose accumulates around the center site $n = 0$. Increasing interaction strength g will lead to dispersing

the accumulated Bose gas, and the number of occupied sites will increase. In this work, we will set the number of sites in the chain as the least number of sites required for a Laughlin state . This state corresponds to the Laughlin state with filling $\nu = 1/2$; therefore, we will choose $N_v = 2N$ many sites in the chain and investigate the quantum phase transition of the system described by the Hamiltonian in Eq.(5.8). This restriction causes the real 2D system to have a finite size L_y along the squeezing axis, so we impose the so-called guiding centers y_n to be inside the sample domain $-L_y/2 \leq y_n < L_y/2$. Using $k_n = 2\pi n/L_x$ and the definition of $y_n = \frac{2\Omega}{\omega_c} k_n \ell^2$ written after Eq. (5.4), this leads to

$$-\frac{N_v}{2} \leq n < \frac{N_v}{2}, \tag{5.14}$$

where

$$N_v = \frac{L_x L_y}{2\pi\ell^2} \frac{\omega_c}{2\Omega}. \tag{5.15}$$

In the isotropic limit $\omega_c \to 2\Omega$, this quantity becomes the standard definition of the number of vortices in a superfluid[2] and takes place of the number of magnetic flux quanta in the electronic quantum Hall problem, introduced in Eq.2.51 in Sec.(2.2.1.1). Thus, from now on, we refer to N_v as the "number of vortices" in the system.

We now interpret the effective 1D model parameters g and γ in terms of the original 2D system, which is governed by experimentally tunable quantities such as the trap anisotropy ω_y/ω_x, the rotation frequency Ω, the interaction strength $g_{2\mathrm{D}}$, and the average density of the Bose gas $\bar{n}$. We consider the system in the rapid rotation limit $\Omega \to \omega_x$, where the gas becomes infinitely elongated along the x-direction. This effective description can be interpreted experimentally as modeling an elongated Bose gas with a density profile $\bar{n}(y)$, which is nearly constant along the elongated direction but varying along the squeezed (y) direction, as observed in Ref. [97]. Due to the approximate uniformity of $\bar{n}$ along x, it is natural to impose periodic boundary conditions encapsulating N number of particles within a strip with length L_x. The ratio of these quantities can be calculated as

$$\frac{N}{L_x} = n_x = \int \mathrm{d}y\, \bar{n}(y),$$

which can be measured in experiments as in Ref.[97]. Within the 1D model, this ratio N/L_x is proportional to γN, allowing us to use γN as a dimensionless parameter to characterize the many-body phase.

Furthermore, the interaction parameter g defined in Eq. (5.10) can be shown to scale linearly as

$$g \propto N \cdot \frac{g_{\text{2D}}}{n_x(\omega_y^2 - \Omega^2)}.$$

Thus, the normalized parameter g/N serves as a convenient and physically meaningful control parameter for identifying quantum phases. It can be used to locate the experimental system within the phase diagram because it depends solely on experimentally accessible quantities and remains independent of the theoretical simplifications specific to our model.

5.2 Phase Space of the System

The model given in Eq. (5.8) describes a rich variety of quantum phases and their intriguing competition. In the limit of small g/N, which corresponds to weak two-body interactions or large density, the Bogoliubov approximation can be employed to demonstrate BEC and its excitations. The resulting spectrum exhibits the well-known superfluid dispersion characterized by the so-called roton-maxon structure [94]. Below, this phase is referred to as the Meissner state, based on the terminology established in quasi-one-dimensional ultracold atomic gases in recent years [98]. As g/N increases, the roton minimum softens, and beyond a critical value, the ground state undergoes a phase transition from a uniform superfluid to a vortex state. In the isotropic rapid rotation limit $\Omega \to \omega_x = \omega_y$, which corresponds to large g/N in our model, the condensate acquires a large number of vortices with triangular lattice structure [3]. Beyond another critical value where cores of vortices start to overlap, and the number of vortices becomes of the order of the number of particles [16], the strong quantum fluctuations melt the vortex lattice, giving way to correlated FQH states described by the Laughlin wavefunction [95, 96].

We focus on the half-filling $\nu = 1/2$ by taking $N = 5$ bosons occupying $N_v = 10$ vortices. We set the maximum occupancy of each site to be the total number of bosons N, which is crucial for observing superfluid phases in the numerics. The full phase diagram is presented in Fig. 5.2(a). The phase boundaries are initially determined using DMRG via the calculation of the von Neumann entanglement entropy S_{vN} by cutting the system in two halves with almost an equal number of sites in each sub-

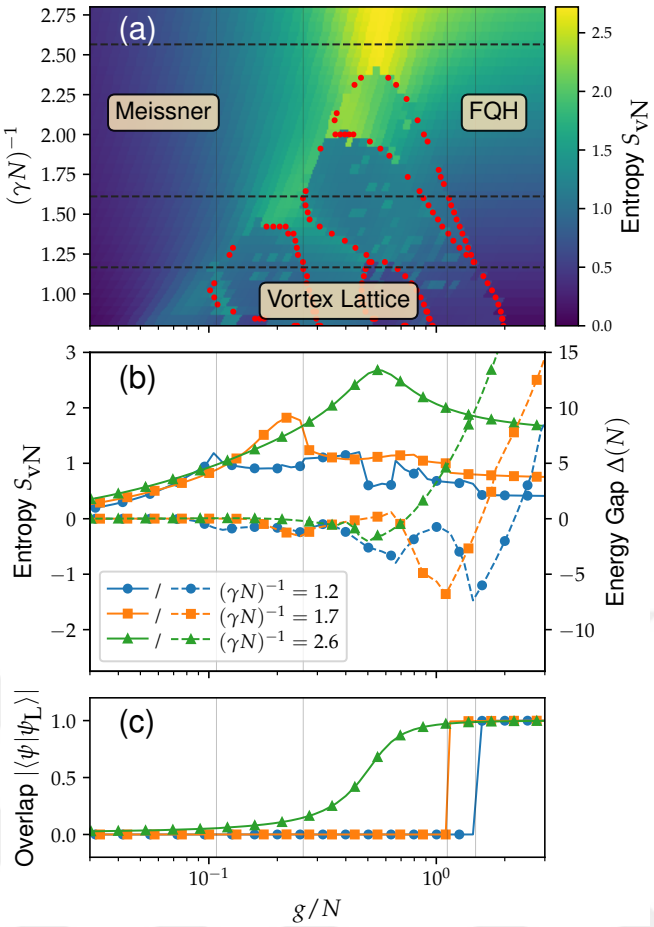

Figure 5.2: (a) The phase diagram of a rapidly rotating anisotropic Bose gas described by the Hamiltonian (5.8) for $N = 5$ as a function of the interaction strength g and anisotropy γ. The color bar indicates the von Neumann entanglement entropy calculated with DMRG. The red dots are obtained from ED by finding the change of the ground state momentum (see the main text). (b) The von Neumann entropy (solid line) and particle-hole excitation gap (5.16) (dashed line) along the horizontal cuts in the phase diagram. (c) The overlap between the ground state calculated with ED and the $\nu = 1/2$ Laughlin state along the same cuts.

system. S_{vN} serves as a useful indicator of a second-order phase transition, as the correlation length diverges at the critical points. This leads to sharp changes in the entanglement entropy even for small systems, as demonstrated in Fig. 5.2(b).

We also calculate the energy gap for particle-hole excitations to probe the compressible superfluid states, which can readily be obtained using both ED and DMRG. In

the Meissner and vortex-lattice phases, these excitations are expected to be gapless in the thermodynamic limit due to the presence of a condensate. In contrast, correlated incompressible states, including FQH states, exhibit a finite particle-hole excitation gap. This gap corresponds to the jump in the chemical potential when adding or removing a particle. In order to minimize the finite-size effects, the energy gap is defined as [16]

$$\Delta(N) = N\left(\frac{E(N+1)}{N+1} + \frac{E(N-1)}{N-1} - 2\frac{E(N)}{N}\right), \tag{5.16}$$

where $E(N)$ is the ground state energy of the Hamiltonian (5.8) for a system with N bosons. As shown in Fig. 5.2(b), the energy gap $\Delta(N)$ remains small in both Meissner and vortex lattice phases, albeit nonvanishing due to the combined effects of the trap potential, the finite particle number, and the edges. However, upon entering the FQH phase, the energy gap increases proportionally to the interaction strength g, signaling the onset of the incompressible ground state, characteristic of the FQH phase [16].

To confirm these boundaries independently, we compute the expectation value of the total momentum [Eq. (5.13)] in the ground state with ED and mark the boundaries with red dots in Fig. 5.2(a). As an example, along the cut $\gamma^{-1} \approx 6$ in the figure, the ground state momentum follows the sequence: $K = 0$, then $K = 1$, back to $K = 0$, a small region with $K = 2$, followed by $K = 1$ and finally $K = 0$ again. Positive and negative nonvanishing momenta exhibit degenerate energies, manifesting the translational symmetry breaking induced by the vortex lattice ground state. A similar phenomenon is inferred from the emergence of degenerate energy levels at Haldane momenta in torus geometry [16]. By calculating the expectation value of density in the ground state, we have obtained sound evidence that each domain exhibits a different vortex lattice. We expect that kinks or abrupt changes in these results reliably indicate the transition between Meissner and vortex phases. However, finite-size effects may prevent an accurate characterization of the competition between distinct lattice structures. This also explains the noisy behavior of the entanglement entropy in the vortex phases seen in Fig. 5.2(b), which is possibly due to the frustration of the lattice by the finite-size constraint. Therefore, we do not pursue an investigation of the competition between distinct vortex lattice structures in the thermodynamic limit, which can be addressed reliably with a GP formalism [99].

5.2.1 Fractional Quantum Hall Phase

In the strong interaction limit, $g/N \gg 1$, the influence of the trap potential becomes negligible, and a strongly correlated ground state emerges, whose nature is determined solely by the parameter γ [100, 95, 96]. When the interaction term in Hamiltonian (5.8) decays very rapidly for $\gamma^{-1} < \sqrt{2}\pi \approx 4.4$, the ground state enters a regime known as the thin-cylinder limit, in which the ground state forms a "crystal" of atoms with equal spacing, known as the Tao-Thouless state [100, 96]. For instance, at half-filling ($\nu = 1/2$), the atomic occupations follow a regular pattern $101010\ldots$. In Fig. 5.3, we present the ED results for a system of 5 bosons on 11 sites, which manifest such a Tao-Thouless state for $\gamma^{-1} \approx 4$ and $g = 10$.We have also verified that the low-lying quasiparticle excitations emerge through the creation of a domain wall structure $\cdots 0101|1010 \cdots$ which has been established in the standard Tao-Thouless theory.

When γ^{-1} increases such that $\gamma^{-1} \lesssim 2.5N$, the longer-range components of the interaction [Eq. (5.9)] become significant and give rise to the melting of the crystalline Tao-Thouless state. This favors the formation of an incompressible Laughlin liquid characterized by a uniform density and the absence of broken translation symmetry. In Fig. 5.3, we obtain such a ground state through ED for $\gamma^{-1} = 10$ and $g = 10$, which reveals uniform $\nu = 1/2$ liquid in the center, which is modified towards the edges as expected.

Lastly, when $\gamma^{-1} > 2.5N$, the cylinder's circumference becomes much larger than its width, resembling a thin ribbon or hoop. In this regime—known as the wide-cylinder limit—the system effectively reduces to one dimension. As $\gamma \to 0$, the exponential in the interaction [Eq. (5.9)] approaches one, allowing each site to couple to every other site in the chain regardless of distance. Simultaneously, the spacing between the neighboring Gaussian centers, $y_n \propto \gamma$, illustrated in Fig. 5.1, diminishes, and the two opposite chiral edges start to overlap, which brings the system to a pure edge limit without bulk. Here, because of the long-range interactions, the correlations in the ground state increase beyond area-law entanglement, and DMRG requires a much bigger bond dimension for convergence. Nonetheless, this limit can be described by using the hydrodynamic approach and Luttinger liquid formalism [101, 95, 48].

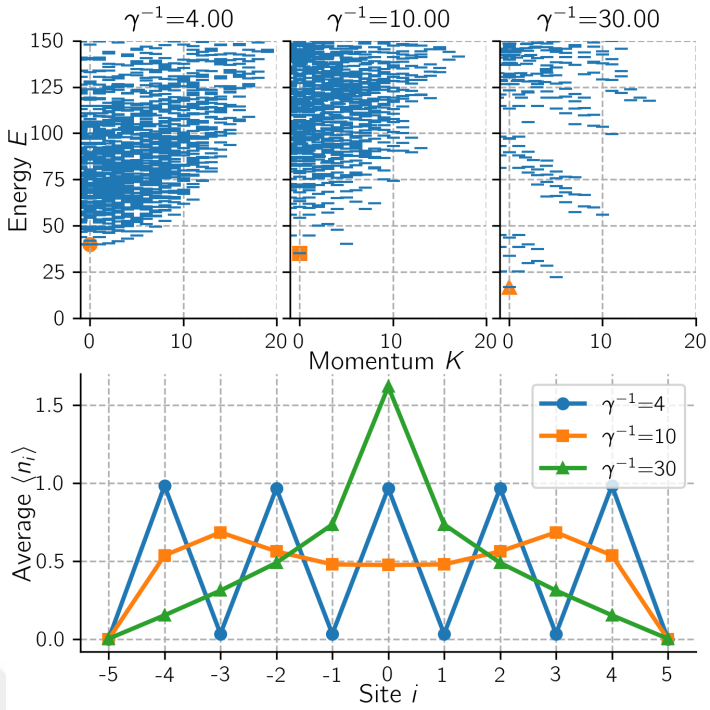

Figure 5.3: (Top) Energy spectrum of the Hamiltonian (5.8) for $N = 5$ bosons with $g = 10$ and $\gamma^{-1} = 4$, 10 and 30, which is cut through the FQH phase in Fig. 5.2 vertically. We choose the number of sites to be 11 to have a symmetric spectrum (density) with respect to the origin $K = 0$ ($i = 0$). Ground state is labeled with (orange) marks for better visibility. (Bottom) Occupations $\langle n_i \rangle$ in the ground state for the trap minima located in the middle site which shows transition from the Tao-Thouless state to the Laughlin state and then to the quasi-1D state, as the anisotropy ratio γ tuned from thin-cylinder to two-dimensional and then to wide-cylinder limit regimes.

In the rapid rotation limit $2\Omega/\omega_c = 1$, the first term in Eq. (5.8) can be dropped, and the resulting Hamiltonian becomes purely interacting. In this case, the Laughlin wavefunction becomes the exact ground state for the present contact interactions, which has been extended to the cylindrical geometry by Thouless [102] (see also [103, 104] for detailed discussions):

$$\psi_{\mathrm{L}}(x,y) = \prod_{i>j} \left(e^{\mathrm{i}2\pi\gamma z_i/\ell} - e^{\mathrm{i}2\pi\gamma z_j/\ell}\right)^m e^{-\sum_i \frac{y_i^2}{2\ell^2}}. \tag{5.17}$$

where $z = x + iy$.

We compute the overlap between the ground state obtained from ED and the corre-

sponding Laughlin state with $\nu = 1/2$ or $m = 2$ along constant-γ^{-1} cuts in the phase diagram. As shown in Fig. 5.2(c), the overlaps jump from zero to nearly unity at a critical interaction strength g_c in both the thin-cylinder and two-dimensional regimes. This transition closely aligns with the vortex lattice-FQH phase boundary previously identified through the energy gap and the entanglement entropy. In contrast, in the pure edge limit ($(\gamma N)^{-1} > 2.5$), the overlap evolves smoothly from the Meissner phase to the FQH phase without any sharp kink. Moreover, the system does not go through an intermediate vortex phase, which is sensible because a one-dimensional fluid cannot accommodate vortices.

5.2.2 Vortex Lattice and Meissner Phases

When the interaction and potential energies in (5.8) become comparable, the system admits a rich phase diagram as illustrated in Figure 5.2. We find that decreasing the interaction strength favors a vortex lattice more than a strongly correlated FQH liquid for lower values of $(\gamma N)^{-1}$. The reason why we do not observe a vortex lattice for higher values of $(\gamma N)^{-1}$ is that the width $L_y < 2\pi\ell$ decreases enough to prevent any vortex from entering the system.

Each enclosed region in the diagram in Figure 5.2 corresponds to a vortex lattice ground state different from the neighboring regions. The common property of these phases is that they have two degenerate ground states with nonzero momentum K (5.13). The superposition of these two degenerate states gives a vortex lattice as shown in Fig.5.4. The same vortex lattice structure can be obtained with the numerical solutions of the GP-like study in the LLL limit [94, 105, 99].

A further decrease in the parameter g/N results in another phase transition. In this phase, no vortex lattice appears inside the system, although the system is in the rapid rotation limit $\Omega \to \omega_x$. This is why we refer to this phase as the Meissner phase. The many-body gap does not close up to the non-interacting case, where $g = 0$. In other words, this phase is adiabatically connected to the non-interacting MPS state. The rapid decrease in the von Neumann entropy $S_{\text{vN}} \to 0$ represented in Fig.5.2 supports our statement.

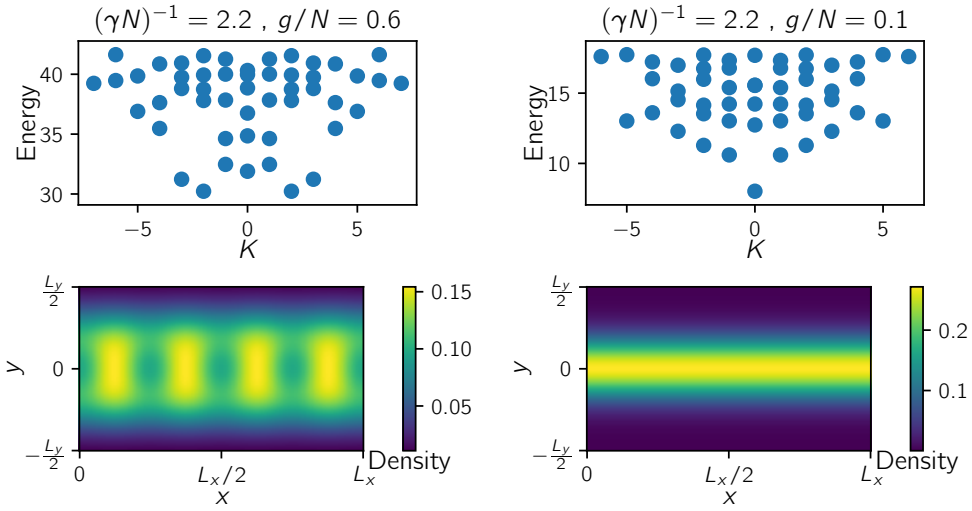

Figure 5.4: (Top) energy spectrum of a vortex lattice obtained with $(\gamma N)^{-1} = 2.2$ and $g/N = 0.6$ and a Meissner phase with $(\gamma N)^{-1} = 2.2$ and $g/N = 0.1$. (Bottom) Density profiles of the ground state related to the given energy spectrum above. The given density for the vortex lattice is obtained with a linear combination of the degenerate ground states with $K = \pm 2$.

We cut the phase diagram for constant γ^{-1} values, both of which cut the vortex lattice phase, and report the change in the entropy S_{vN} with respect to increasing interaction strength g in Fig.5.5. We observe a rapid increase in entropy during the transition from the Meissner to the vortex lattice phase, accompanied by the formation of a tip at the transition point. The tip of the entropy increases rapidly with the number of particles N in the system. This may suggest a divergence of a physical quantity in the transition, which can be used as a signature for a second-order phase transition.

5.2.3 Crossover at Quasi-1D Regime

Above $(\gamma N)^{-1} \approx 2.5$, the phase boundary between Meissner and FQH phases shows a smooth transition in entanglement entropy without any kink, based on the largest available data with $N = 5$, 8, and 10, as presented in Fig.5.6. This suggests the possibility of a crossover rather than a true phase transition. However, in this regime, the system becomes strongly one-dimensional with arbitrarily long-range coupling (because of large $(\gamma N)^{-1}$), leading to significantly slower convergence in the DMRG

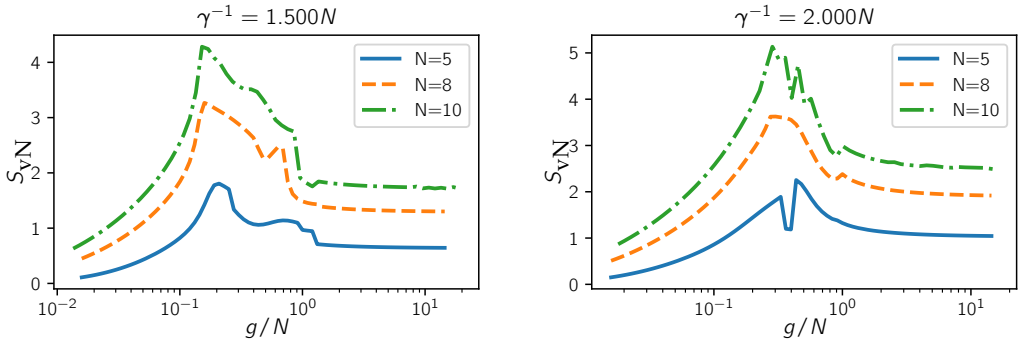

(a) (b)

Figure 5.5: Entanglement entropy S_{vN} as a function of the interaction strength g for $N = 5$, 8, and 10 bosons for (a) $(\gamma N)^{-1} = 1.50$ and (b) $(\gamma N)^{-1} = 2.00$. The entropy during the phase transition between the Meissner and vortex lattice phases forms a tip in the entanglement spectrum, and rapidly increases with the number of atoms N, which can be used as a signature of a diverging behaviour in the second-order phase transition.

algorithm, which hinders our ability to obtain more conclusive evidence. Below, we discuss this transition in more detail from the perspective of the FQH phase and the Laughlin ansatz.

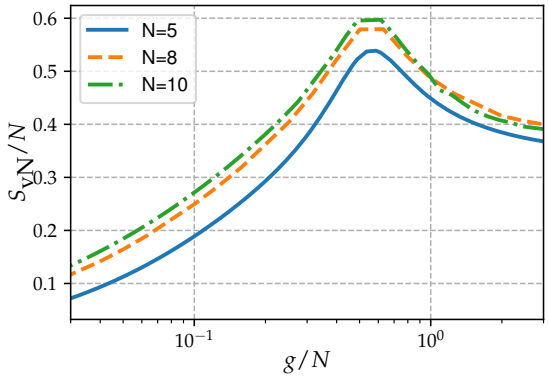

Figure 5.6: Entanglement entropy per particle S_{vN}/N as a function of the interaction strength g for $N = 5$, 8, and 10 bosons in the half filling case $\nu = 1/2$ and in the pure edge limit $(\gamma N)^{-1} = 2.75$. The scaling with g/N gives a critical point $g_c/N \approx 0.5$.

At the crossover between these Meissner and FQH phases—where the overlap with the Laughlin wavefunction increases continuously—the particle-hole gap $\Delta(N)$ does

not increase abruptly, signaling a smooth evolution of the ground state. However, the von Neumann entropy exhibits a cusp-like structure as shown in Fig. 5.6 for $N = 5$, 8, and 10 bosons. While the Meissner phase is adiabatically connected to a matrix product state with $S_{\text{vN}} = 0$, the FQH phase shows nontrivial entanglement; thus, a critical point separating these two limits is reasonable. Note that Eq. (5.8) in the limit $\gamma^{-1} \to \infty$ maps exactly to a one-dimensional Bose gas on a ring with contact interactions—the well-known Lieb-Liniger model [106]. In this case, Ref. [107] reported a crossover from a uniform condensate to a fragmented one (or a soliton state) as a function of the interaction strength based on ED, which is supported by our result shown in Fig. 5.6. A similar phenomenon was considered in Ref. [108] using the symmetric gauge, which reported a transition to the usual condensed state under asymmetric perturbations breaking the conservation of total angular momentum. To our knowledge, this phenomenon has not been previously studied in the context of FQH phases of rapidly rotating anisotropic gases. We anticipate a similar competition with the condensed state in our case when some terms are added to the Hamiltonian that do not conserve the total momentum K, such as the trapping along the circumference of the cylinder, which is the subject of future investigation.

5.3 Conclusion

In this section, we developed a theoretical framework for rapidly rotating anisotropic Bose gases with asymmetric trapping $\omega_x < \omega_y$. The rotation frequency is set to the weaker trapping frequency, $\Omega = \omega_x$, whereas in the orthogonal direction, a residual confinement remains due to $\Omega < \omega_y$. In this setting, the elongated cloud is described by the Landau gauge on a cylindrical geometry where translationally invariant circumference corresponds to a trap-free x-direction. This geometry is widely studied in two-dimensional electronic systems under a strong magnetic field, but its bosonic counterpart remains relatively underexplored. In particular, the interplay between Bose condensation, vortex lattice formation, and the strongly correlated phases in this geometry is still an open and intriguing problem.

By projecting the Hamiltonian onto the LLL in the fast rotation limit, we derived an effective model characterized by two parameters: the interaction strength g and

the anisotropy ratio γ. Using ED, we mapped out the full phase diagram at half-filling ($\nu = 1/2$) and identified three distinct regimes: (i) weakly interacting Bose gas without vortices, which we refer to as the Meissner phase, (ii) a series of vortex phases exhibiting different lattice structures depending on g and γ, and (iii) a strongly correlated phase well described by the Laughlin wavefunction. We benchmarked our main findings in larger systems using the DMRG.

Due to the competition of superfluid phases with broken $U(1)$ and translation symmetries and strongly correlated incompressible phases with topological order, we demonstrated the necessity of employing a variety of complementary probes across the full phase diagram. The compressible superfluid phases were identified through the particle-hole energy gap, while the topologically ordered FQH phase was revealed via the overlap between the exact diagonalization ground state and the Laughlin wavefunction. Interestingly, the entanglement entropy was found to provide a robust diagnostic throughout the entire phase diagram, offering reliable identification of the phase transitions.

In the strongly correlated regime $g \gg 1$, the entire range—from wide-cylinder to two-dimensional to thin-cylinder regime—is described by the Laughlin wavefunction. Indeed, Rezayi and Haldane used this fact to construct the phase diagram starting from $\gamma = 0$ and building Laughlin wavefunctions for different anisotropy ratios [95]. In our work, neither DMRG nor ED reveals a sharp phase boundary between the Laughlin phase, the Tao-Thouless limit, or the wide-cylinder regime; rather, these limits appear to be adiabatically connected in broad agreement with Ref. [96]. While the thin-cylinder limit is analytically tractable and has recently benefited from the development of powerful DMRG-based numerical methods [109, 110], the wide-cylinder regime remains comparatively less explored and also technically more challenging. To what extent the FQH phase survives in this limit is still an open question [95], possibly competing with a correlated vortex liquid without condensation [3]. Interestingly, recent experiments on cold atomic gases [97, 111, 112] are capable of probing precisely this regime, potentially paving the way for novel insights in the near future.

Many open questions remain that warrant further investigation. First, the extent to which the topology of the phase diagram persists in the regime $\omega_x < \Omega < \omega_y$— rel-

evant for current experiments [111]—is an important issue that will be addressed in a separate study. In this regime, determining a (meta)stable ground state is a delicate theoretical problem due to the inherent instability of the saddle-shaped trap potential. Furthermore, the role of higher Landau levels may be important for explaining some of the observations in these experiments, and a detailed theoretical analysis is required. In the present stable anisotropic case, understanding the exact vortex lattice structures in the thermodynamic limit and its excitations may shed light on the microscopic mechanism behind the vortex lattice melting. Last but not least, rapidly rotating dipolar Bose gases and their low-energy physics in the Landau gauge may offer a compelling comparison to the phase diagram presented here, where the source of anisotropy originates not from the trap potential as in our work but from the two-body interaction itself [113]. In summary, our results establish a comprehensive framework that unifies weakly interacting Bose condensates, vortex matter, and strongly correlated topological phases, laying the groundwork for future theoretical and experimental investigations of anisotropic quantum fluids.

CHAPTER 6

CONCLUSION

In this thesis, we studied two distinct topics related to Bose gases in anisotropic traps. The first topic is about dark solitons and their nonlinear dynamics. The second one concerns topological phases that emerge when the system rotates rapidly. In both cases, the shape of the trap and the anisotropy are essential for the system's behavior.

In the first part, we employed a variational method to investigate the snake instability of dark solitons in two dimensions. Our wavefunction describes how the soliton bends and how vortex-antivortex pairs appear. Using Lagrangian analysis, we investigated the stability of dark solitons and determined the critical anisotropy required to suppress the snaking instability. The results matched well with full numerical simulations of the 2D GP equation. Our method is more flexible than previous linear methods and can be applied to more complex situations, such as moving solitons or traps with different shapes [70, 88, 83].

In the second part, we studied a rotating Bose gas in an anisotropic trap. We started from the full 2D Hamiltonian and projected it onto a 1D model using the Landau gauge in a cylindrical setup. Using ED and DMRG methods, we mapped out the phase diagram at half filling, revealing Meissner-like condensate phases, a variety of vortex lattices, and a strongly correlated Laughlin-like phase.

In summary, this thesis presents two main results. The first is an effective variational method to investigate the stability and dynamical analysis of dark solitons in realistic trap geometries. The second is a quantum phase analysis of the rotating anisotropic Bose gas, which can be a promising tool for studying systems that appear in new experiments [97, 111, 112].

REFERENCES

[1] C. Pethick and H. Smith, *Bose-Einstein condensation in dilute gases*. Cambridge University Press, 2002.

[2] N. Cooper, "Rapidly rotating atomic gases," *Advances in Physics*, vol. 57, p. 539–616, Nov. 2008.

[3] A. L. Fetter, "Rotating trapped Bose-Einstein condensates," *Reviews of Modern Physics*, vol. 81, p. 647–691, May 2009.

[4] S. Viefers, "Quantum Hall physics in rotating Bose–Einstein condensates," *Journal of Physics: Condensed Matter*, vol. 20, p. 123202, feb 2008.

[5] D. J. Frantzeskakis, "Dark solitons in atomic bose–einstein condensates: from theory to experiments," *Journal of Physics A: Mathematical and Theoretical*, vol. 43, p. 213001, May 2010.

[6] Y. Kivshar, "Dark optical solitons: physics and applications," *Physics Reports*, vol. 298, p. 81–197, May 1998.

[7] V. E. Zakharov and A. M. Rubenchik, "Instability of waveguides and solitons in nonlinear media," *Soviet Physics JETP*, vol. 38, no. 3, pp. 494–500, 1974. Russian original: Zh. Eksp. Teor. Fiz. **65**, 997–1010 (1973).

[8] J. Brand and W. P. Reinhardt, "Solitonic vortices and the fundamental modes of the "snake instability": Possibility of observation in the gaseous bose-einstein condensate," *Physical Review A*, vol. 65, Apr. 2002.

[9] S. Komineas and N. Papanicolaou, "Solitons, solitonic vortices, and vortex rings in a confined bose-einstein condensate," *Physical Review A*, vol. 68, Oct. 2003.

[10] A. E. Muryshev, H. B. van Linden van den Heuvell, and G. V. Shlyapnikov, "Stability of standing matter waves in a trap," *Phys. Rev. A*, vol. 60, pp. R2665–R2668, Oct. 1999.

[11] D. L. Feder, M. S. Pindzola, L. A. Collins, B. I. Schneider, and C. W. Clark, "Dark-soliton states of Bose-Einstein condensates in anisotropic traps," *Phys. Rev. A*, vol. 62, Oct. 2000.

[12] R. Carretero-González, D. J. Frantzeskakis, and P. G. Kevrekidis, "Nonlinear waves in Bose–Einstein condensates: physical relevance and mathematical techniques," *Nonlinearity*, vol. 21, p. R139, jun 2008.

[13] P. G. Kevrekidis, G. Theocharis, D. J. Frantzeskakis, and A. Trombettoni, "Avoiding infrared catastrophes in trapped bose-einstein condensates," *Physical Review A*, vol. 70, Aug. 2004.

[14] J. R. Abo-Shaeer, C. Raman, J. M. Vogels, and W. Ketterle, "Observation of vortex lattices in Bose-Einstein condensates," *Science*, vol. 292, no. 5516, pp. 476–479, 2001.

[15] V. Bretin, S. Stock, Y. Seurin, and J. Dalibard, "Fast rotation of a Bose-Einstein condensate," *Phys. Rev. Lett.*, vol. 92, p. 050403, Feb 2004.

[16] N. R. Cooper, N. K. Wilkin, and J. M. F. Gunn, "Quantum phases of vortices in rotating Bose-Einstein condensates," *Phys. Rev. Lett.*, vol. 87, p. 120405, Aug 2001.

[17] J. Sinova, C. B. Hanna, and A. H. MacDonald, "Quantum melting and absence of Bose-Einstein condensation in two-dimensional vortex matter," *Phys. Rev. Lett.*, vol. 89, p. 030403, Jun 2002.

[18] M. Linn, M. Niemeyer, and A. L. Fetter, "Vortex stabilization in a small rotating asymmetric Bose-Einstein condensate," *Phys. Rev. A*, vol. 64, p. 023602, Jul 2001.

[19] M. O. Oktel, "Vortex lattice of a Bose-Einstein condensate in a rotating anisotropic trap," *Phys. Rev. A*, vol. 69, p. 023618, Feb 2004.

[20] D. L. Kovrizhin, "Density matrix renormalization group for bosonic quantum Hall effect," *Physical Review B*, vol. 81, Mar. 2010.

[21] M. H. Anderson, J. R. Ensher, M. R. Matthews, C. E. Wieman, and E. A.

Cornell, “Observation of bose-einstein condensation in a dilute atomic vapor,” *Science*, vol. 269, no. 5221, pp. 198–201, 1995.

[22] C. C. Bradley, C. A. Sackett, J. J. Tollett, and R. G. Hulet, “Evidence of bose-einstein condensation in an atomic gas with attractive interactions,” *Phys. Rev. Lett.*, vol. 75, pp. 1687–1690, Aug 1995.

[23] K. B. Davis, M. O. Mewes, M. R. Andrews, N. J. van Druten, D. S. Durfee, D. M. Kurn, and W. Ketterle, “Bose-einstein condensation in a gas of sodium atoms,” *Phys. Rev. Lett.*, vol. 75, pp. 3969–3973, Nov 1995.

[24] L. Pitaevskii and S. Stringari, *Bose-Einstein condensation and superfluidity*, vol. 164. Oxford University Press, 2016.

[25] M. R. Matthews, B. P. Anderson, P. C. Haljan, D. S. Hall, M. J. Holland, J. E. Williams, C. E. Wieman, and E. A. Cornell, “Watching a superfluid untwist itself: Recurrence of rabi oscillations in a bose-einstein condensate,” *Phys. Rev. Lett.*, vol. 83, pp. 3358–3361, Oct 1999.

[26] K. W. Madison, F. Chevy, W. Wohlleben, and J. Dalibard, “Vortex formation in a stirred bose-einstein condensate,” *Phys. Rev. Lett.*, vol. 84, pp. 806–809, Jan 2000.

[27] P. Engels, I. Coddington, P. C. Haljan, and E. A. Cornell, “Nonequilibrium effects of anisotropic compression applied to vortex lattices in bose-einstein condensates,” *Phys. Rev. Lett.*, vol. 89, p. 100403, Aug 2002.

[28] R. J. Donnelly, *Quantized vortices in helium II*, vol. 2. Cambridge University Press, 1991.

[29] T.-L. Ho, “Bose-Einstein condensates with large number of vortices,” *Phys. Rev. Lett.*, vol. 87, p. 060403, Jul 2001.

[30] R. E. Prange and S. M. Girvin, eds., *The Quantum Hall Effect*. Graduate Texts in Contemporary Physics, New York, NY: Springer-Verlag New York Inc., 2 ed., December 1990. Published: 11 December 1989 (Softcover), 06 December 2012 (eBook).

[31] E. P. Gross, "Structure of a quantized vortex in boson systems," *Il Nuovo Cimento*, vol. 20, p. 454–477, May 1961.

[32] L. P. Pitaevskii, "Vortex lines in an imperfect bose gas," *Sov. Phys. JETP*, vol. 13, no. 2, pp. 451–454, 1961.

[33] C. Pethick and H. Smith, *Bose-Einstein condensation in dilute gases*. Cambridge University Press, 2002.

[34] D. S. Petrov, M. Holzmann, and G. V. Shlyapnikov, "Bose-Einstein condensation in quasi-2d trapped gases," *Phys. Rev. Lett.*, vol. 84, pp. 2551–2555, Mar 2000.

[35] D. Krökel, N. J. Halas, G. Giuliani, and D. Grischkowsky, "Dark-pulse propagation in optical fibers," *Physical Review Letters*, vol. 60, p. 29–32, Jan. 1988.

[36] A. M. Weiner, J. P. Heritage, R. J. Hawkins, R. N. Thurston, E. M. Kirschner, D. E. Leaird, and W. J. Tomlinson, "Experimental observation of the fundamental dark soliton in optical fibers," *Physical Review Letters*, vol. 61, p. 2445–2448, Nov. 1988.

[37] M. Chen, M. A. Tsankov, J. M. Nash, and C. E. Patton, "Microwave magnetic-envelope dark solitons in yttrium iron garnet thin films," *Physical Review Letters*, vol. 70, p. 1707–1710, Mar. 1993.

[38] L. Landau and E. Lifshitz, *Statistical Physics: Volume 5*. Butterworth-Heinemann, 2013.

[39] D. Butts and D. Rokhsar, "Predicted signatures of rotating bose–einstein condensates," *Nature*, vol. 397, no. 6717, pp. 327–329, 1999.

[40] V. Schweikhard, I. Coddington, P. Engels, V. P. Mogendorff, and E. A. Cornell, "Rapidly rotating Bose-Einstein condensates in and near the lowest Landau level," *Phys. Rev. Lett.*, vol. 92, p. 040404, Jan 2004.

[41] A. A. Abrikosov, "On the magnetic properties of superconductors of the second group," *Soviet Physics-JETP*, vol. 5, pp. 1174–1182, 1957.

[42] E. H. Hall, "On a new action of the magnet on electric currents," *American Journal of Mathematics*, vol. 2, no. 3, pp. 287–292, 1879.

[43] K. v. Klitzing, G. Dorda, and M. Pepper, "New method for high-accuracy determination of the fine-structure constant based on quantized Hall resistance," *Phys. Rev. Lett.*, vol. 45, pp. 494–497, Aug 1980.

[44] D. C. Tsui, H. L. Stormer, and A. C. Gossard, "Two-dimensional magnetotransport in the extreme quantum limit," *Phys. Rev. Lett.*, vol. 48, pp. 1559–1562, May 1982.

[45] D. J. Thouless, M. Kohmoto, M. P. Nightingale, and M. den Nijs, "Quantized Hall conductance in a two-dimensional periodic potential," *Phys. Rev. Lett.*, vol. 49, pp. 405–408, Aug 1982.

[46] R. B. Laughlin, "Quantized hall conductivity in two dimensions," *Phys. Rev. B*, vol. 23, pp. 5632–5633, May 1981.

[47] X.-G. Wen, "Topological orders and edge excitations in fractional quantum hall states," *Advances in Physics*, vol. 44, no. 5, pp. 405–473, 1995.

[48] X.-G. Wen, *Quantum Field Theory of Many-Body Systems: From the Origin of Sound to an Origin of Light and Electrons*. Oxford: Oxford University Press, 09 2007.

[49] C. Nayak, S. H. Simon, A. Stern, M. Freedman, and S. Das Sarma, "Non-abelian anyons and topological quantum computation," *Rev. Mod. Phys.*, vol. 80, pp. 1083–1159, Sep 2008.

[50] L. Landau, "Diamagnetismus der metalle," *Zeitschrift für Physik*, vol. 64, p. 629–637, Sept. 1930.

[51] S. M. Girvin and K. Yang, *Modern Condensed Matter Physics*. Cambridge University Press, 2019.

[52] D. J. Griffiths and D. F. Schroeter, *Introduction to Quantum Mechanics*. Cambridge University Press, 3 ed., 2018.

[53] G. B. Arfken, H. J. Weber, and F. E. Harris, *Mathematical methods for physicists: a comprehensive guide*. Academic press, 2011.

[54] R. B. Laughlin, “Anomalous quantum Hall effect: An incompressible quantum fluid with fractionally charged excitations,” *Phys. Rev. Lett.*, vol. 50, pp. 1395–1398, May 1983.

[55] W. Bao, D. Jaksch, and P. A. Markowich, “Numerical solution of the Gross–Pitaevskii equation for Bose–Einstein condensation,” *Journal of Computational Physics*, vol. 187, no. 1, pp. 318–342, 2003.

[56] J. Javanainen and J. Ruostekoski, “Symbolic calculation in development of algorithms: split-step methods for the Gross–Pitaevskii equation,” *Journal of Physics A: Mathematical and General*, vol. 39, no. 12, p. L179, 2006.

[57] P. Bader, “Fourier-splitting methods for the dynamics of rotating Bose–Einstein condensates,” *Journal of Computational and Applied Mathematics*, vol. 336, pp. 267–280, 2018.

[58] A. L. Fetter and J. D. Walecka, *Quantum theory of many-particle sys*. Dover Books on Physics, Mineola, NY: Dover Publications, May 2003.

[59] S. R. White, “Density matrix formulation for quantum renormalization groups,” *Physical Review Letters*, vol. 69, p. 2863–2866, Nov. 1992.

[60] S. R. White, “Density-matrix algorithms for quantum renormalization groups,” *Physical Review B*, vol. 48, p. 10345–10356, Oct. 1993.

[61] U. Schollwöck, “The density-matrix renormalization group,” *Rev. Mod. Phys.*, vol. 77, pp. 259–315, Apr 2005.

[62] U. Schollwöck, “The density-matrix renormalization group in the age of matrix product states,” *Annals of Physics*, vol. 326, no. 1, pp. 96–192, 2011. January 2011 Special Issue.

[63] J. Eisert, M. Cramer, and M. B. Plenio, “Colloquium: Area laws for the entanglement entropy,” *Reviews of modern physics*, vol. 82, no. 1, pp. 277–306, 2010.

[64] J. D. Bekenstein, “Black holes and entropy,” *Physical Review D*, vol. 7, no. 8, p. 2333, 1973.

[65] M. Srednicki, "Entropy and area," *Phys. Rev. Lett.*, vol. 71, pp. 666–669, Aug 1993.

[66] C. Callan and F. Wilczek, "On geometric entropy," *Physics Letters B*, vol. 333, no. 1-2, pp. 55–61, 1994.

[67] M. Fishman, S. R. White, and E. M. Stoudenmire, "The ITensor software library for tensor network calculations," *SciPost Phys. Codebases*, p. 4, 2022.

[68] V. Zakharov and A. Rubenchik, "Instability of waveguides and solitons in nonlinear media," *Soviet Journal of Experimental and Theoretical Physics*, vol. 38, p. 494, 1974.

[69] Y. S. Kivshar and D. E. Pelinovsky, "Self-focusing and transverse instabilities of solitary waves," *Physics Reports*, vol. 331, p. 117–195, June 2000.

[70] P. O. Fedichev, A. E. Muryshev, and G. V. Shlyapnikov, "Dissipative dynamics of a kink state in a bose-condensed gas," *Phys. Rev. A*, vol. 60, pp. 3220–3224, Oct. 1999.

[71] A. V. Mamaev, M. Saffman, and A. A. Zozulya, "Propagation of dark stripe beams in nonlinear media: Snake instability and creation of optical vortices," *Physical Review Letters*, vol. 76, p. 2262–2265, Mar. 1996.

[72] V. Tikhonenko, J. Christou, B. Luther-Davies, and Y. S. Kivshar, "Observation of vortex solitons created by the instability of dark soliton stripes," *Optics Letters*, vol. 21, p. 1129, Aug. 1996.

[73] S. Burger, K. Bongs, S. Dettmer, W. Ertmer, K. Sengstock, A. Sanpera, G. V. Shlyapnikov, and M. Lewenstein, "Dark solitons in bose-einstein condensates," *Physical Review Letters*, vol. 83, p. 5198–5201, Dec. 1999.

[74] J. Denschlag, J. E. Simsarian, D. L. Feder, C. W. Clark, L. A. Collins, J. Cubizolles, L. Deng, E. W. Hagley, K. Helmerson, W. P. Reinhardt, S. L. Rolston, B. I. Schneider, and W. D. Phillips, "Generating solitons by phase engineering of a bose-einstein condensate," *Science*, vol. 287, p. 97–101, Jan. 2000.

[75] B. P. Anderson, P. C. Haljan, C. A. Regal, D. L. Feder, L. A. Collins, C. W. Clark, and E. A. Cornell, "Watching dark solitons decay into vortex rings in

a bose-einstein condensate," *Physical Review Letters*, vol. 86, p. 2926–2929, Apr. 2001.

[76] Z. Dutton, M. Budde, C. Slowe, and L. V. Hau, "Observation of quantum shock waves created with ultra- compressed slow light pulses in a bose-einstein condensate," *Science*, vol. 293, p. 663–668, July 2001.

[77] J. Brand and W. P. Reinhardt, "Generating ring currents, solitons and svortices by stirring a bose-einstein condensate in a toroidal trap," *Journal of Physics B: Atomic, Molecular and Optical Physics*, vol. 34, pp. L113–L119, Feb. 2001.

[78] S. Donadello, S. Serafini, M. Tylutki, L. P. Pitaevskii, F. Dalfovo, G. Lamporesi, and G. Ferrari, "Observation of solitonic vortices in bose-einstein condensates," *Physical Review Letters*, vol. 113, Aug. 2014.

[79] A. Weller, J. P. Ronzheimer, C. Gross, J. Esteve, M. K. Oberthaler, D. J. Frantzeskakis, G. Theocharis, and P. G. Kevrekidis, "Experimental observation of oscillating and interacting matter wave dark solitons," *Physical Review Letters*, vol. 101, Sept. 2008.

[80] C. Becker, S. Stellmer, P. Soltan-Panahi, S. Dörscher, M. Baumert, E.-M. Richter, J. Kronjäger, K. Bongs, and K. Sengstock, "Oscillations and interactions of dark and dark–bright solitons in bose–einstein condensates," *Nature Physics*, vol. 4, p. 496–501, May 2008.

[81] S. Stellmer, C. Becker, P. Soltan-Panahi, E.-M. Richter, S. Dörscher, M. Baumert, J. Kronjäger, K. Bongs, and K. Sengstock, "Collisions of dark solitons in elongated bose-einstein condensates," *Physical Review Letters*, vol. 101, Sept. 2008.

[82] G. Theocharis, A. Weller, J. P. Ronzheimer, C. Gross, M. K. Oberthaler, P. G. Kevrekidis, and D. J. Frantzeskakis, "Multiple atomic dark solitons in cigar-shaped bose-einstein condensates," *Physical Review A*, vol. 81, June 2010.

[83] M. Ma, R. Carretero-González, P. G. Kevrekidis, D. J. Frantzeskakis, and B. A. Malomed, "Controlling the transverse instability of dark solitons and nucleation of vortices by a potential barrier," *Physical Review A*, vol. 82, Aug. 2010.

[84] S. K. Adhikari, "Stable, mobile, dark-in-bright, dipolar bose-einstein-condensate solitons," *Physical Review A*, vol. 89, Apr. 2014.

[85] E. A. Kuznetsov and S. K. Turitsyn, "Instability and collapse of solitons in media with a defocusing nonlinearity," *Soviet Physics JETP*, vol. 64, no. 8, p. 1583, 1988. Russian original: Zh. Eksp. Teor. Fiz. **94**, 119–129 (1988).

[86] I. Shomroni, E. Lahoud, S. Levy, and J. Steinhauer, "Evidence for an oscillating soliton/vortex ring by density engineering of a Bose–Einstein condensate," *Nature Physics*, vol. 5, p. 193–197, Jan. 2009.

[87] T. Mithun, A. R. Fritsch, I. B. Spielman, and P. G. Kevrekidis, "Dynamical instability of 3d stationary and traveling planar dark solitons," *Journal of Physics: Condensed Matter*, vol. 35, p. 014004, Nov. 2022.

[88] T. Busch and J. R. Anglin, "Motion of dark solitons in trapped Bose-Einstein condensates," *Phys. Rev. Lett.*, vol. 84, pp. 2298–2301, Mar 2000.

[89] B. Jackson, N. P. Proukakis, and C. F. Barenghi, "Dark-soliton dynamics in Bose-Einstein condensates at finite temperature," *Phys. Rev. A*, vol. 75, p. 051601, May 2007.

[90] P. Weinberg and M. Bukov, "QuSpin: a Python package for dynamics and exact diagonalisation of quantum many body systems part I: spin chains," *SciPost Phys.*, vol. 2, p. 003, 2017.

[91] P. Weinberg and M. Bukov, "QuSpin: a Python package for dynamics and exact diagonalisation of quantum many body systems. Part II: bosons, fermions and higher spins," *SciPost Phys.*, vol. 7, p. 020, 2019.

[92] M. Fishman, S. R. White, and E. M. Stoudenmire, "Codebase release 0.3 for ITensor," *SciPost Phys. Codebases*, pp. 4–r0.3, 2022.

[93] D. S. Petrov, D. M. Gangardt, and G. V. Shlyapnikov, "Low-dimensional trapped gases," *Journal de Physique IV (Proceedings)*, vol. 116, p. 5–44, Oct. 2004.

[94] S. Sinha and G. V. Shlyapnikov, "Two-dimensional Bose-Einstein condensate under extreme rotation," *Phys. Rev. Lett.*, vol. 94, p. 150401, Apr 2005.

[95] E. H. Rezayi and F. D. M. Haldane, "Laughlin state on stretched and squeezed cylinders and edge excitations in the quantum Hall effect," *Physical Review B*, vol. 50, p. 17199–17207, Dec. 1994.

[96] E. J. Bergholtz and A. Karlhede, "Quantum Hall system in Tao-Thouless limit," *Physical Review B*, vol. 77, p. 155308, Apr. 2008.

[97] R. J. Fletcher, A. Shaffer, C. C. Wilson, P. B. Patel, Z. Yan, V. Crépel, B. Mukherjee, and M. W. Zwierlein, "Geometric squeezing into the lowest Landau level," *Science*, vol. 372, p. 1318–1322, June 2021.

[98] M. Atala, M. Aidelsburger, M. Lohse, J. T. Barreiro, B. Paredes, and I. Bloch, "Observation of chiral currents with ultracold atoms in bosonic ladders," *Nature Physics*, vol. 10, no. 8, pp. 588–593, 2014.

[99] A. Keles, "Rotating anisotropic Bose gas with large number of vortices," 2025.

[100] R. Tao and D. J. Thouless, "Fractional quantization of Hall conductance," *Physical Review B*, vol. 28, p. 1142–1144, July 1983.

[101] F. Haldane, "Luttinger's theorem and bosonization of the Fermi surface, lectures given at the International School of Physics Enrico Fermi, Varenna, Italy (July, 1992)," *and J. Phys. C*, vol. 14, p. 2585, 1981.

[102] D. Thouless, "Theory of the quantized Hall effect," *Surface Science*, vol. 142, no. 1, pp. 147–154, 1984.

[103] S. Jansen, E. H. Lieb, and R. Seiler, "Symmetry breaking in Laughlin's state on a cylinder," *Communications in Mathematical Physics*, vol. 285, pp. 503–535, 2009.

[104] E. Westerberg and T. H. Hansson, "Quantum mechanics on thin cylinders," *Phys. Rev. B*, vol. 47, pp. 16554–16562, Jun 1993.

[105] S. I. Matveenko, D. Kovrizhin, S. Ouvry, and G. V. Shlyapnikov, "Vortex structures in rotating Bose-Einstein condensates," *Phys. Rev. A*, vol. 80, p. 063621, Dec 2009.

[106] E. H. Lieb and W. Liniger, "Exact analysis of an interacting Bose gas. I. the general solution and the ground state," *Phys. Rev.*, vol. 130, pp. 1605–1616, May 1963.

[107] R. Kanamoto, H. Saito, and M. Ueda, "Quantum phase transition in one-dimensional Bose-Einstein condensates with attractive interactions," *Phys. Rev. A*, vol. 67, p. 013608, Jan 2003.

[108] X.-J. Liu, H. Hu, L. Chang, W. Zhang, S.-Q. Li, and Y.-Z. Wang, "Fragmented condensate ground state of trapped weakly interacting bosons in two dimensions," *Phys. Rev. Lett.*, vol. 87, p. 030404, Jul 2001.

[109] M. P. Zaletel, R. S. K. Mong, and F. Pollmann, "Topological characterization of fractional quantum Hall ground states from microscopic hamiltonians," *Phys. Rev. Lett.*, vol. 110, p. 236801, Jun 2013.

[110] M. P. Zaletel, R. S. K. Mong, F. Pollmann, and E. H. Rezayi, "Infinite density matrix renormalization group for multicomponent quantum Hall systems," *Phys. Rev. B*, vol. 91, p. 045115, Jan 2015.

[111] B. Mukherjee, A. Shaffer, P. B. Patel, Z. Yan, C. C. Wilson, V. Crépel, R. J. Fletcher, and M. Zwierlein, "Crystallization of bosonic quantum Hall states in a rotating quantum gas," *Nature*, vol. 601, p. 58–62, Jan. 2022.

[112] R. Yao, S. Chi, B. Mukherjee, A. Shaffer, M. Zwierlein, and R. J. Fletcher, "Observation of chiral edge transport in a rapidly rotating quantum gas," *Nature Physics*, vol. 20, p. 1726–1731, Sept. 2024.

[113] L. Klaus, T. Bland, E. Poli, C. Politi, G. Lamporesi, E. Casotti, R. N. Bisset, M. J. Mark, and F. Ferlaino, "Observation of vortices and vortex stripes in a dipolar condensate," *Nature Physics*, vol. 18, no. 12, pp. 1453–1458, 2022.